

# Sheffield Hallam University

*Model X-ray scattering behaviour of arrays of structured cylinders.*

GALE, Trevor J.

Available from the Sheffield Hallam University Research Archive (SHURA) at:

<http://shura.shu.ac.uk/19215/>

## A Sheffield Hallam University thesis

This thesis is protected by copyright which belongs to the author.

The content must not be changed in any way or sold commercially in any format or medium without the formal permission of the author.

When referring to this work, full bibliographic details including the author, title, awarding institution and date of the thesis must be given.

Please visit <http://shura.shu.ac.uk/19215/> and <http://shura.shu.ac.uk/information.html> for further details about copyright and re-use permissions.

MODEL X-RAY SCATTERING BEHAVIOUR OF  
ARRAYS OF STRUCTURED CYLINDERS

---

TREVOR JOHN GALE

THESIS SUBMITTED IN PARTIAL FULFILMENT OF THE REQUIREMENTS  
FOR THE DEGREE OF MASTER OF PHILOSOPHY  
OF THE CNAAC

SEPTEMBER 1984

SPONSORING ESTABLISHMENT: SHEFFIELD CITY POLYTECHNIC

ProQuest Number: 10694095

All rights reserved

INFORMATION TO ALL USERS

The quality of this reproduction is dependent upon the quality of the copy submitted.

In the unlikely event that the author did not send a complete manuscript and there are missing pages, these will be noted. Also, if material had to be removed, a note will indicate the deletion.



ProQuest 10694095

Published by ProQuest LLC (2017). Copyright of the Dissertation is held by the Author.

All rights reserved.

This work is protected against unauthorized copying under Title 17, United States Code  
Microform Edition © ProQuest LLC.

ProQuest LLC.  
789 East Eisenhower Parkway  
P.O. Box 1346  
Ann Arbor, MI 48106 – 1346

ABSTRACT      Model X-ray scattering behaviour of arrays of  
structured cylinders.

T.J. Gale

The model X-ray scattering behaviour of hexagonal arrays of infinitely long cylinders with various internal structures is considered by regarding the model as a function of three parameters, viz:- the cylinder's scattering function, the swelling factor ( $\delta$ ), and the lattice interference function.

The behaviour of the scattering function is considered as the cylinder's structure (electron density distribution) is systematically varied from the case of a solid cylinder to that of a thin shell. A ten stage electron density strip model is shown to be sufficient for this purpose.

The effects of packing of the cylinders is examined by the use of the swelling factor ( $\delta$ ), and the behaviour of the diffraction pattern due to an array of solid cylinders is used to illustrate the effects of changing  $\delta$ .

The behaviour of the lattice function is examined as the numbers of lattice points in a centred hexagonal array is varied from seven to sixty-one. It is shown that the interference function due to a hexagonal array of thirty-seven points represents a reasonable approximation to the case of the interference function due to an infinite hexagonal array.

The behaviour of the diffraction patterns due to a series of cylinders with various structures in a centred hexagonal array of thirty-seven components is examined as systematic changes to the various parameters are made, and explained in terms of the combined behaviour of those parameters as outlined above.



7934258 01

## CONTENTS

	<u>Page No.</u>
Objective	
Chapter 1 Liquid Crystals	1
Chapter 2 Survey of Previous Work	15
Chapter 3 Model Parameters I	42
The Electron Density Distribution	
Chapter 4 Model Parameters II	74
The Lattice Function	
Chapter 5 Model Parameters III	95
The Swelling Factor	
Chapter 6 Model Diffraction Patterns	103
Chapter 7 Conclusions	118
Diagrams Model Scattering Profiles and Diffraction Patterns	
Appendix A Model Computer program	
Appendix B Conversion of diffraction line positions into equivalent inter-planar spacings	
References	
Acknowledgements	

## OBJECTIVE OF THE STUDY

In the past, identification of the various phase structures formed by amphiphilic liquid crystals has depended mainly on the position of the lines within the diffraction pattern, and additional confirmatory information such as the composition and density of the sample, and the chemical properties of the molecules. It has also been necessary to assess whether or not a particular structure could exist in the light of what else was known about the system under consideration.

The number of diffraction lines recorded depends on the amphiphilic compound, the liquid crystal phase, and the composition. Somewhere between two and seven lines may be observed, but sometimes larger numbers may be seen. When the numbers of lines are few, interpretation of the diffraction pattern may be difficult. Even when large numbers of lines are observed, close proximity may make classification difficult.

Whilst the above approach has led to some measure of success in the identification of the various phases, valuable confirmatory evidence may be excluded by ignoring diffraction line intensities. Due to this, little information relating to the structure of the micelles has resulted. Observation of the change in intensities of the diffraction lines as the concentration of the amphiphiles is varied may provide additional information relating to the micellar structure. This is particularly true in the case of the hexagonal phase.

The objective of the present study is to establish a mathematical model of the scattering of X-rays by the hexagonal phase, based upon arrays of infinitely long structured cylinders. The effects on the position and intensities of the diffraction lines as predicted by the model, and also the manner in which these intensities vary as the type, and separation of the cylinders are changed, are assessed, with a view to providing a tool for the investigation of the hexagonal phase in a more positive and detailed manner.

## 1.1 INTRODUCTION

In the physical world, matter exists in three main states or phases, gas, liquid and solid.<sup>(1,2)</sup> There are however, many materials that exhibit properties belonging to more than one of these phases. Certain of these mesophases, with properties in between those of a liquid and a crystalline solid have come to be known as liquid crystals.

Liquid crystals are most commonly composed of elongated "rod-like" molecules and exhibit a degree of rotational and translational order over a limited range.

The optical properties of liquid crystals<sup>(3,4)</sup> have been studied mostly by the combined techniques of hot-stage and polarisation microscopy, which enables the substances under investigation to be heated to the ranges of temperature in which the mesophases are stable.

The first observations of liquid crystalline behaviour were made at the end of the 19th century, principally by Lehmann and Reinitzer. It was Lehmann who pioneered the use of the polarising microscope in his observations on "plastic crystals", c1877.

## 1.2 CLASSIFICATION OF LIQUID CRYSTALS

The classification and terminology of liquid crystals dates back to the observations made by Friedel c1922. Two types of liquid crystal may be distinguished, those whose behaviour is temperature dependent, and those whose behaviour is solvent dependent. They are known as thermotropic and lyotropic liquid crystals respectively.

## 1.3 THERMOTROPIC LIQUID CRYSTALS

Thermotropic liquid crystals are formed by melting such substances as cholesteryl benzoate, cholesteryl chloride, and cholesterylamine.<sup>(5)</sup> Three major types of thermotropic mesophases may be distinguished, nematic, cholesteric and smectic.

The nematic mesophases derive their name from the thread-like lines that have been observed in them when they have been prepared by rapid cooling of the melt. There is a high degree of rotational order present in the nematic phase and the molecules are aligned parallel to one another. Microscopic examination of the nematic phase shows that several different textures are observed, such as the homogeneous and the homeotropic textures. (6)

As far as is known, all compounds forming cholesteric mesophases have molecules that are asymmetric. In general terms, this provides an explanation of why the mesophases have twisted structures. (7) The absence of a long range translational ordering of the cholesteric phase (as with the nematic) means that the phase is fluid. Over a limited range, there is little physical difference between the cholesteric and nematic phases.

Optical and X-ray evidence show that the chief characteristic of the smectic mesophase (7) is that the molecules are arranged in layers with their long axes, or at least their main directions, normal to the layer planes. As many as eight different smectic mesophases have been identified, of which only three, the smectic A, C and B phases are well documented. (6,8)

Some thermotropic liquid crystals have been observed to pass through more than one mesophase in between the solid and liquid states, for instance, consider a material which has a nematic and three smectic phases. The order of the mesophases occurring will be:-

Solid → smectic B → smectic C → smectic A → nematic → cholesteric  
T increasing →

For compounds having cholesteric and smectic mesophases, the occurrence of the mesophases will be:-

Solid → cholesteric → isotropic

or

Solid → smectic A → cholesteric → cholesteric → isotropic

T increasing →

Experimental evidence for the above has been found, but not for the nematic/cholesteric mesophases.

## 1.4 LYOTROPIC LIQUID CRYSTALS

Lyotropic liquid crystals, as with thermotropics, are highly ordered fluid states that are formed by the penetration of a solvent in between the molecules of a crystal lattice. Many pure substances exhibit thermotropic mesomorphism, but the presence of a solvent is always required for lyotropic mesomorphism. Systems of lipid and water that exhibit lyotropic mesomorphism have also been observed to form thermotropic mesophases at high temperatures.<sup>(9)</sup>

As indicated, lyotropic liquid crystals are systems composed of two or more compounds, and may be mixtures of amphiphilic compounds and a solvent. The amphiphilic molecules themselves are of two main types, those in which the polar group is at the end of a long lipophilic chain, and those in which the polar group is linked to two chains.

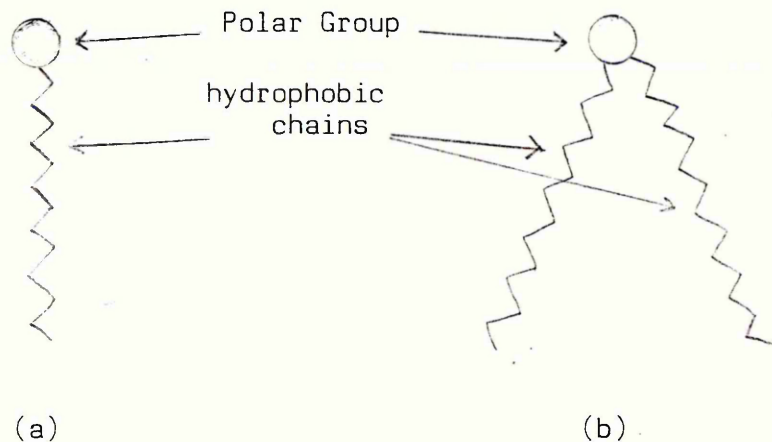


Figure 1

An example of a type (a) molecule is sodium laurate.

Ternary, or three component systems, composed of an amphiphile, water and a water insoluble compound may also form mesophases. Here, the water and water insoluble compound are "solubilised" in one another by the amphiphile, which acts as a co-solvent.

With the binary system (of amphiphiles and water), the tendency of the polar groups to associate with each other and with the water, causes the molecules to form micelles. It is believed that whatever mesophase is formed, the shape of the structure is governed mainly by the polar groups.<sup>(10)</sup> The lipophilic or hydrophobic part of the molecules forming the liquid-like associations.

#### 1.4.1 Conditions for micelle formation

With very dilute amphiphile concentrations, the molecules are uniformly and randomly distributed throughout the solution. As the concentration increases, the amphiphilic molecules start to form groups. Some typical micellar forms are shown below:

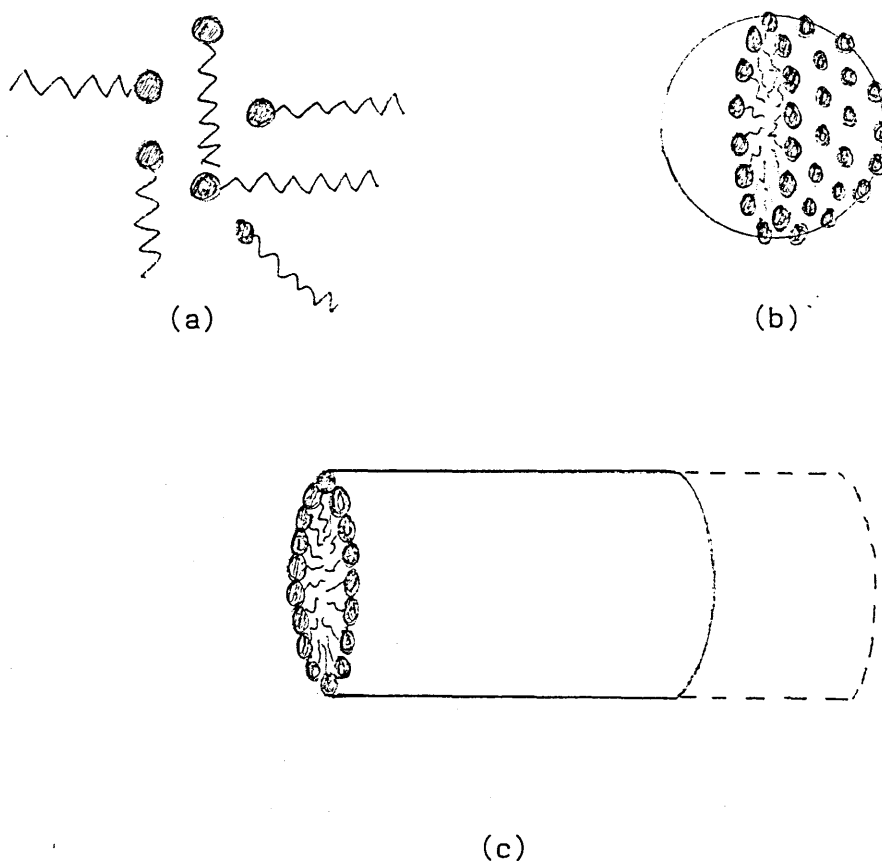


Figure 2

Figure 2(a) represents the randomly distributed amphiphilic molecules at low concentrations. Figure 2(b) and (c) are examples of spherical and cylindrical micelles, respectively, the hydrophobic "tails" of the molecules being grouped within the interiors of the micelles, and are fluid in nature. The structure of the micelles is properly regarded as being of a statistical nature, fluctuating in size and shape, being in an equilibrium state with the surrounding amphiphilic molecules, temperature being a controlling factor.

Further increase in concentration of the amphiphilic molecules results in the formation of lyotropic liquid crystal mesophases, which may take up several different forms. The interior of the micelles may be regarded as pockets of pure liquid hydrocarbon, which is capable of dissolving hydrophobic molecules that are added to the solution. The action of soap as a cleansing agent employs this mechanism.

#### 1.4.2 Lyotropic mesophases

The macroscopic structures of lyotropic mesophases<sup>(11)</sup> are similar to that of emulsions that are stabilised by surfactants. Often they are opalescent in colour and gel-like. Difficulties in discerning the difference between micellar and liquid crystal systems, and heterogeneous dispersions are sometimes experienced, but heterogeneous dispersions do not exhibit X-ray diffraction profiles as do micellar and mesomorphous phases. The interplanar spacings that correspond to the hydrocarbon and aqueous regions vary with the amount of water present in the system.

The state of the hydrocarbon chains in the micelles and mesophases is indicated by the Krafft phenomenon.<sup>(9)</sup> The Krafft point is defined for an aqueous solution to be that temperature at which the solubility reaches the critical micelle concentration. As the temperature rises further, the solubility also rises rapidly, since the molecules form micelles.

Some typical examples of phase diagrams may be found in the Handbook of Liquid Crystals (Verlag Chemie 1980), and also reference (9) (Lyotropic Liquid Crystals, Advances in Chemistry 1976). Ternary systems comprising a surfactant, a slightly polar additive and water, also display many interesting properties.

#### 1.4.2.1 The Neat Phase

It is generally agreed that this phase is lamellar ie smectic with the amphiphile forming double layers separated by water.

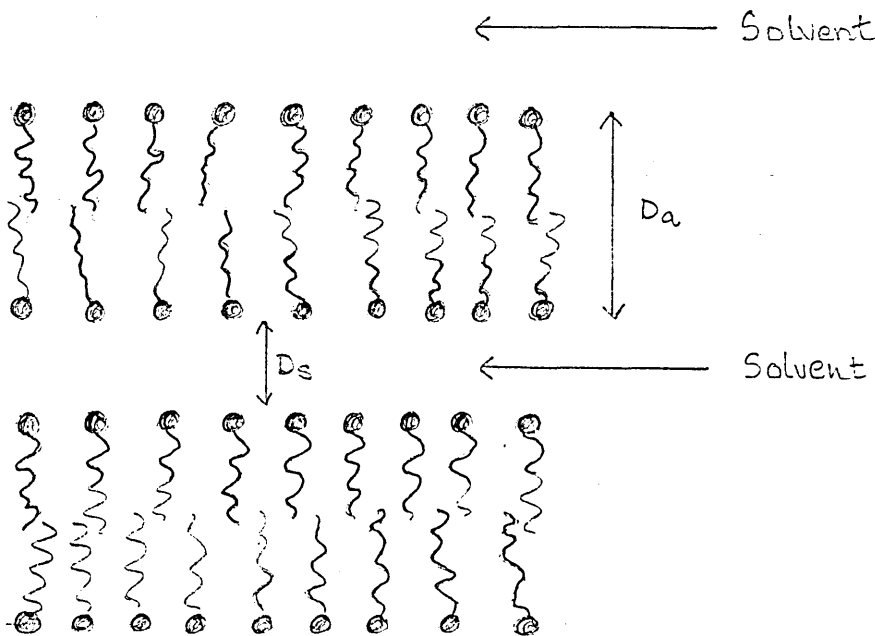


Figure 3

The molecules are arranged with the head groups on both surfaces. These layers are practically of infinite extent (c.f the layer thickness). The double layers are stacked periodically, being separated by solvent. The distance  $D_a$  is less than twice the molecular length, and is of the order 30-40 Å.  $D_s$  is of the order 20 Å.

#### 1.4.2.2 The Middle Phase

The middle phase seems to be formed only from single chain amphiphilic molecules and not of the two chain type. In cases where both the neat and the middle phases are formed, the middle phase is stable at higher water concentrations than the neat phase. X-ray diffraction studies indicate that the molecules are grouped into cylinder-like micelles of indefinite length. These cylinders are arranged in parallel fashion in a 2-D hexagonal array, with water being the intervening medium between the cylinders.

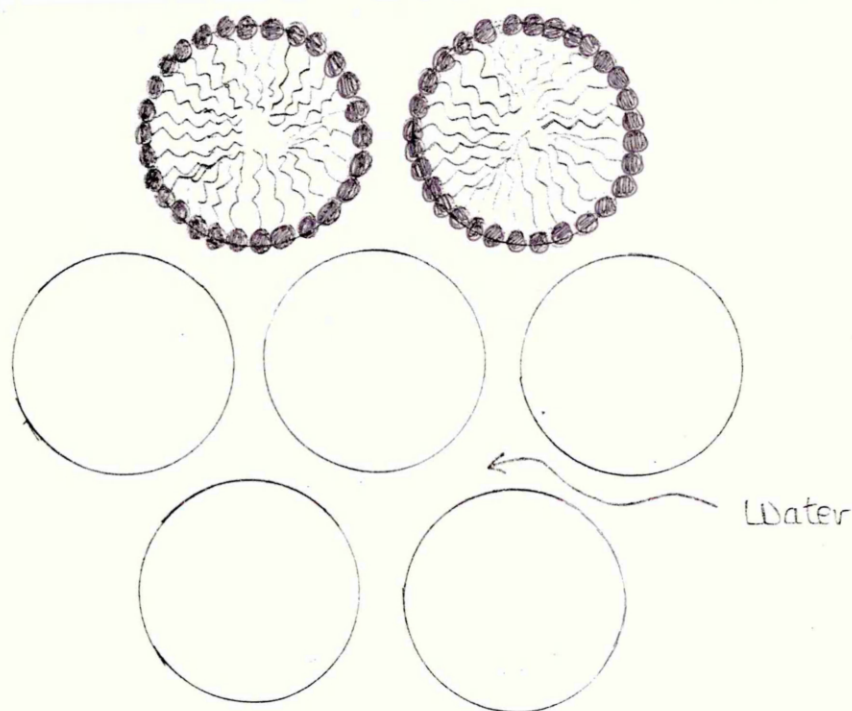


Figure 4

As already noted, the middle or hexagonal phase suffers from a lack of detailed information relating to the micelle's structure, due mainly to the fact that previously only diffraction line positions were considered. Only after consideration of the known physical and chemical properties of the phase, and other supporting information, could a micellar model be proposed with any reasonable degree of certainty.

#### 1.4.2.3 The Viscous Phase

The viscous phase appears in some systems at concentrations in between those within which the neat and the middle phases are stable. The structure of the viscous phase is not well understood. The only information that optical investigation has so far provided is that the phase is isotropic. X-ray studies were originally interpreted to mean that the structure was a face centred cubic lattice. However, more recent studies have shown that the structure is based upon a body-centred cubic lattice.

#### 1.4.2.4 The Isotropic Phase

The isotropic phase has been observed in binary systems of water and such substances as decyl-trimethylammonium chloride, at higher water concentrations than those at which the middle phase has been found to be stable. It has also been observed in certain ternary systems. It is thought to have a primitive lattice.

#### 1.4.2.5 The Inverse Phases

In some lyotropic mesophases, at greater concentrations than those at which the neat phase is stable, the  $V_2$  phase which is also isotropic, occurs. At still higher concentrations the inverse middle ( $M_2$ ) phase is formed. The  $V_2$  phase, as with the neat ( $V_1$ ) phase is not structurally well understood.

The  $M_2$  phase has been found to possess a similar structure to the middle ( $M_1$ ) phase, but of an "inverted" nature. This means that the hydrophobic heads are on the inside of the cylinder, enclosing a water core. The medium in between the micelles must therefore be of a lipophilic nature.

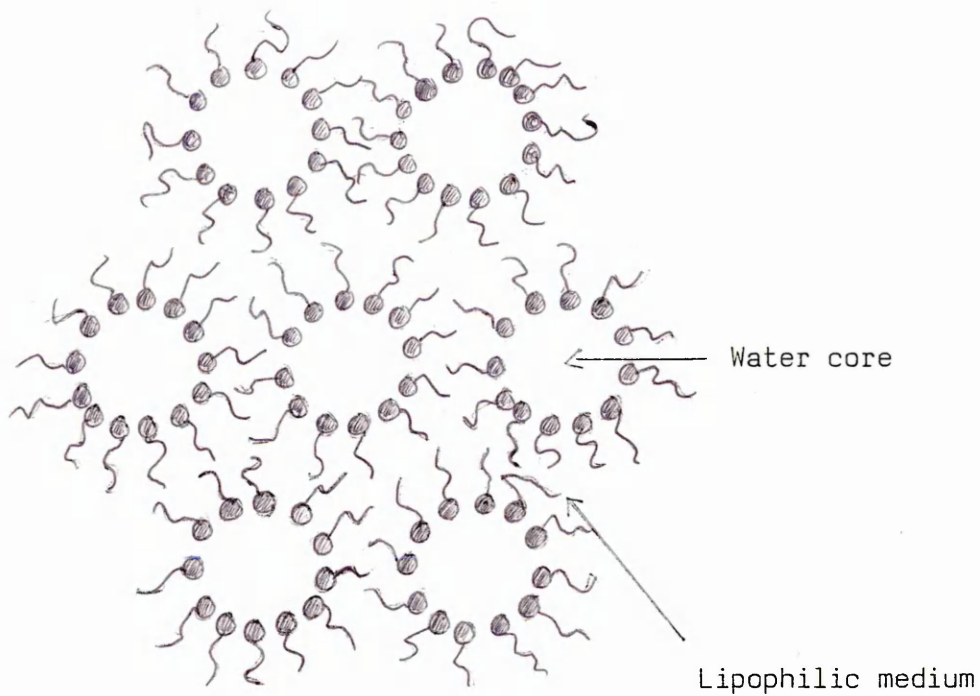


Figure 5

#### 1.4.2.6 Other Phases

Apart from phases with hexagonally arranged micelles, other phases with 2-D periodicity are possible<sup>(11,12)</sup> Luzzati has encountered a rectangular (R) phase present in aqueous amphiphile systems. This phase is characterised by two independent series of interplanar spacings:-  
 $a: a/2 : a/3$  and  $b: b/2 : b/3$ . The ratio between the two repeat distances being dependent on the type of amphiphile, and indicates a 2-D network with two independent parameters.

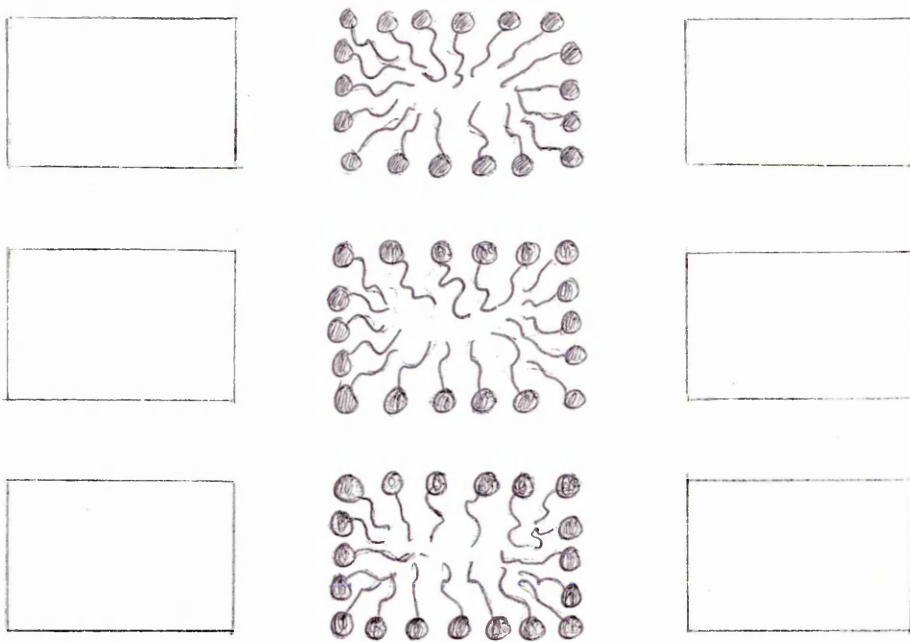
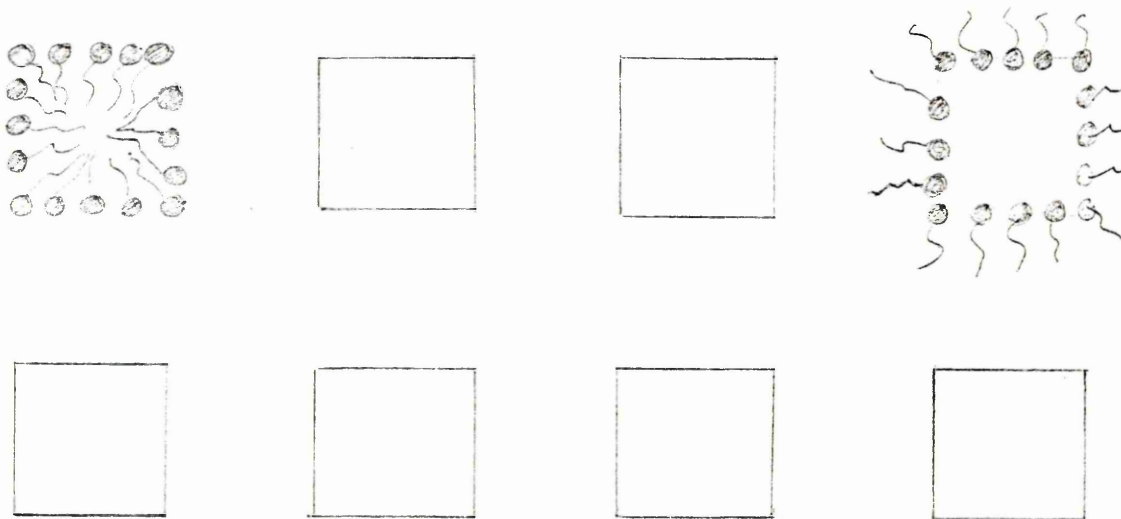


Figure 6

Rectangular phases have also been observed by Ekwall, in systems of potassium soaps. This phase appears between the middle and neat phases.

The case where the parameters  $a$  and  $b$  are equal defines a structure that might be possessed by the C and K phases.



Tetragonal C

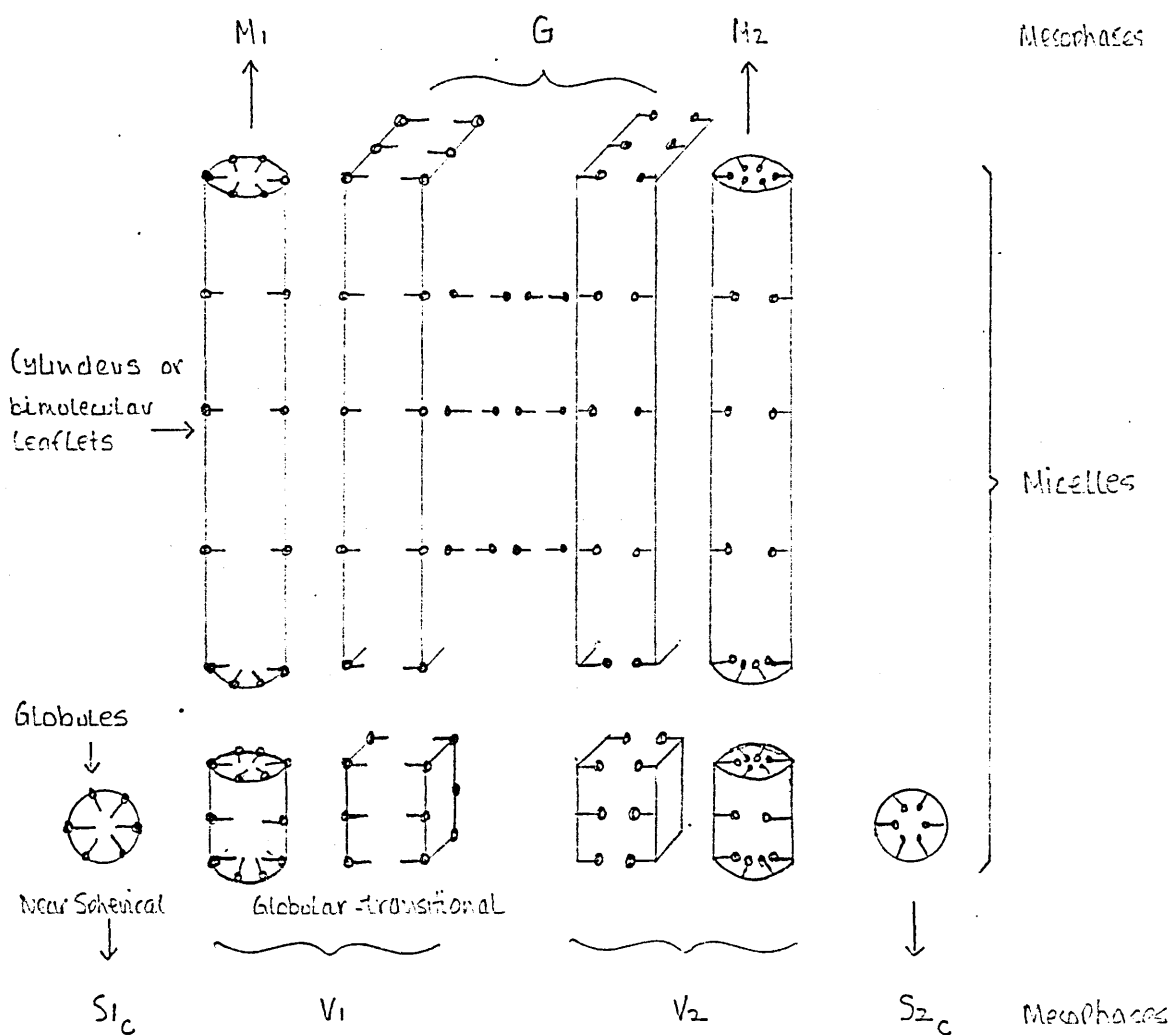
Tetragonal K

Figure 7

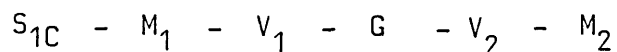
These phases have been observed by Ekwall et al in a number of amphiphilic systems. They observed a series of X-ray reflections with corresponding d-values in the ratios  $1 : \frac{1}{2} : \frac{1}{3}$ . Location of these phases within the phase diagram indicates that the structures of the C and K phases are complimentary. C being normal, whilst the K phase being of an inverted nature. This type of structure implies the presence of a reflection corresponding to the diagonal of the square lattice. This has not been observed.

### 1.5 THE ORDER OF APPEARANCE OF THE PHASES

Consider a binary system, maintained at a fixed temperature, in which the concentration of the amphiphile is allowed to vary. As the concentration of the amphiphile increases, the sequence of appearance of the various phases would be



As shown above, the succession of the phases is:-



This complete series has not yet been found in any single system. Quite often the only sequences observed are G,  $V_2$  and  $M_2$ , or  $M_1$ ,  $V_1$  or G, but whichever phases are present, they always occur in the order defined above.

## 1.6 X-RAY DIFFRACTION AND AMPHIPHILIC LIQUID CRYSTALS

X-ray diffraction techniques have been widely applied to both amphiphilic and non-amphiphilic liquid crystal systems, however, only amphiphilic systems and in particular the hexagonal phase, will be considered further.

As noted earlier, X-ray diffraction data alone has not been sufficient to categorise a structure uniquely. Additional information, such as the composition and density of the sample, the size and shape and chemical composition of its molecules, has been necessary. Even when such data described above has been considered as a whole, a unique definition of the structure may not be possible. Examination of any other relevant information about the system has to be assessed before any valid predictions may be made as to the structure of the sample.

At one time, due mainly to the scarcity of X-ray data, all amphiphilic phases were thought to be of the lamellar type.

Amphiphilic liquid crystal systems tend to have diffraction patterns characterised by a series of sharp reflections corresponding to interplanar spacings in the range 10-100 $\text{\AA}$ , and a wide diffuse reflection at 4.5 $\text{\AA}$ . A system containing water will display an additional diffuse reflection at 3.2 $\text{\AA}$ . Reflections corresponding to large distances or "long" Bragg spacings may sometimes be as sharp as those obtained from well crystallised substances. The number of reflections observed depends on the amphiphile, and on the phase and composition. When few reflections are observed, interpretation of the diffraction pattern may be difficult.

In order to interpret X-ray diffraction photographs, they are treated as powder patterns. The Bragg equation, viz:

$$n\lambda = 2d \sin \theta$$

is used to convert the position of the diffraction lines into interplanar spacings

where  $\lambda$  = wavelength  
d = interplanar spacings  
n = order of reflection  
 $2\theta$  = diffraction angle

The symmetry of the lattice may be determined by finding an equation with which all the observed spacings agree, hence the unit cell dimensions may be calculated.

It is the degree of agreement between the observed and the predicted intensities of reflections that determine the validity or correctness of the proposed structure. Only a small number of reflections are observed in the case of amphiphilic liquid crystals, so that comparisons are difficult to make. However, as will be shown later, it has been possible to make valid comparisons in some cases, when the diffraction patterns were studied as a function of the water content. For a structure that is formed of aggregates of fixed dimensions separated by variable amounts of water, the intensities of the reflections are proportional to the Fourier transform of the aggregates sampled at the lattice sites. In order for a proposed structure to be valid, the ratio of the observed intensities must match the amplitudes of the Fourier transform.

## 1.7 CONCLUDING REMARKS

It has been seen that X-ray crystallographic data alone usually does not provide enough information to make unequivocal statements about a particular structure. It is easy to misinterpret a particular mesophase if only X-ray data is considered. A more reliable approach is to construct a series of phase diagrams. Each phase, and the model associated with it, should progress logically as a consequence of its composition within the sequences of the phases. In addition, the structural parameters resulting from X-ray data based upon the model adopted, should be realistically inter-related.

## 2.1 INTRODUCTION

X-ray diffraction provides a powerful and effective tool for investigating the structure of many materials. It is possible in principle, to determine an exact and usually unique structure for atomic and molecular arrays having 3-D periodicity. However for a liquid, the situation is different, due to the fact that the atoms are not fixed in space but are in constant motion. Hence only a statistical, time averaged distribution can be established. With liquid crystal mesophases, which possess properties intermediate between the solid and the liquid states, it is possible to obtain information about the structure of the mesophase in proportion to the degree of correlation existing along specific directions in the array. It is not generally possible to derive a unique molecular arrangement directly from the observed X-ray data in the case of systems with partial or intermediate ordering. X-ray diffraction photographs tend to be used to distinguish between the various mesophases, but little in the way of information about the molecular arrangements of the particular phase results.

Many attempts have been made to interpret X-ray diffraction data from liquid crystal systems, by the use of highly simplified mathematical models based on cylinders and spheres to represent the meso-aggregates or micelles.

## 2.2 OSTER AND RILEY

Oster and Riley<sup>(13)</sup> applied scattering theory to several idealised models of colloids and macro-molecules, in order to explain the angular scattering due to solutions of such particles. In order to compare X-ray and light scattering by the same system, the dimensionless parameter  $kR$  was introduced, where  $R$  is the radius of the spherical particle, and  $k = (4\pi/\lambda)\sin\theta$ ,  $\lambda$  = wavelength of radiation and  $2\theta$  = angle between the incident and scattered radiation.

Their paper<sup>(13)</sup> also points out that for the simple dipole theory of scattering<sup>(14)</sup> to be applicable, it is a necessary requirement that the refractive index of the particle be nearly the same as that of the surrounding medium. This condition is almost always satisfied in practice with X-rays, and is in the main satisfied by visible light, except for example in the case of metallic colloids which have a high refractive index.

Oster and Riley developed an expression for the scattering of X-rays by a uniform solid sphere, viz:

$$F(kR) = 3 \left[ \frac{\sin(kR) - (kR) \cos(kR)}{(kR)^3} \right] \quad -(1)$$

or expressed in more compact form

$$F(kR) = 3 \sqrt{\frac{\pi}{2}} \frac{J_{3/2}(kR)}{(kR)^{3/2}} \quad -(2)$$

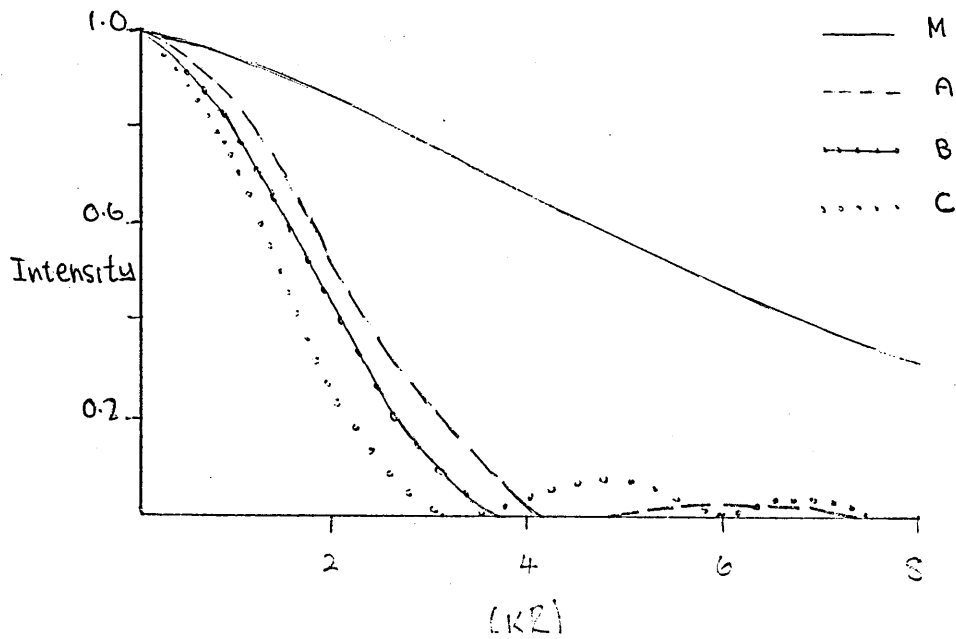
where  $F(kR)$  represents the scattering amplitude and  $J_{3/2}(kR)$  is the spherical Bessel function of order  $3/2$ . Recognising the fact that a solid sphere might not adequately represent certain types of molecular aggregates, Oster and Riley introduced the concept of a variable thickness shell to take this into account. For a shell of thickness  $(1-C)R$ , where  $1 > C > 0$ , then the equation for the scattering due to a spherical shell is given by:

$$F(kR) = 3 \left[ \frac{(\sin(kR) - kR \cos(kR)) - (C \sin(CkR) - CkR \cos(CkR))}{(1-C^3)(kR)^3} \right] \quad -(3)$$

Letting  $C \rightarrow 1$ , the scattering amplitude due to an infinitesimally thin shell is obtained:

$$F(kR) = \frac{\sin(kR)}{(kR)} \quad -(4)$$

The intensity of scattering ( $F^2(kR)$ ) due to various thicknesses of spherical shells obtained by Oster and Riley using equations (3) and (4) are shown below:



M represents the normalised intensity of scattering for independent mercury atoms (included for comparison purposes).

Figure 8

Figure 8, curve B, shows  $F^2(kR)$  for  $C=0.8$  ie for a shell of thickness one fifth the outer radius of the sphere. By letting  $C \rightarrow 1$ , the scattering intensity due to an infinitesimally thin shell is obtained (C), curve(A) represents the scattering intensity due to a solid sphere. As can be seen, the  $F^2$  curves in figure 8 fall off more rapidly the thinner the shell.

When certain conditions are met, colloidal particles and macro-molecules will aggregate together in solution. If the system is sufficiently dilute, then the aggregates may be considered to scatter independently of each other, so that the total observed scattering is just the summation of the intensities scattered by each individual aggregate.

For an aggregate consisting of  $n$  particles, each with scattering faction  $F$ , then the averaged intensity of scattering will be  $F^2(kR)$  multiplied by:

$$\frac{1}{n^2} \sum_i \sum_j \frac{\sin(kr_{ij})}{(kr_{ij})} \quad - (5)$$

where  $r_{ij}$  is the distance between the particles  $i$  and  $j$ . Expression (5) originally due to Debye (1915) was modified by Oster and Riley to include the factor  $(1/n^2)$  to obtain the scattering per particle.

For example, for two spheres in contact, the scattering equation becomes -

$$I = F^2(kR) \left[ \frac{1}{4} \frac{[2 + 2 \sin(2kR)]}{(2kR)} \right] \quad -(6)$$

where  $F^2(kR)$  is the scattering intensity due to the sphere.

Figure 9 shows the normalised intensity of scattering per sphere for independent solid single spheres, (curve A) aggregates of five solid spheres (curve C), and aggregates of two hydrated spheres (curve D).

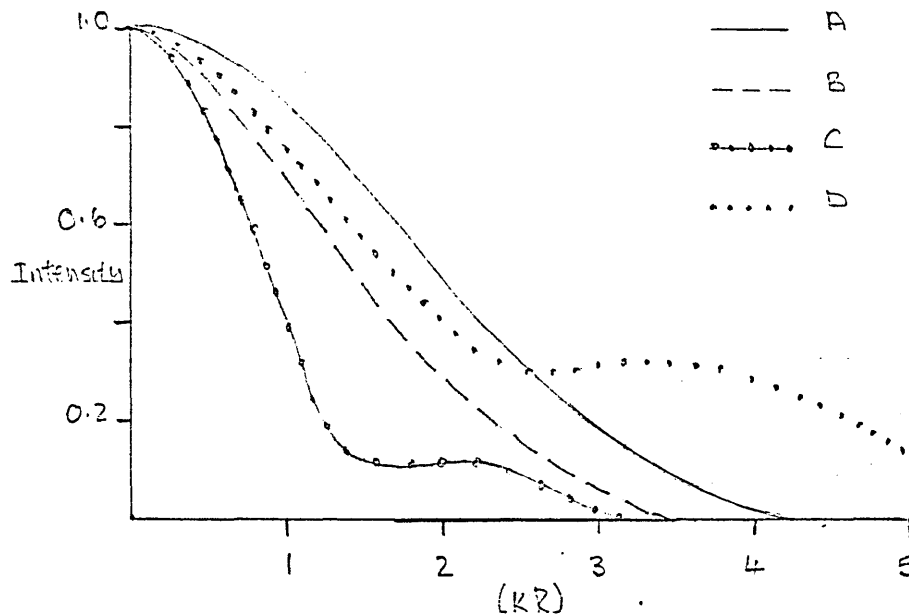


Figure 9

For small values of  $(kR)$ , the scattering intensity falls off more rapidly, the greater the complexity of the aggregate.

In a following paper<sup>(15)</sup>, Oster and Riley considered the scattering due to systems of long macro-molecules, by likening the molecules to rigid, smooth cylinders with internal radial structure, in order to account for the electron density variation within the molecules. The basis for this particular model's approach being argued as follows -

On the macroscopic scale, systems of long particles may be isotropic or anisotropic. Whilst isotropic systems are composed of collections of cylindrically symmetric domains, anisotropic systems have domains with preferred orientations. It was known that very long particles tend to show correlation in orientation even in fairly dilute solutions, thus enabling considerable simplifications to the mathematics of the situation, reducing a 3-D problem to one in 2-D. As a further qualification, the rods or cylinder-like particles were considered to be parallel to each other, within their independently scattering domains. Due to the fact that only two dimensions are considered, the intensity of scattering is localised in a plane at right angles to the axes of the cylinders.

Diffraction patterns for various structured cylinders were produced, the mathematical forms of the solutions being conveniently expressed in terms of the Bessel functions  $J_0(X)$  and  $J_1(X)$ . The nature of the solutions imply that the diffraction patterns must be of an oscillatory nature.

For an infinitely long solid cylinder Oster and Riley obtained the following expression for the scattering amplitude

$$F(kR) = \frac{2 J_1(kR)}{(kR)} \quad \text{-(7)}$$

and for a cylindrical shell of thickness  $(1-C)R$ .

$$F(kR) = 2 \frac{(kR)J_1(kR) - (CkR)J_1(CkR)}{(kR)^2(1-C^2)} \quad - (8)$$

where  $k$  denotes the same parameter used in the earlier Oster and Riley paper<sup>(13)</sup>,  $R$  represents the radius of the cylinder. Both equations (7) and (8) represent the normalised scattering amplitude for both types of cylinders. From equation (8), by allowing  $C \rightarrow 1$ , Oster and Riley obtained the scattering amplitude due to an infinitely thin cylindrical shell:

$$F(kR) = J_0(kR) \quad - (9)$$

Equation (9) is equivalent to the Fraunhofer diffraction by a circular line aperture.

The results obtained, for the cases discussed above, by Oster and Riley, are represented graphically below:

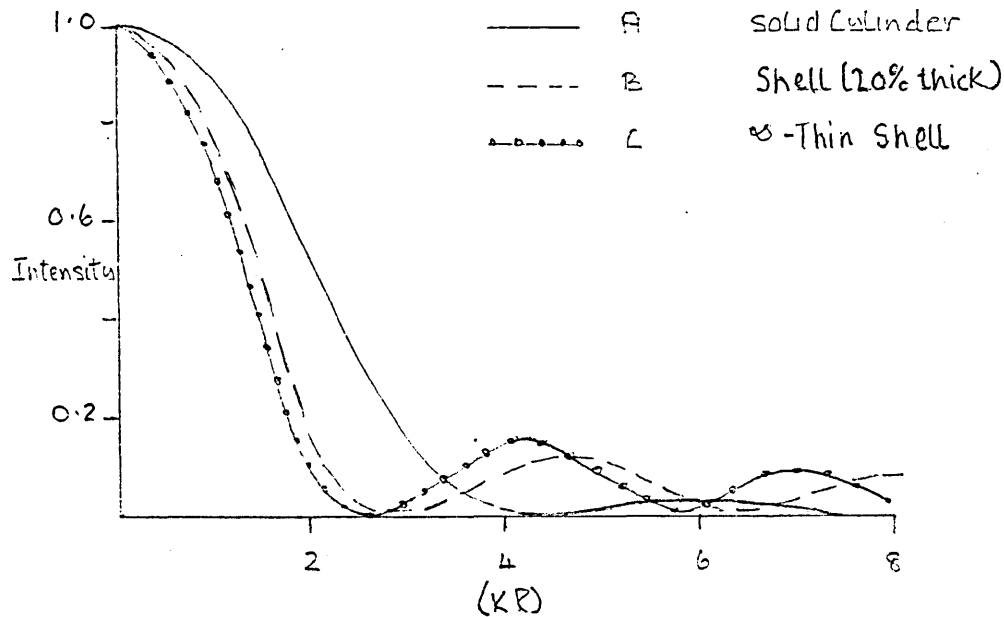


Figure 10

As can be seen from Figure 10, the central peak tends to become sharper as more material is removed from the interior of the cylinder, the first and second subsidiary peaks becoming more pronounced. Oster and Riley showed that for small values of  $(kR)$ , equation (8) may be approximated by the expression -

$$F^2(kR) = 1 - \frac{1}{4} (kR)^2(1 + C^2) \quad - (10)$$

Hence showing that for small values of (kR) the scattering is practically independent of the internal structure of the particles.

Oster and Riley then consider the scattering due to limited assemblies of cylindrical particles. By analogy with Debye, and in similiary manner to their earlier paper<sup>(13)</sup>, the normalised intensity of scattering due to an array of structured cylinders was obtained:

$$I = 1/n^2 F^2(kR) \sum_p^n \sum_q^n J_0(kSpq) \quad - (11)$$

Where Spq = separation of the p,q<sup>th</sup> particles. At this stage, the important concept of the swelling factor ( $\chi$ ) was introduced, being defined by the relation  $\chi = S/2R$ . This was intended to take account of the fact that the cylinders might not always be in contact, owing to inter-particle repulsion or hydration.

For two parallel cylinders, equation (11) becomes:

$$I = 1/2^2 F^2(kR) [2 + 2 J_0(kS)] \quad - (12)$$

and for seven cylinders grouped in a centred hexagonal array, equation (11) becomes :

$$K = 1/7^2 F^2(kR) [7 + 24J_0(kS) + 6J_0(2kS) + 12J_0(\sqrt{3}kS)] \quad - (13)$$

where kS = 2  $\chi$  kR

The normalised intensity of scattering, obtained by Oster and Riley, for several independent aggregates of seven cylinders in a centred hexagonal array, at various values of  $\chi$  are shown below:-

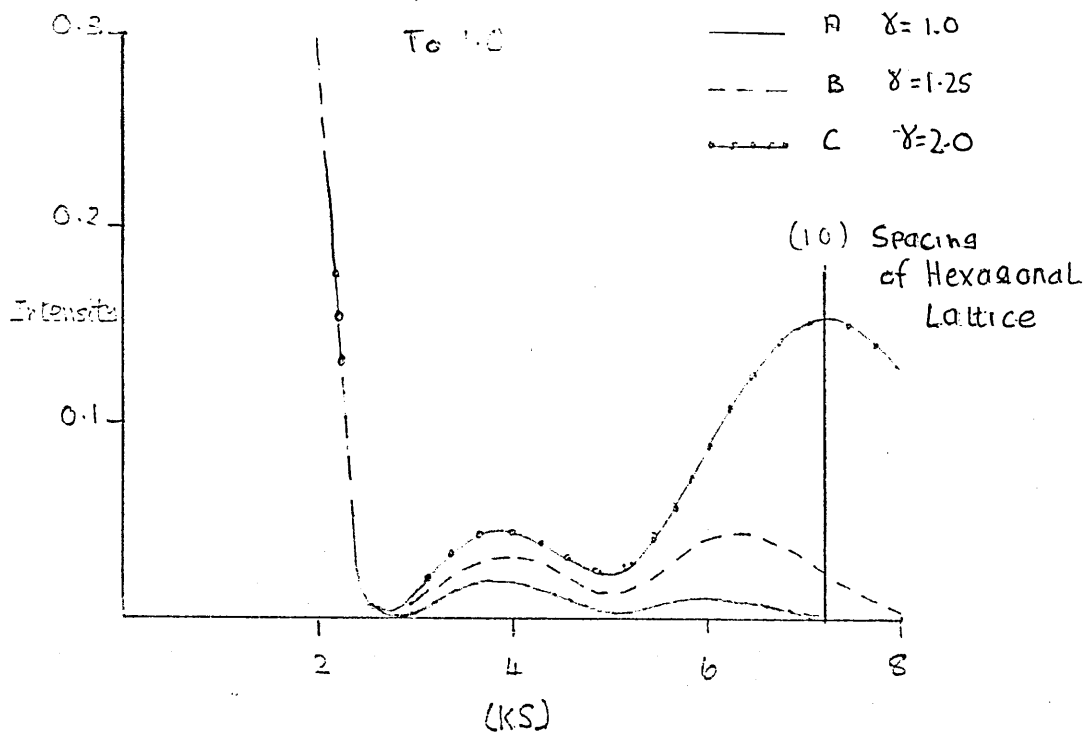


Figure 11

As can be seen from Figure 11, increase in interparticle separation ( $S = 2\gamma R$ ), causes an increase in intensity of the subsidiary diffraction peaks. The second of these subsidiary peaks, moves towards the position corresponding to the (10) planes in a 2-D hexagonal lattice of infinite extent as ( $\gamma$ ) increases. It was noted by Oster and Riley that the first subsidiary peaks shown in Figure 11, have no equivalent in the case of the infinite 2-D lattice. The positions of the diffraction peaks resulting from an infinite 2-D hexagonal lattice may be calculated from standard crystallographic theory.<sup>(16)</sup> See also Appendix B.

### 2.3 BURGE

A diffraction pattern may be envisaged as the combination of two effects, the scattering due to each individual unit cell or cylinder, and the interference of these scattered waves in a manner determined by the spatial distribution of the cylinders.

Burge<sup>(17)</sup>, considered inter-particle interference effects in some detail. Starting with seven points in a centred hexagonal array, and expanding the array or lattice by adding complete hexagonal "rings", Burge produced interference functions for up to eight concentric hexagonal arrays. Each configuration containing  $3t^2+3t+1$  lattice points, where  $t$  = the number of complete hexagonal rings in the array.

The form of the interference function used by Burge was essentially the same as that used by Oster and Riley, (see equation (11)), but in a slightly modified form, viz:

$$T(x) = 1/n^2 [n + \sum_{j=1}^{j_{\max}} b_j J_0(r_j x)] \quad - (14)$$

where  $x = kS$ , and the number of vectors between the cylinders or particles, in any plane parallel to the equational plane of length  $r_j S$ , is  $b_j$ .

The following co-ordinate system was defined by Burge, in which any inter-cylinder vector may be described by two integers  $(l,m)$ , where  $l \geq m \geq 0$ .

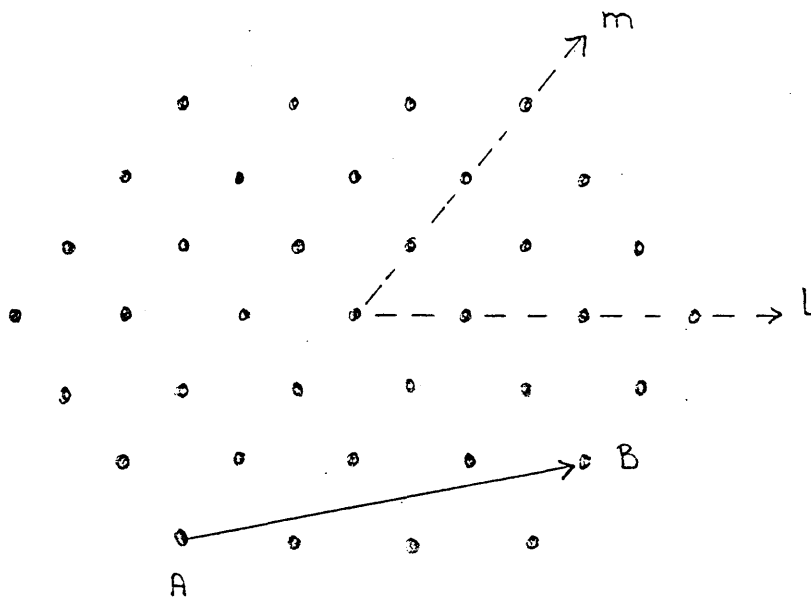


Figure 12

The separation  $r_j$  or  $r_{l,m}$  between lattice points (or the centres of the cylinders) being defined by the relation:

$$r_{l,m}^2 = l^2 + lm + m^2 \quad - (15)$$

For example, from Figure 12, the separation between the lattice points A and B is

$$r_{a,b}^2 = 3^2 + 3 \cdot 1 + 1^2 = \sqrt{13}$$

The following results were obtained by Burge, for a series of interference functions with up to 8 complete rings of points.

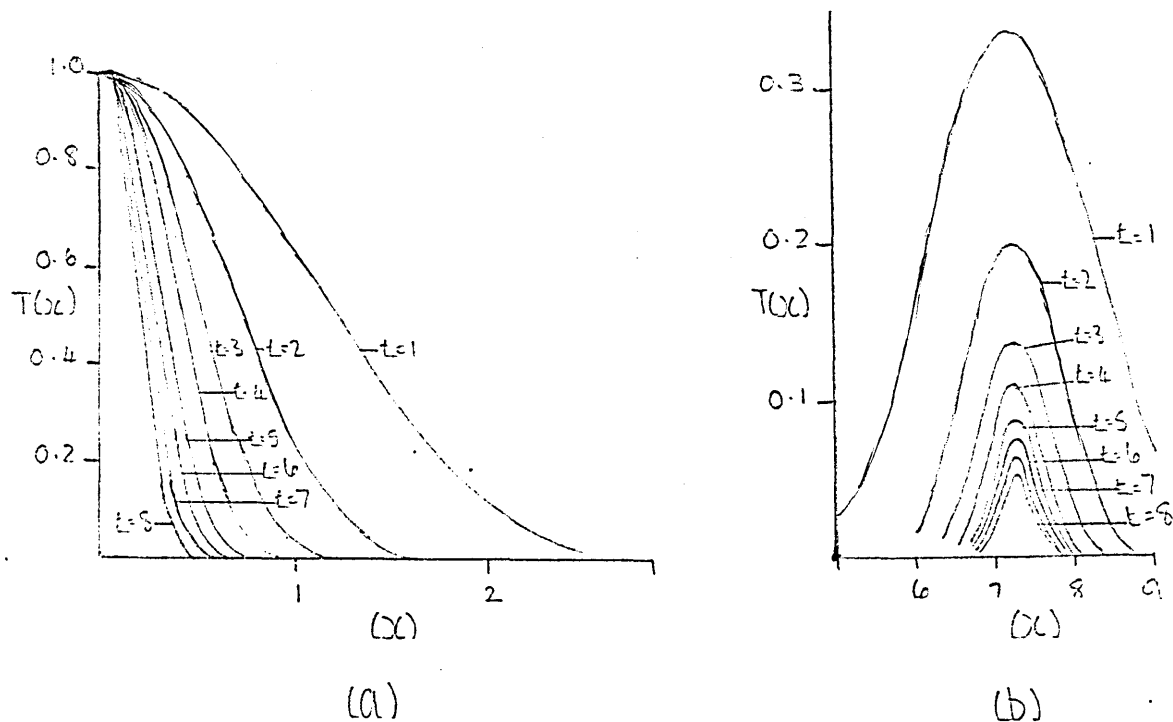


Figure 13

Figure 13 shows the variation of  $T(x)$  with  $x$ , for lattices containing from 7 to 317 points, ie  $t = 1$  to 8, in the ranges (a)  $x = 0$  to  $x = 3$ , and (b)  $x = 5$  to  $x = 9$ . As can be seen from the diagram, the more points included in the lattice, the sharper the main peak becomes. Also note that due to the factor  $(1/n^2)$ , the more points that are added to the lattice, the less intense the peaks become, as shown by Figure 13b. It may also be seen from Figure 13b that as the number of lattice points is increased, there is a progressive movement in the position of the peaks towards the equivalent (10) position of an infinite 2-D hexagonal lattice.

Two subsequent papers by Burge<sup>(18,19)</sup> introduced a modified form of the interference function. The first of these papers<sup>(18)</sup>, discussed the structure of bacterial flagella, and introduced the concept of different levels of ordering of the lattice, the model was defined as follows:

Let the normalised, cylindrically averaged intensity of equatorial X-ray scattering from a molecular unit be  $F^2(kR)$ . Suppose that  $S$  of these identical units be arranged into a filament, and let  $m$  filaments be arranged into a flagellum, furthermore let  $n$  flagella be associated into a coherent bundle, forming the specimen. Thus, according to Burge, the normalised, cylindrically averaged scattered intensity is given by the expression:

$$I(kR) = F^2(kR) T(U) T'(U) T''(U) \quad - (16)$$

$$\text{where } T(U) = 1/S^2 \sum_p^S \sum_q^S J_0(kU_{pq})$$

$$T'(U) = 1/m^2 \sum_{p'}^m \sum_{q'}^m J_0(kU_{p'q'})$$

$$T''(U) = 1/n^2 \sum_{p''}^n \sum_{q''}^n J_0(kU_{p''q''})$$

The  $p$ th and  $q$ th units within a filament being separated by a distance  $U_{pq}$  in the equational plane, the  $p'$ th and  $q'$ th filaments are separated by  $U_{p'q'}$ , and the  $p''$ th and  $q''$ th flagella by  $U_{p''q''}$ .  $J_0(kU_{pq})$  etc being the zero order Bessel functions.

Four rotation axes are implied by the form of equation (16), the centre of the scattering unit, the centre of a filament the centre of a flagellum, and the centre of the lattice within which the flagella are packed.

The X-ray diffraction predicted by the use of the above model, thus arises from three different systems in which short range order exists, and consequently X-ray reflections may occur at spacings not found in extended structures. Burge developed expressions for interference functions with numbers of components ranging from 2 to 10, corresponding to the models shown below:

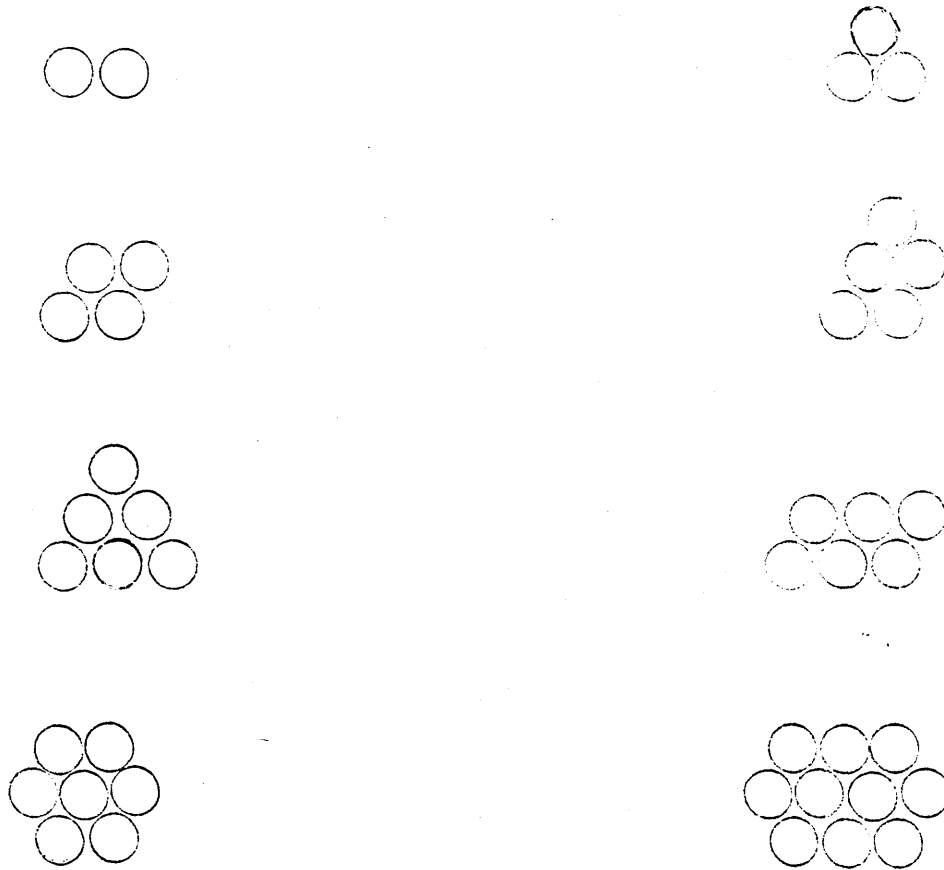


Figure 14

The interference functions corresponding to the various structures above, being given by:

$$T(U) = 1/2^2 [2 + 2J_0(kU)] \quad - (17)$$

$$T(U) = 1/3^2 [3 + 6J_0(kU)] \quad - (18)$$

$$T(U) = 1/4^2 [4 + 10J_0(kU) + 2J_0(\sqrt{3}kU)] \quad - (19)$$

$$T(U) = 1/5^2 [5 + 14J_0(kU) + 4J_0(\sqrt{3}kU) + 2J_0(2kU)] \quad - (20)$$

$$T(U) = 1/6^2 [6 + 18J_0(kU) + 6J_0(\sqrt{3}kU) + 4J_0(2kU) + 2J_0(\sqrt{7}kU)] \quad - (21)$$

$$T(U) = 1/7^2 [7 + 24J_0(kU) + 12J_0(\sqrt{3}kU) + 6J_0(2kU)] \quad - (22)$$

$$T(U) = 1/10^2 [10 + 38J_0(kU) + 22J_0(\sqrt{3}kU) + 16J_0(2kU) + 12J_0(\sqrt{7}kU) + 2J_0(3kU)] \quad - (22)$$

The first model (model 1) proposed by Burge to describe the X-ray diffraction from bacterial flagella was that the scattering unit was taken to be a single  $\alpha$ -helix. A filament was taken to be composed of 19  $\alpha$ -helices in a centred hexagonal array. The interference function being given by:

$$T(U) = 1/19^2 [19 + 84J_0(kC) + 54J_0(2kC) + 24J_0(3kC) + 6J_0(4kC) + 60J_0(\sqrt{3}kC) + 72 J_0(\sqrt{7}kC + 24J_0(\sqrt{13}kC) + 18 J_0(2\sqrt{3}kC)] - (23)$$

where C = separation between centres of nearest neighbours.

A trigonal array of 3 filaments, with separation b between centres, was taken to represent a flagellum, with corresponding interference function:

$$T'(U) = 1/3^2 [3 + 6J_0(kb)] - (24)$$

A coherent array of three flagella, with separation v between centres, having the interference function

$$T''(U) = 1/3^2 [3 + 6J_0(kv)] - (25)$$

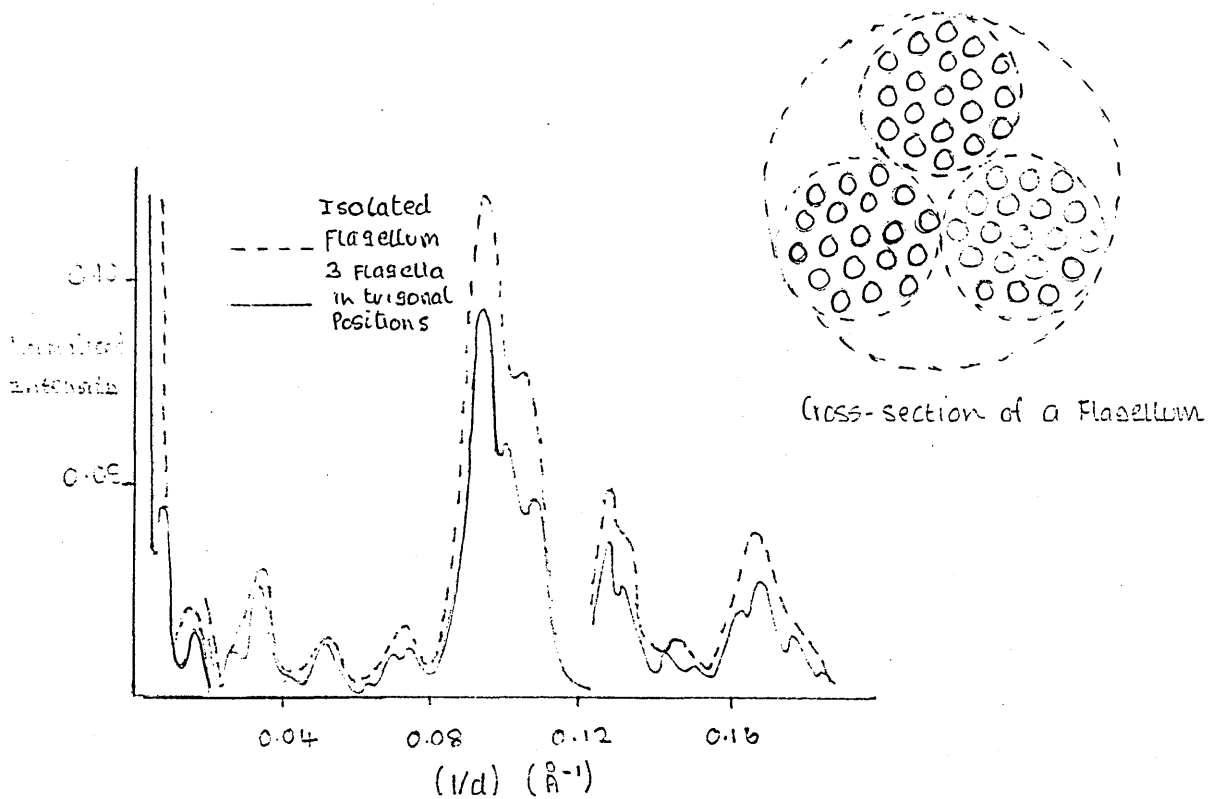
So that the complete scattering equation being composed of equations (23), (24) and (25) becomes:

$$I^2(kR) = F^2(kR) T(U) T'(U) T''(U) - (26)$$

where  $F^2(kR)$  representing the scattering function due to the  $\alpha$ -helix.

Various values for the ratio b/c were taken and the corresponding intensity curves calculated. Scattering by a single flagella was found to be sensitive to this ratio.

Figure 15 shows the normalised, cylindrically averaged, intensity of scattering by an isolated flagellum, and a coherent aggregate of three flagella in trigonal positions.



Model 1 In both curves the scale has been changed in the ranges  $0.02 - 0.12 \text{ \AA}^{-1}$ , and  $0.12 - 0.16 \text{ \AA}^{-1}$ . The ordinate of the curve for --- should be  $\div 10$  in the range  $0.02 - 0.12 \text{ \AA}^{-1}$ , and  $\div 100$  in the range  $0.12 - 0.16 \text{ \AA}^{-1}$ . For — the ranges should be  $\div 20$ , and  $\div 200$  respectively.

Figure 15

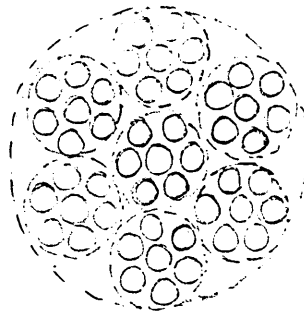
In the second model (model 2) considered by Burge, each filament was assumed to be composed of seven  $\alpha$ -helices, and seven filaments were assumed to make up a single flagellum. This means that the interference functions  $T(U)$  and  $T'(U)$  are of the same form:

$$T(U), T'(U) = 1/7^2 [7 + 24J_0^c(Kb) + 12J_0^c(\sqrt{3}kb) + 6J_0^c(2Kb)] - (27)$$

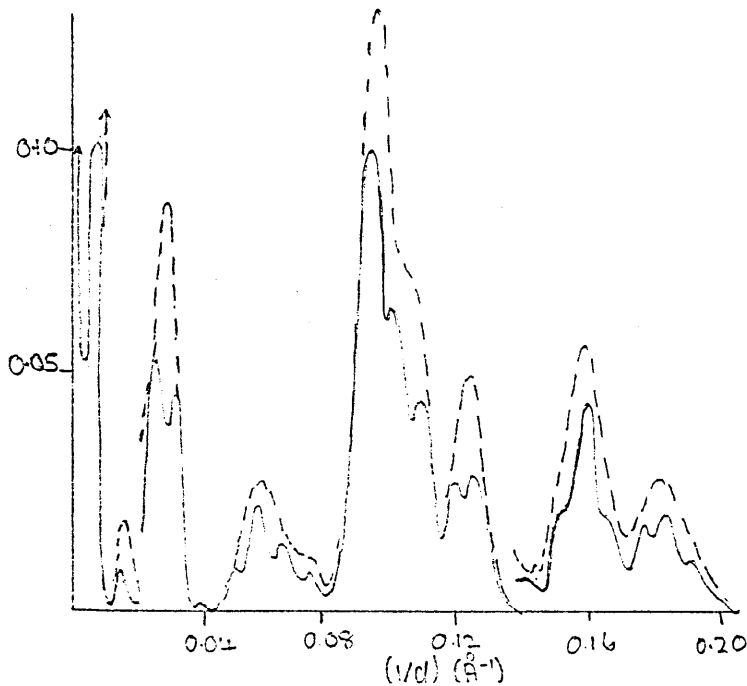
$c$  = separation of  $\alpha$ -helices within a filament

$b$  = separation of filaments within a flagellum

Figure 16 shows the results obtained by Burge for the model 2 case.



Cross-section of a Flagellum



----- Isolated Flagellum

———— 3 Flagella in triangular positions

Model 2 In both curves the scale has been changed in the ranges  $0.02-0.14 \text{ \AA}^{-1}$  and  $0.14-0.20 \text{ \AA}^{-1}$ . The ordinate for the ----- curve  $\pm 5$  in the range  $0.02-0.14 \text{ \AA}^{-1}$  and  $\pm 50$  in the range  $0.14-0.20 \text{ \AA}^{-1}$ . For ——— the ranges should be  $\pm 10$  and  $\pm 100$  respectively.  
Figure 16

In order to account for certain observed reflections, Burge modified model 1 by the introduction of small systematic departures at the level of the filament, ie a cylindrical lattice of 19 components was considered in contrast to a hexagonal lattice with the same number of components.

It was found by Burge that the general features of both the cylindrical and hexagonal forms of  $T(U)$  were similar, but in the cylindrical case certain values of  $T(U)$  were enhanced by a factor of three compared to the corresponding values of  $T(U)$  for the hexagonal case.

Both of the models evaluated by Burge gave reasonable agreement with experimental data in terms of both positions and intensities of the equatorial diffraction lines. However on the basis of observed diffraction evidence, model 2 gave marginally the better results, but by allowing lattice distortion effects at the T(U) level, as described above, model 1 could not be discounted.

In the second of the two papers<sup>(19)</sup>, Burge applied the approach outlined above to the proteins, feather keratin and f-actin. The problem of the number of filaments to include in the array was approached by trial and error. Comparison of experimental and theoretical data showed that a fibril composed of seven filaments gave the closest match in the case of feather keratin. As no specific model was available for the molecular unit, it was taken to be a uniform solid cylinder.

Burge also pointed out that for a restricted hexagonal lattice, non-Bragg maxima are possible at spacings higher than the (10) spacing of the infinite 2-D hexagonal lattice.

#### 2.4 LUZZATI AND CO-WORKERS

Luzzati et al,<sup>(20)</sup> discussed the liquid crystalline phases of amphiphile/water systems, in a general way, distinguishing the various phases by the positions of the X-ray diffraction lines, and by observing the effects of temperature on the diffraction patterns, were able to deduce the structure of the paraffin chains of the amphiphilic molecules.

The above evidence enabled Luzzati to make certain predictions about the nature of the various phases, for example, the middle phase being composed of a series of cylindrical particles of indefinite length, the separations of which being governed by the diffraction line spacings. The radius of the cylinder being obtained via the concentration and the partial specific volume of the amphiphile.

A subsequent paper<sup>(21)</sup> examined the characteristics of the various phases separately, by the use of the combined techniques of polarisation microscopy and X-ray diffraction. It was noted that only a relatively small number of diffraction lines were recorded for the various phases, three lines being recorded in the case of the middle phase, and only two for the lamellar phase. For the hexagonal phase, the intensities of the diffraction lines were found to be dependent on the concentration of the amphiphiles, the (10) reflection always being present and of large magnitude, whilst the (11), (20) reflections were observed to vary in magnitude, the (11) reflection tending to zero intensity at high concentrations, whilst the (20) reflection was at first appreciable, then diminished, and finally increased in intensity as the concentration increased.

The model electron density distribution used by Luzzati was based upon the structured cylinder model proposed by Oster and Riley.<sup>(13)</sup>

In a further paper, Luzzati and Reiss-Husson<sup>(22)</sup> presented an interpretation of absolute low-angle X-ray scattering by micellar solutions of soaps and detergents in water, pointing out that if the scattered intensity is determined only on a relative scale, interpretation of the data may only be carried out with reference to some arbitrary model.

They also pointed out that in the past, in order to facilitate the interpretation of the diffraction patterns from micellar solutions, simplified mathematical models, whose structure was concentration independent, were put forward.

By contrast, it was claimed that low-angle X-ray scattering, measured on an absolute scale should provide a more precise and systematic structure analysis, the basis of the method being to compare the recorded angular scattering by an amphiphile solution to the total energy present in the incident X-ray beam. By comparing a series of curves of absolute scattering intensity versus scattering angle at various concentrations, for a particular amphiphile, Luzzati and Reiss-Husson were able to deduce micellar shape and dimensions.

In an attempt to solve the phase problem in relation to the study of biological membranes, Luzzati and Tardieu<sup>(23)</sup> used a pattern recognition approach. The mathematical technique of which was equivalent to looking at all the possible Fourier transforms consistent with the amplitude of the reflections and recognising the most satisfactory one. In contrast to the usual methods that seek to determine phase as a function of the experimental data, their method consisted in generating all possible combinations of phase values. These phase values are then screened in accordance with a set of criteria related to some of the known, or postulated properties of the system under consideration.

These unknowns are determined by consideration of previous crystallographic evidence, and known physical and chemical properties of the compounds under examination. More importantly the method relies on the structure under examination being centro-symmetric.

This technique of pattern recognition was claimed to offer significant savings in the time required to analyse a particular structure, over the traditional method of generating the Fourier transform from the experimental evidence.

## 2.5 BLAUROCK AND WORTHINGTON

Blaurock and Worthington<sup>(24)</sup> considered the treatment of X-ray diffraction data from planar and concentric multilayered biological structures, such as retinal rods, nerve myelin, and other fibrous proteins such as collagen. These structures have well defined repeating units, with linear or repeat distances of order 300-400 $\text{\AA}$ . Whilst the low-angle spacings provide information about the lattice or repeat structure, the X-ray intensities convey information about the large scale structure of the unit cell.

The purpose of the paper was to derive a relation between the integrated intensities and the Fourier transform of the unit cell, in order to test the validity of a proposed model against the observed X-ray data.

The relation between the Fourier transform of the unit cell and the integrated intensities being defined as follows:

$$I(h) \propto \Delta(h) |T(h)|^2 \quad - (28)$$

where  $h$  is an integer defined by the relation  $a^* = h/d$ , and  $a^*$  represents reciprocal space co-ordinates.

In order to obtain  $|T(h)|$  from the intensity  $I(h)$ , the value of  $\Delta(h)$  must be found.

Blaurock and Worthington set out to obtain  $\Delta(h)$  for various structures possessing rotational symmetry. As they pointed out, difficulty is encountered in recording sufficient data to ensure adequate resolution of the Fourier synthesis. The resolution available is  $\sim d/2h_0$ , where  $h_0$  is the largest order of diffraction recorded. The value of  $h_0$  is determined by many factors, but  $\Delta(h)$  also influences the number of orders recorded. In the case of collagen, for example, up to twenty-five orders may be recorded.

In a further paper, Worthington<sup>(25)</sup> considered the interpretation of low-angle X-ray data from planar and concentric multi-layered structures by the use of 1-D electron density strip models. When a low-angle diffraction pattern is recorded, only a limited set of intensities,  $J(h)_{\text{obs}}$  are obtained. The problem is to deduce an accurate structure from these values.

Worthington also compared the Fourier synthesis method to the model approach as follows. In the Fourier synthesis approach, the phase must be determined, and a Fourier series representation must be computed. However, with the model approach, the predictions of a proposed model must be compared to the experimentally obtained values  $J(h)_{\text{obs}}$ .

As already stated, the Fourier synthesis approach requires knowledge of the systems phases, which have to be determined by the use of heavy atoms, or from shrinkage or swelling phenomena. Phases are not easily obtained in low angle X-ray studies. Hence the phase problem poses a definite limitation to the Fourier synthesis technique. Even if the phase problem were solved, interpretation of the Fourier synthesis in terms of absolute electron densities remains.

Due to this limited resolution of the Fourier synthesis technique, and the absence of absolute electron density information, the preferred method is to test a proposed electron density strip model against the observed data  $J(h)_{\text{obs}}$ .

Worthington pointed out that in order to advance a suitable model, that physical and chemical data such as microscopy, birefringence and composition need to be considered.

In order to assess the validity of such a model, Worthington defined the R value -

$$R = \frac{\sum | [ J'(h)_{\text{calc}} ]^{\frac{1}{2}} - [ KJ(h)_{\text{obs}} ]^{\frac{1}{2}} |}{\sum | [ KJ(h)_{\text{obs}} ]^{\frac{1}{2}} |} \quad - (29)$$

where  $J'(h)_{\text{calc}}$  = calculated diffraction intensities

$J(h)_{\text{obs}}$  = observed diffraction intensities

$K$  = normalisation factor - converts observed data to absolute values.

The value of R should be close to the error in obtaining  $[J(h)_{\text{obs}}]^{\frac{1}{2}}$ . However, even if the R value obtained from a particular model satisfies the above criterion, the question as to whether or not the proposed model is the correct one still remains. All the features of the proposed model should be in keeping with the known physical and chemical properties. Also, a sharp minimum in the value of R should be observed as the model's parameters are varied. If several models were shown to fit the above conditions satisfactorily, the one with the smallest R value should be taken to represent the unit cell.

Use of the R factor defined by Worthington has been made by several workers, (26,27,28,29) notable amongst them being Luzzati in investigating the structure of low density lipo-proteins and by Blaurock and Nelander in investigating the disorder in nerve myelin.

Application of an electron density strip model was made by Blaurock<sup>(30)</sup> in a paper discussing the diffraction of X-rays from a lipid bi-layer with added protein molecules. The paper showed that the effect of adding small amounts of protein to one or both surfaces of the bi-layer causes a cross-interference effect, or a ripple in the diffraction pattern. It was claimed that the amount, thickness and distance of the protein layer from the bi-layer can be predicted from the observed ripple.

The problem of deciding whether the protein is on one or both sides of the layer is not quite so easy to accomplish. This difficulty may be overcome to a certain extent by carefully recording and measuring the intensity near the centre of the diffraction pattern, only then may the structure be inferred with reasonable accuracy. When large amounts of protein are added, profound changes in the diffraction pattern are said to result.

As an example of a typical electron density profile considered by Blaurock, Figure 17 shows a bi-layer membrane with protein added to one side in a saline environment.

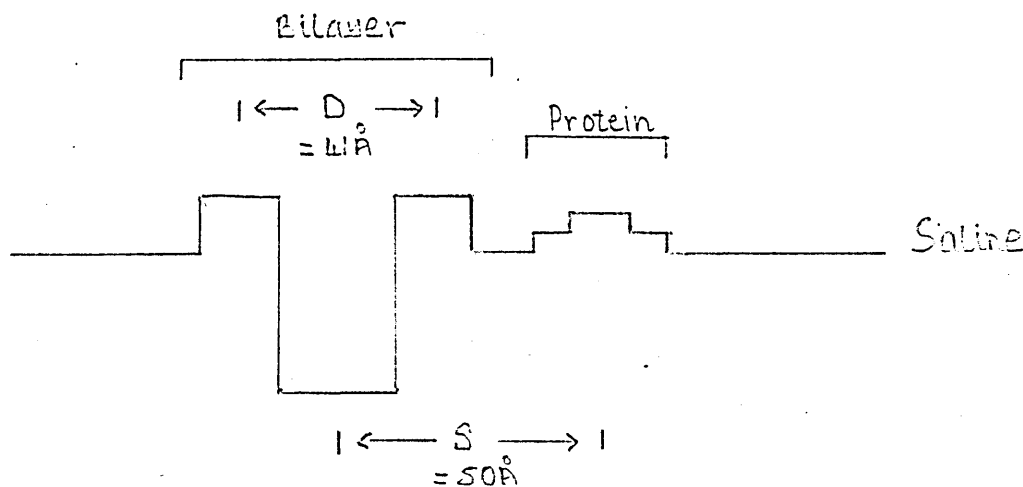


Figure 17

In arriving at the model, Blaurock made certain simplifying assumptions were made. First that the bi-layer and the protein layer were parallel to one another spaced a distance  $S$  apart, and second that both profiles were symmetric.

Blaurock noted that the effect of increasing the separations between the bi-layer and protein increases the frequency of the ripple in the diffraction pattern, and by allowing the protein layer to "thicken-up" has the effect of damping out the ripple near the origin. If the value of  $S$  had been unknown previously it could be estimated from the diffraction pattern ripples.

Blaurock concluded the paper by noting that the principal agent leading to the form of the diffraction pattern is the contrast between the average electron density of the protein and the surrounding water. Consequently, the diffracted intensity will be strongest near to the origin, falling off to a low value near the Bragg spacing equal to the half width of the protein layer profile. Beyond this it was noted, small subsidiary bands may be present. With the lipid bi-layer, it is the contrast between the average electron densities of the head groups and the fatty chains that determine the structure of the X-ray diffraction pattern, being of low intensity near the origin, but when the head group layers are well defined, produce an exclusive series of diffraction bands.

The validity of the theory put forward above by Blaurock<sup>(30)</sup> was put to the test in a further paper<sup>(31)</sup>, which discussed the structure of a lipid-cytochrome C membrane. After adding cytochrome C to lipid vesicles, the predicted ripple in the diffraction pattern was observed. Analysis of this ripple enabled the confirmation of the structure proposed by earlier workers.<sup>(32,33)</sup>

## 2.6 LESSLAUER

Lesslauer<sup>(34)</sup> considered X-ray diffraction by various systems of fatty-acid multilayers, such as barium stearate and barium myristate, the multilayers being treated as simple trial structures, in order to investigate low-angle diffraction experiments with biological membranes.

Fourier syntheses were then carried out (using scaled amplitudes of the structure factors), on the experimental data, providing electron density maps of the bilayer profiles on an absolute scale of electron density. The electron density maps adopted as the correct models for the bilayers were selected by consideration of the known physical and chemical properties of the multilayers. The main criterion for the selection of the appropriate Fourier map being that it should have a region representing a flat hydrocarbon core.

Lesslauer found that for all of the barium and magnesium stearate multilayers that were considered, there was only one Fourier synthesis out of the many possible solutions that gave a flat region in the electron density profile that could be attributed to the hydrocarbon core of the bilayer.

The scaling factors needed in order to derive the absolute electron densities from the Fourier maps were calculated, in the manner of Worthington<sup>(25)</sup>, from the known chemical properties of the compounds.

In his concluding remarks, Lesslauer stated that low-angle X-ray diffraction provides a significant advantage over microscope techniques in the study of biological membranes, because no prior sample preparation such as fixation, staining or dehydration needs to be done.

What remains essential is to show that not only the X-ray spacings, but also the intensities of the recorded diffraction data, contain reliable information relating to the structure under study. This can only be done by investigating simple trial structures, hence inferring the structures of the more complex biological membranes for which they act as models.

In a further paper,<sup>(35)</sup> Lesslauer considered the angular width of the X-ray diffraction peaks from fatty-acid multilayers with few unit cells. The purpose being to observe how the width of the diffraction peaks varied as the number of unit cells in the system was changed, this number being known from the method of preparation.

The theoretical basis for the model being that for a structure with few unit cells, the form of the diffraction pattern is determined by the scattering function of the unit cell being sampled at specific points (of the reciprocal lattice) by an interference function whose main peaks possess finite width due to the low numbers of unit cells.

X-ray diffraction data was recorded from barium stearate multilayers, with numbers of layers (N) ranging from 2 to 10. It was observed that the positions of the main diffraction peaks, although shifting slightly, did not significantly depend on N.

By selecting a single, well defined diffraction peak (ie strong and with equal levels of background radiation on either side of the peak), Lesslauer clearly demonstrated that the angular width of the diffraction peaks varies as  $(1/N)$ .

It was also noted that for small N ( $\geq 2$ ), secondary diffraction peaks were observed, in the regions in between the main lamellar peaks, the existence of which increased the difficulty of finding the true minima on either side of the main peaks.

By observing that the change in width of the diffraction peaks, as the number of unit cells vary, was due to the Structure Factor  $|^2$  being sampled at the reciprocal lattice points, Lesslauer noted that direct analysis of the diffraction pattern due to a multilayer was feasible, since the number of unit cells (N) was known exactly.

## 2.7 SUMMARY OF PREVIOUS WORK

Oster and Riley, after introducing the concept of the structured cylinder as a scattering unit, only considered the two extreme cases of the solid cylinder and the infinitely thin shell, in various simple arrays with various packings of the cylinders. In consequence, there is a lack of information relating to arrays of cylinders with structures intermediate between the limiting cases described above, and since the scattering profile due to the solid cylinder is substantially different to that of the thin shell case, predictions made on the basis of the above models, for these intermediate cases, may be misleading.

Burge, in examining the effects of inter-particle interference in close packed hexagonal arrays, introduced the concept of the multiple interference function, but did not consider model scattering units.

The work of Luzzati and co-workers serving to identify the various liquid crystalline phases, and to make general predictions as to the structures of these phases, Their predictions being based on a combination of X-ray diffraction data (mainly diffraction line positions) and supporting chemical and physical data. In the study of biological membranes, Luzzati used the method of pattern recognition in order to solve the phase problem. Again possible structure solutions being proposed after consideration of the relevant physical and chemical data.

Blaurock and Worthington outlined the usefulness of the electron density strip model in considering the treatment of X-ray diffraction data from concentric multi-layered systems. The modifications to the diffraction pattern due to a lipid bi-layer, by the addition of protein molecules to the system, was considered by Blaurock, noting in the investigation that the form of the diffraction pattern was due to the contrast between the electron density of the protein and the surrounding water medium.

Lesslauer used the concept of a model, this time due to an actual fatty-acid multi-layer, in order to investigate the low-angle X-ray diffraction experiments with biological membranes, using the Fourier synthesis technique on the experimental diffraction data to generate electron density maps of the structure. The map chosen to represent the structure being determined by corroborative chemical and physical data.

Both the Fourier synthesis method and the model approach used to derive the structure of a particular liquid phase have their drawbacks. The Fourier synthesis method experiences difficulty in selecting the correct phase model, and supporting chemical and physical evidence is required before a structure may be proposed. With the model approach, only a limited range of model scattering units have been considered, and little detailed information is available concerning the effects of packing on the various arrays of model cylinders' diffraction patterns.

CHAPTER 3

MODEL PARAMETERS - THE ELECTRON DENSITY DISTRIBUTION

### 3.1 INTRODUCTION

In concept, the diffraction model that is now to be described, and later used to examine the scattering behaviour of various arrays of cylinders, may be regarded as a function of three variable parameters or arguments.

$$\text{Diffraction pattern} = f(ED, L, S) \quad - (1)$$

The components of equation (1) will now be discussed in outline, so that an overview of the model may be gained, and in more detail later on when specific questions need to be answered.

First the electron density distribution (ED) of the cylinder, which bears a (1:1) relation to the distribution of matter within the cylinder, and determines its scattering behaviour. Second, the lattice interference function (L), which describes how the scattered waves interfere due to the spatial arrangement of the array of cylinders. Third, the swelling factor (S), which governs the spatial separation of the cylinders within the array. Since the lattice function and the swelling factor are inter-related, due to the fact that each, in its own way, describes one aspect of the cylinders' distribution in space, the conceptual equation (1) might be more properly written

$$\text{Diffraction pattern} = f(ED, L(S)) \quad - (2)$$

The behaviour of the diffraction pattern, as will be shown later, is due to the subtle interplay of the effects produced by often seemingly slight variations in the model's parameters. In order to understand the underlying diffraction mechanism, each of the above parameters and its variations will be examined in turn.

Once the individual behaviour of each of these parameters has been established, an analysis of the mechanism behind the complete diffraction model will be attempted.

### 3.2 THE ELECTRON DENSITY DISTRIBUTION OF THE CYLINDER

The central concept of the diffraction model used in this thesis is that the electron density distribution (ED) of the cylinder or motif may be represented by an electron density strip model. Before this is discussed in detail, it seems appropriate to briefly consider why the ED is so important a concept to the model's scattering mechanism.

The electric field  $\underline{E}$  of an E-M <sup>wave</sup> acts upon the electric charge  $q$  of a particle producing a force  $\underline{F}$  defined by:

$$\underline{F} = q \underline{E} \quad - (3)$$

This force  $\underline{F}$  causes the particle, mass  $m$ , to experience an acceleration  $\underline{a}$ , governed by the relation

$$\underline{F} = m \underline{a} \quad - (4)$$

combining (3) and (4)

$$\underline{a} = (q/m) \underline{E} \quad - (5)$$

Classical E-M theory states that any charged particle in a state of oscillation will emit E-M waves, of intensity proportional to the (acceleration)<sup>2</sup> of the particle

$$I \times (\underline{a})^2 = (q/m)^2 (\underline{E})^2 \quad - (6)$$

From equation (6), it can be seen that the intensity of the radiation scattered by a particle is inversely proportional to the square of its mass. Since  $(m_e/m_p)$  is approximately 2000, electrons will scatter E-M radiation of the order of  $4 \times 10^6$  times more effectively than protons, and must therefore be regarded as the primary scatterers of E-M radiation.

#### 3.2.1 The Electron Density Strip Model

An electron density strip model is simply obtained by dividing the model cylinder into a series of concentric shells, each with a discrete electron density ( $P_e$ ). By allowing the number of shells ( $N$ ) to increase indefinitely, the discrete electron density distribution tends towards a continuously varying function of the cylinder's radius ( $R$ ).

The scattering function of a structured cylinder with a finite number (N) of shells (or its equivalent electron density strip model, with a finite number of strips) will now be developed, by considering the cases of the solid cylinder and the thin shell and then generalising the theory to cover the N shell case.

### 3.2.1.1 Scattering from an isolated solid cylinder

If the cylinder is long c.f. the wavelength of the X-rays used then the scattering due to a thin slice of the cylinder may be taken to be representative of that due to the whole rod. Thus reducing a complex 3-D problem to a relatively simpler one in 2-D.

Any point within the cylinder may be expressed in cylindrical polar co-ordinates  $(r, \theta, z)$ . However, since only a thin slice of the cylinder need be considered, the  $z$  co-ordinate is a constant.

$$\therefore (r, \theta, z) \rightarrow (r, \theta)$$

In 3-D space,  $\underline{r}$  describes the position of a point wrt an arbitrary origin  $O$ ,  $\underline{dr}$  may be taken to define an element of volume  $dV$ . In 2-D space,  $\underline{dr}$  defines an element of area  $dA$ .

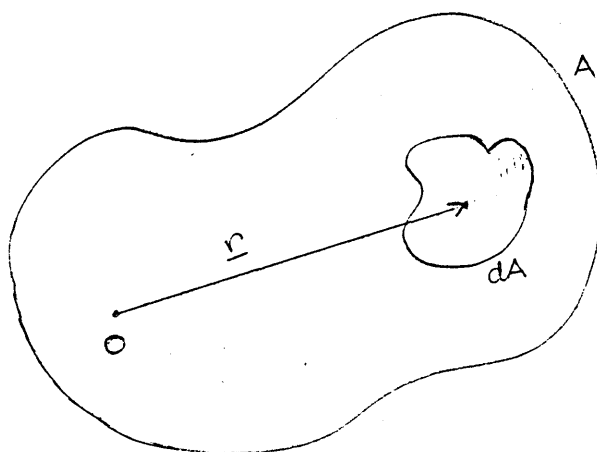


Figure 18

Consider an incident wave  $\psi = \psi_0 \exp(i \underline{k} \cdot \underline{r})$ , if  $\psi_0$  is taken to be 1, then:—  $\psi = \exp(i \underline{k} \cdot \underline{r})$

A 2-D object may be thought of as  $\int d\underline{r}$ , the scattering effect of the obstacle will then be the sum of the individual scattering effects due to each  $d\underline{r}$ .

If  $f(\underline{r})$  defines an amplitude function for the obstacle, then  $f(\underline{r})d\underline{r}$  represents the scattering effect of each element of area  $dA$ .

If  $dS$  represents the scattering by an element of area  $dA$ , then

$$dS = f(\underline{r})d\underline{r}\exp(i \underline{k} \cdot \underline{r})$$

or  $dS = f(\underline{r})\exp(i \underline{k} \cdot \underline{r}) d\underline{r}$

so that  $S = \int_{\text{Obstacle}} f(\underline{r}) \exp(i \underline{k} \cdot \underline{r}) d\underline{r} - (7)$

This is generally written as :

$$F(\underline{k}) = \int_{\text{all } \underline{r}} f(\underline{r})\exp(i \underline{k} \cdot \underline{r}) d\underline{r} - (8)$$

since the  $\int$  is a function of  $\underline{k}$ , the wave vector.

Consider a slice through the cylinder

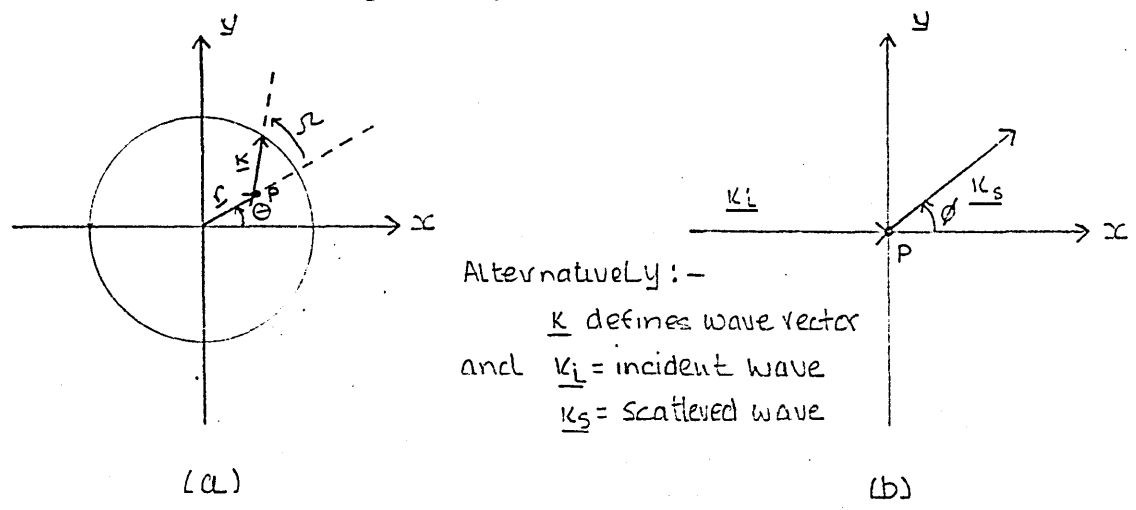


Figure 19

Let  $|\underline{k}| = k$   
 and  $k_x = k \cos \phi$   
 $k_y = k \sin \phi$  - (9)

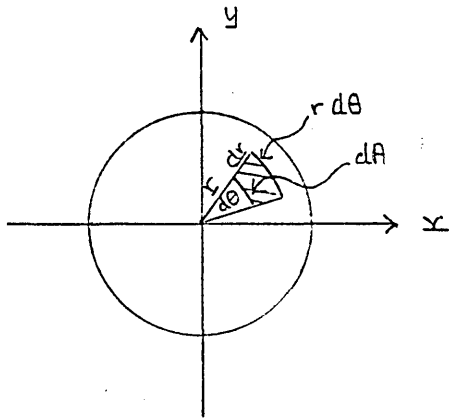
similarly  $r_x = r \cos \theta$   
 $r_y = r \sin \theta$  - (10)

The dot product  $\underline{k} \cdot \underline{r}$  may be written as  
 $\underline{k} \cdot \underline{r} = k_x r_x + k_y r_y$  - (11)

So that using (10) and (8)  
 $F(k) = \int_{\text{all } \underline{r}} f(\underline{r}) \exp(i(k_x r_x + k_y r_y)) d\underline{r}$  - (12)

where  $d\underline{r} = dA$

Due to the fact that cylindrical symmetry exists, equations may be written in terms of polar co-ordinates, so that the results may later be more conveniently expressed in terms of the Bessel functions,  $J_0$  and  $J_1$ .



$dA = r dr d\theta$

Figure 20

From Figure 20 it may be seen that

$dA = r dr d\theta$  - (13)

hence substituting (9), (10), (11) and (13) into (12) gives:-

$F(k) = \int_{\text{all } A} f(r) \exp(i(k \cos \phi r \cos \theta + k \sin \phi r \sin \theta)) r dr d\theta$  - (14)

Here the  $\int$  is over two variables,  $r$  and  $\theta$ , so that

$$F(k) = \int_{r=0}^{\infty} \int_{\theta=0}^{2\pi} f(r) \exp(i(k\cos\phi r \cos\theta + k\sin\phi r \sin\theta)) r dr d\theta \quad - (15)$$

(15) may be re-written as:

$$F(k) = \int_0^{\infty} \int_0^{2\pi} f(r) \exp(ikr (\cos\phi \cos\theta + \sin\phi \sin\theta)) r dr d\theta \quad - (16)$$

But  $(\cos\phi \cos\theta + \sin\phi \sin\theta) = \cos(\phi - \theta)$

writing  $(\phi - \theta) = \mathcal{N}$  so that  $\cos(\phi - \theta) = \cos \mathcal{N}$

$$\text{and} \quad d\theta = d\mathcal{N}$$

Integration limits for  $\mathcal{N}$  are  $0 \rightarrow 2\pi$

$$\text{Re-writing (16)} \quad F(k) = \int_0^{\infty} \int_0^{2\pi} f(r) \exp(ikr \cos\mathcal{N}) r dr d\theta \quad - (17)$$

$$\text{casting (17) into the form} \quad F(k) = \int_0^{\infty} f(r) r dr \int_0^{2\pi} \exp(ikr \cos\mathcal{N}) d\mathcal{N} \quad - (18)$$

and integrating wrt  $\mathcal{N}$  gives

$$F(k) = \int_0^{\infty} r f(r) 2\pi J_0(kr) dr \quad - (19)$$

It is convenient to introduce a "normalising factor" at this point. The amplitude of the scattered wave is governed by  $f(r)$  and the maximum value of the scattered wave is given by  $\int_{\underline{r}} f(\underline{r}) d\underline{r}$ , since  $\exp(ikr)$  has a maximum value of  $\pm 1$ .

Returning to equation (8), and dividing by  $\int_{\underline{r}} f(\underline{r}) d\underline{r}$ , then a relative scattering factor  $F_{\text{rel}}(k)$  may be defined as:

$$F_{\text{rel}}(k) = \frac{\int_{\underline{r}} f(\underline{r}) \exp(ikr) d\underline{r}}{\int_{\underline{r}} f(\underline{r}) d\underline{r}} \quad - (20)$$

writing  $\int_{\underline{r}} f(\underline{r}) d\underline{r}$  in terms of  $(r, \theta)$

$$\int_{\underline{r}} f(\underline{r}) d\underline{r} = \int_0^{\infty} \int_0^{2\pi} f(r) r dr d\theta \quad - (21)$$

$$= \int_0^{\infty} 2\pi r f(r) dr \quad - (22)$$

and dividing (19) by (22)

$$F_{\text{rel}}(k) = \frac{\int_0^{\infty} 2\pi r f(r) J_0(kr) dr}{\int_0^{\infty} 2\pi r f(r) dr} \quad - (23)$$

$f(r)$  cannot exist outside the obstacle, and within the obstacle can have a maximum value of 1.

$$\begin{aligned} \text{i.e. } f(r) &= 1 \text{ for } 0 < r < R \\ &= 0 \text{ for } r > R \end{aligned}$$

so that equation (23) may be written

$$F_{\text{rel}}(k) = \frac{\int_0^{\infty} 2\pi r(1)J_0(kr)dr}{\int_0^{\infty} 2\pi r(1)dr} \quad - (24)$$

$$\text{Now } \int_0^R rJ_0(kr)dr = (R/k)J_1(kR) \quad - (25)$$

so substituting in (24)

$$\begin{aligned} F_{\text{rel}}(k) &= \frac{2\pi(R/k)J_1(k/R)}{2\pi(R^2/2)} \\ &= \frac{2J_1(kR)}{(kR)} \end{aligned} \quad - (26)$$

this then is the scattering amplitude due to a solid cylinder.

### 3.2.1.2 Scattering from an Isolated Cylindrical Shell

Consider now a cylindrical shell, of thickness  $(1 - C)R$ , where  $1 > C > 0$ . The amplitude function only exists within the confines of the shell walls, so that:

$$\begin{aligned} f(r) &= 0 && CR > r > 0 \\ &= 1 && R > r > CR \\ &= 0 && r > R \end{aligned}$$

$$\text{Equation (23) gives } F_{\text{rel}}(k) = \frac{\int_{CR}^R 2\pi r(1)J_1(kr)dr}{\int_{CR}^R 2\pi r(1)dr}$$

$$\text{or } F_{\text{rel}}(k) = \frac{2\pi r(R/k)J_1(kR) - 2\pi(CR/k)J_1(CkR)}{2\pi(R^2/2) - 2\pi(CR^2/2)} \quad - (27)$$

$$F_{\text{rel}}(k) = 2 \left[ \frac{RJ_1(kR) - CRJ_1(CkR)}{k(1 - C^2)R^2} \right] \quad - (28)$$

so that multiplying top and bottom by  $k$

$$F(k) = 2 \left[ \frac{(kR)J_1(kR) - (CkR)J_1(CkR)}{(kR)^2(1 - C^2)} \right] \quad - (29)$$

This represents the scattering amplitude for a thick cylindrical shell.

As the walls of the shell decrease in thickness, so the "thickness factor"  $C$  increases.

Consider equation (22), with  $c \rightarrow 1$ , and for convenience write

$$kr = \alpha$$

$$\text{so that } F_{\text{rel}}(k) = 2 \left[ \frac{\alpha J_1(\alpha) - c\alpha J_1(c\alpha)}{\alpha(1-c^2)} \right] - (30)$$

Expanding  $J_1(\alpha)$  as a series:

$$J_1(\alpha) = \frac{\alpha}{2} - \frac{\alpha^3}{2^3 1! 2!} + \frac{\alpha^5}{2^5 2! 3!} - \frac{\alpha^7}{2^7 3! 4!} + \dots \quad (31)$$

and

$$c\alpha J_1(c\alpha) = \frac{c^2 \alpha^2}{2} - \frac{c^4 \alpha^4}{2^3 1! 2!} + \frac{c^6 \alpha^6}{2^5 2! 3!} - \frac{c^8 \alpha^8}{2^7 3! 4!} + \dots$$

Substituting (31) into (30) gives

$$F_{\text{rel}}(k) = 2 \left[ \frac{1 - \frac{\alpha^2(1+c^2)}{2^3 1! 2!} + \frac{\alpha^4(1+c^2+c^4)}{2^5 2! 3!} - \frac{\alpha^6(1+c^2+c^4+c^6)}{2^7 3! 4!} + \dots \right]$$

$$\text{As } c \rightarrow 1 \text{ then } F_{\text{rel}}(k) \rightarrow 1 - \frac{\alpha^2}{2^2(1!)} + \frac{\alpha^4}{2^4(2!)^2} - \frac{\alpha^6}{2^6(3!)^2} + \dots$$

so that in the limit, for an infinitely thin cylindrical shell, the scattered amplitude is given by:

$$F_{\text{rel}}(k) = J_0(kR) \quad (32)$$

These results were obtained by Oster and Riley<sup>(13)</sup> in 1952.

### 3.2.1.3 Scattering from a Structured Cylinder with N Shells

The solution of  $F(kR)$  for a cylindrical shell is obtained by making the assumption that  $f(r)$  is constant ( $= 1$ ) within the shell walls, the various thicknesses of shell wall being obtained by allowing  $C$  to vary.

$F(kR)$  for a cylinder consisting of series of concentric shells may be obtained by splitting the integration range ( $R \rightarrow 0$ ) in equation (23), into several sections, and summing the separate integrals due to each of these sections.

Equation (23) states:

$$F_{\text{rel}}(kR) = \frac{\int_0^R 2\pi r f(r) J_0(kr) dr}{\int_0^R 2\pi r f(r) dr} \quad - (23)$$

Dividing R according to the number of shells (N) defined by the model, and letting f(r) take the appropriate values for the electron densities of each individual shell, then:

$$F_{\text{rel}}(kR) = \frac{\int_{C_{N-1}R}^R 2\pi r \alpha J_0(kr) dr + \int_{C_{N-2}R}^{C_{N-1}R} 2\pi r \beta J_0(kr) dr + \dots + \int_0^{C_1R} 2\pi r \gamma J_0(kr) dr}{\int_{C_{N-1}R}^R 2\pi r \alpha dr + \int_{C_{N-2}R}^{C_{N-1}R} 2\pi r \beta dr + \dots + \int_0^{C_1R} 2\pi r \gamma dr} \quad - (33)$$

where  $\alpha, \beta, \dots$  etc are the electron density values for the Nth (N-1)th...etc shells.

Solving equation (33), the scattering amplitude due to a structured cylinder with N shells is given by

$$F_{\text{rel}}(kR) = \frac{2 [\alpha(kR) J_1(kR) + (\beta - \alpha) (C_{N-1}R) J_1(C_{N-1}kR) + \dots + (\gamma - \beta) (C_1R) J_1(C_1kR)]}{(kR)^2 [\alpha + (\beta - \alpha) C_{N-1}^2 + (\gamma - \beta) C_{N-2}^2 + \dots + (\gamma - \beta) C_1^2]} \quad - (34)$$

Each shell of the cylinder (or strip of the electron density profile) is represented by a pair of terms in equation (34). For instance, terms relating to the (N-1)th shell involve the factor  $C_{N-1}$ , and those relating to the innermost shell,  $C_1$ . Since the factor  $C_N$  varies in magnitude from zero to unity, the actual values of  $C_N$  relating to a particular shell are given by  $C_p = p/N$ , for example for a model containing  $N=100$  shells, then

$$C_{N-1} = 0.99 \text{ and } C_1 = 0.01 \text{ etc.}$$

### 3.2.2 The number of strips in the model

The problem of the number of strips to include in order to make the model realistic, is resolved as follows. Since it is the aim of the work only to establish a comparative description of the behaviour of the diffraction pattern, i.e. the prediction of trends that occur as the various parameters are varied, it follows that an infinite number of strips need not be considered. Only a relatively small number of strips ( $\leq 10$ ) need be included.

The process of dividing the cylinder into a series of concentric shells, and obtaining the equivalent electron density strip model is best illustrated pictorially as follows:

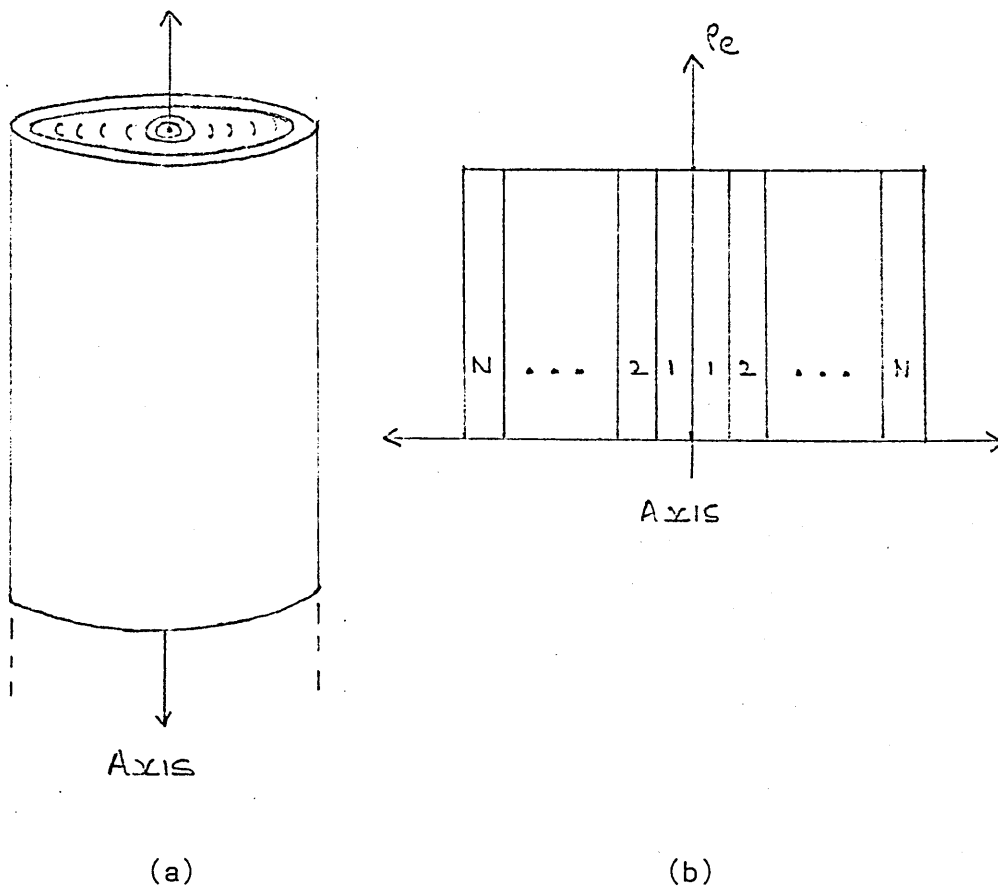


Figure 21

Figure 21 represents the concept of a structured cylinder with N concentric shells (a), and its equivalent electron density strip model (b), which represents the electron density distribution across a thin slice of the cylinder. Note that the shells are divided into equal widths, not equal areas, so that the amount of matter contained within each shell will increase with shell radius, hence each shell's contribution to the total scattering by each cylinder will also vary.

In order to describe and compare the different electron density strip models effectively, some form of shorthand notation is required. The method adopted here will now be described. Examination of Figure 21 (b) shows that the diagram is symmetrical about the  $P_e$  axis (due to the radial symmetry of the cylinder), so that only one half (say the left) is needed to describe any particular strip model or cylinder.

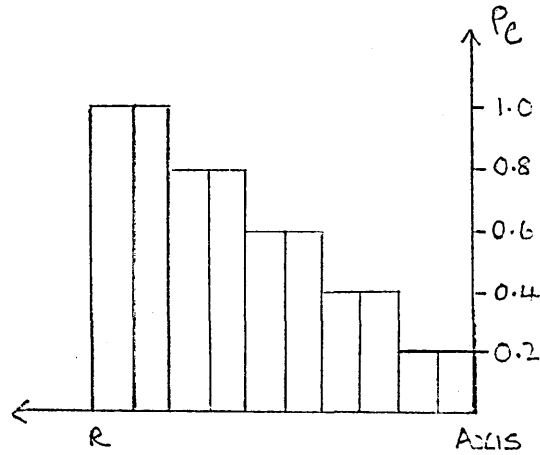
As it is only the relative electron density distribution of the cylinder that is important in determining the scattering envelope, a normalised form of the electron density strip model will be used. That is to say, the maximum value of  $P_e$  occurring in any of the strips will be one.

The electron density profile (EDP) of a structured cylinder may now be defined numerically as:

$$\text{EDP} = (\text{DDDDDDDDDD})$$

where each digit (D) represents the relative electron density of each strip, when read from left to right (ie from the outer to the inner shell).

For example:—



EDP = (1188664422)

Figure 22

Figure 22 represents a structured cylinder with 5 levels of  $P_e$ . Note that decimal points are omitted from the numeric representation and to avoid confusion between unity and 0.1 densities, the former carries an underscore.

### 3.2.3 Model cylinders and their Scattering Profiles

Before considering the scattered intensity profiles (SIP) which are produced by various model cylinders, it is worthwhile to consider how such a profile from a particular cylinder varies according to the number of strips included in the EDP. To illustrate this, a "sawtooth" electron density profile will be used, and several approximations, each with a different number of strips, will be presented.

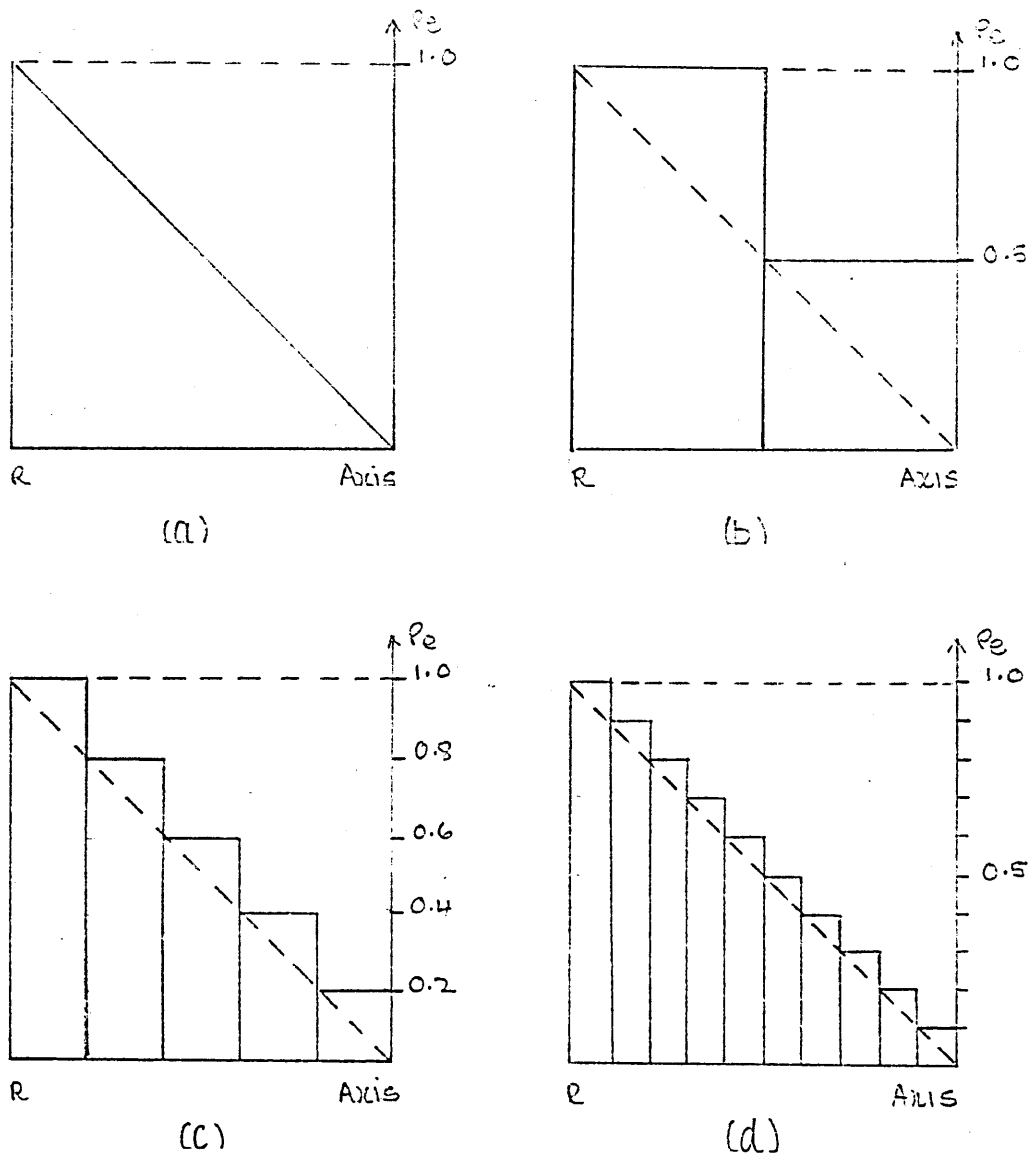


Figure 23

Figures 23 (b)-(d) represent the successive approximations to the "sawtooth" profile shown in (a). The SIP produced by each of these approximations consists of a central main peak, and a single subsidiary peak (as shown in diagram 1). In order to illustrate the variation in SIP of each approximation, the changes occurring in this subsidiary peak, as the number of strips included in the model is varied, are plotted in diagram 1d.

In the case of the two stage approximation, a peak height of  $I \sim 0.043$  (intensity units) is observed at a  $kR$  value of  $\sim 5.0$ . As can be seen the values of  $I$  for the 5 and 10 stage models are 0.050, 0.053 at  $kR$  values of 4.9, 4.8 respectively are observed.

As can be seen from Figure 23 all the approximations employ, to a greater or lesser extent, an overestimate of the area of the original sawtooth electron density distribution, the estimate of this area improving with the number of strips included in the model. The tightening spread of the SIP for the 2, 5 and 10 strip models seems to indicate that a limiting curve is being approached, thus lending support to the choice of a 10 strip model as sufficient to describe an electron density profile.

### 3.3

#### 3.3.1 Scattering profiles due to a series of Cylindrical Shells of various thicknesses

In order to illustrate the change in the model's SIP, as the transition from a solid cylinder to a thin shell occurs, the following series of cylinders is used: (1111111111) to (1000000000) with an electron density decrement ( $\Delta P_e$ ) of (-1) per strip. Each of these cylinders, together with its SIP is illustrated in diagram 2, and plotted as the normalised intensity of scattering vs  $kR$ .

The following points of interest may be noted from the diagrams. The solid cylinder (diagram 2a) has only a single main peak of half width  $3.2kR$ , and a subsidiary peak positioned at  $5.3kR$  and of intensity 0.01. No other peaks are observed, at the level of resolution of intensity used. As the thickness of the shell decreases (more zeros appear from right to left in the EDP), a number of subsidiary peaks appear and increase in intensity.

With the 80% thick shell (diagram 2b), the subsidiary peak has increased in intensity to 0.03, and its position has shifted slightly to a kR value of 5.2. No other peaks are observed. As the shell's thickness decreases further, to 60%, a more pronounced change in the intensity of the subsidiary peak occurs. A maximum value of  $I=0.07$  is recorded at a kR value of 5.0. Again, no other peaks are recorded.

At a thickness of 40%, the position of the subsidiary peak has moved to  $kR=4.7$  and has an intensity of 0.12. An additional peak occurs at a kR value of 8.5, of intensity 0.03.

The 20% thick shell exhibits 4 subsidiary peaks over the range shown (0-20kR). The first and largest of these subsidiary peaks has an intensity of 0.15, and is positioned at a kR value 4.2. The second subsidiary peak both in position and magnitude has an intensity of 0.07, and is situated at  $kR=7.7$ . The other peaks diminish progressively in amplitude as kR increases.

The SIP of an infinitely thin cylinder forms one of the limiting cases for the scattering function (the other being the solid cylinder). Any other type of cylinder or its equivalent EDP must therefore give rise to an SIP intermediate between the 2 limiting cases described above.

The SIP of an infinitely thin shell is described by the function  $[J_0(kR)]^2$ . This function will therefore provide the limiting case, both in terms of the observed or predicted intensities, and also in terms of the positions that are occupied by the subsidiary peaks.

Variations in the magnitude and positions of the subsidiary peaks (diagram 2) bring to the fore, several important points. As the shell's thickness changes from 100% to 80%, there is only a relatively small change in intensity from 0.02 to 0.03, in the first (and only) subsidiary peak. The difference between the 80% thick case and the 60% case is  $(0.07-0.03)=0.04$ , as opposed to the 0.01 difference in intensity between the 100% and 80% thick shells.

From the 60% to the 40% thick shells, a difference of  $(0.12-0.07)=0.05$  is observed, but from the 40% to the 20% case, a difference in intensity between the first subsidiary peaks of  $(0.15-0.12)=0.03$  is observed.

The only case where a substantial second order subsidiary peak is observed, at least at the resolution used for plotting, are the 20% and the 40% thick shells. It will be noted that there is a greater change in peak height or intensity for this second order difference (0.04) than the corresponding change between first order peaks (0.03), for these two cases.

As already indicated, accompanying the change in magnitude of the subsidiary peaks there is also a shift in the positions of these peaks. For the first order peaks, positional shifts from a  $kR$  value of 5.3 for the SIP due to a solid cylinder, to a  $kR$  value of 4.2 due to the 20% thick cylindrical shell, are observed.

Again, as with peak intensities, there is a correspondingly greater positional shift in the second order peak's position for the 40% and 20% thick cases, than in the first order positions.

### 3.3.2 Scattering profiles due to a series of cylinders with "sawtooth" electron density profiles

The SIP due to various sawtooth distributions are compared using diagram 1. The first order peak for the two level EDP (diagram 1a) has an intensity of 0.043, and is centred at  $kR=5.0$ . As the number of levels in the EDP change, a slightly different sawtooth profile results, with corresponding changes in peak heights and positions. The positions of the first order peaks occurring are  $kR=4.9$  for the 5 stage, and  $kR=4.8$  for the 10 stage model. Corresponding intensities being 0.050 and 0.053 respectively. Only small variations in the intensities of the first order peaks are observed, a range of 0.01, compared to the corresponding variation in intensity (0.14) for the first order peaks of the rectangular EDPs illustrated in diagram 2.

### 3.3.3 Scattering profiles due to a series of cylinders with two stage electron density profiles

Diagram 3 shows the effect of reducing the electron density of the inner portion of the cylinder, effectively creating a 2 level electron density distribution. The maximum intensities for the first order subsidiary peaks for the three models are 0.025, 0.045 and 0.070 for the models defined as (a), (b), (c), and their respective positions at  $kR$  values of 5.1, 5.0 and 4.9. A "smooth" variation in peak intensity is to be expected due to there being only a reduction in electron density in one region of the cylinder. The limits of this sequence must be on the one hand the SIP of the solid cylinder, and on the other hand, the shell of 50% thickness, with the equivalent electron density values.

Diagram 4 illustrates the SIPs due to a "standard" sawtooth electron density distribution, and its corresponding mirror image distribution. As can be seen, this reverse distribution behaves in a different manner to the "standard" distribution. The "standard" SIP has a main peak of half width  $3.2kR$ , and the first order peak has intensity 0.053, at a  $kR$  value 4.8. The reverse distribution has no subsidiary peaks whatsoever, and the central or main peak has a half width of  $5.2kR$ .

It is interesting to compare this "reverse" SIP, with that due to the solid cylinder, as shown in diagram 2a. The solid cylinder has a first order peak, the "reversed" cylinder has none. The half width of the central peak due to the solid cylinder is  $3.8kR$ , whereas the "reversed" distributions central peak is  $5.2kR$ , quite the largest by far of all the models illustrated. Discussion of this will be deferred until after the presentation of the next and final set of diffraction profiles.

### 3.3.4 Scattering profiles due to the "moving-shell" series

The effects produced by an EDP in which a pair of shells is separated by increasing distances across the cylinder's radius, whilst one of the shells remains in a fixed position are shown in diagram 5. The basic EDP used is (1100000000), progressing through intermediate stages such as (1000010000) to the limit of the sequence (1000000001).

The SIP due to the 20% thick shell used as the basis for the series is shown in Diagram 5a. The central peak is of half width 2.40kR. As the separation between the shells increases, by increments of 10%R, so the half width of the central peak increases from that of the 20% thick shell, to a value of 2.60kR for the case of the 20% separation between the shells (diagram 5b), up to a value of 2.80 for the 20%R separation. The half width of the central peak remains constant at the value 2.80kR, up to a separation of 60%R between the shells, thereafter decreasing to a value of 2.60kR at 70%R separation, and again decreasing to a value of 2.40kR at the maximum separation of 80%R. The constancy of the central peak's width occurs over the range from 30% to 70%R, measured from the inner to the outer shells, i.e from shells 3 to 7 inclusive.

As the separation of the two shells increases, a shift in position of the first subsidiary peak occurs, from a value of  $kR=4.2$  for the 20% thick shell, to a  $kR$  value of 4.6 for a separation of 20%R between the shells. This position is maintained up to a separation of 30%R, and thereafter the position of the peak is observed to move towards the origin as the shells' separation increases, achieving a position of  $kR=4.1$  at the maximum separation of the first subsidiary peak from the origin ( $kR=4.6$ ) is achieved as the "moving" shell "occupies" shells 6 and 7, as measured from the inner to the outer shell.

Accompanying this change in the position of the first subsidiary peak, there is also a corresponding change in intensity. The 20% thick shell has an intensity of  $I=0.15$  for the first peak, and as the separation between the shells increases there is a corresponding diminution in amplitude, until a minimum value of  $I=0.02$ , at a  $kR$  value of 4.3 is achieved, for a separation of 50%R between the shells. The intensity remains at this level as the separation is increased to 60%R, but as the separation increases still further, to the maximum possible value of 80%R, the intensity starts to increase, until it attains the value  $I=0.10$  at the maximum possible separation. The changes occurring in the values of the intensity and position of the first subsidiary peak follow opposite trends, from minimum to maximum to minimum for the separation from the origin, and from maximum to minimum to maximum for the changes in intensity. The positions of these relative maximum and minimum values of position and intensity do not coincide over all of their respective ranges. The maximum positional movement of  $4.6kR$  away from the origin is constant as the "moving" shell occupies shells 3 to 7, whilst the minimum constant intensity  $I=0.02$  occurs only when shells 6 and 7 are occupied.

Variations in the position and amplitude of the second subsidiary peak are not so well defined as in the case of the first order peak. With certain of the cylinders no second peak is observed at all. For the 20% thick shell, the second peak occurs at a  $kR$  value of 7.8, and is of intensity  $I=0.07$ . At the 10%R level of separation, the position of the second peak has moved to a value of  $kR=8.0$ , and has an intensity of 0.04. As the shell's separation increases to a value between 20% and 40%R, no second peak is observed. At the 50% level of separation between the shells, the second subsidiary peak re-appears, at a position of  $kR=7.1$ , and an intensity  $I=0.03$ . As the separation increases to the maximum possible, the magnitude of the peak increases to a maximum of 0.12, at a  $kR$  value of 7.4, for the 70%R separation, and then decreases to an intensity of  $I=0.10$  at  $kR=7.4$  for the 80%R separation.

Compared to the first subsidiary peak variation, there is a greater relative change in magnitude of the observed intensities in the case of the second subsidiary peak. Also, it will be noted that the variation in intensity of this peak decreases to a minimum value, increases to a maximum and then decreases again, whereas the first subsidiary peak decreases to a single minimum value and then increases again.

Returning again to the 20% thick shell on "base" EDP, over the range shown (0-20 kR), there are additionally third and fourth subsidiary peaks situated at kR values of 11.2 and 14.7, with respective magnitudes  $I=0.04$ , and  $0.02$ . At a separation of 10%R between the shells, the third and fourth peaks are absent. At 20%R, a fifth subsidiary peak appears at  $kR=16.80$  and is of intensity  $I=0.02$ . No second, third and fourth peaks are observed. At a separation of 30%R, the first, fourth and fifth peaks are present and at 40%R, peaks one, three and four may be seen. Subsidiary peaks one, two and three are present at 50%R separation, and again on the 60%R case. An additional fifth subsidiary peak is noted at the 60%R level of separation.

At the 70%R level of separation, five subsidiary peaks may be seen, but in the case of the limiting separation, only the first four peaks are present.

The third subsidiary peaks, when present increase from a value of  $I=0.04$  for the 20% thick shell, to a value of  $I=0.07$  for the 50%R separation, and then decrease to a value of  $I=0.02$  in the 70%R case, but in the limiting 80%R separation case, increases again to a value of  $I=0.03$ .

If a comparison is made of the variation in intensity over the first three subsidiary peaks, the following points are of note. As the shell's separation increases, the intensity of the first peak decreases smoothly to a minimum, and then increases. The second subsidiary peaks intensity variation decreases to a minimum, increases to a maximum, and then decreases again, up to the limit of the shell's separation.

Variation in intensity of the third subsidiary peak takes the form of a function which decreases to a minimum value, then increases to a maximum value, followed by another minimum, and finally increasing again as the limiting separation case is approached.

A further interesting point becomes evident if a comparison is made between the relative peak intensities occurring in the series showing the transition from the solid cylinder (diagram 2) to the thin shell, and the series discussed above. In the former series, each SIP exhibits a gradual fall off in intensity as the peak's positional number increases, but in the latter series, there are several cases where this pattern is not followed. This is clearly demonstrated as the separation of the two shells exceeds the 50%R value, and at this stage, no particular pattern to these variations is evident.

Insufficient numbers of the fourth and fifth subsidiary peaks are present to enable any reliable conclusions to be drawn as to the behaviour of the SIPs, due to the various cylinders, in this region.

### 3.4 ANALYSIS OF THE SCATTERING PROFILES

In order to analyse the governing mechanism that produces the SIP due to a structured cylinder, it is necessary to look in detail at the scattering function, as described earlier. This will now be presented in a slightly simplified form, so that any relevant points may be illustrated more clearly.

The scattering equation (34) for a structured cylinder may be re-written as:

$$F(X) = \frac{2 [P_{10}(X)J_1(X) + (P_9 - P_{10})(0.9X)J_1(0.9X) + \dots + (P_1 - P_2)(0.1X)J_1(0.1X)]}{[(X)^2(P_{10} + (P_9 - P_{10})0.9^2 + \dots + (P_1 - P_2)(0.1)^2]} \quad - (35)$$

the resultant intensity of the scattered radiation is given by

$$I = [F(X)]^2$$

In order to make clear the contribution of each individual shell to the SIP, a slight re-arrangement in the terms of equation (35) is required. So that:

$$F(X) = 2 [P_{10}X(J_1(X) - 0.9J_1(0.9X)) + P_9X(0.9J_1(0.9X) - 0.8J_1(0.8X)) \\ + \dots + P_2X(0.2J_1(0.2X) - 0.1J_1(0.1X)) + P_1X(0.1)J_1(0.1X)]$$

---


$$[X^2(1-0.9^2)P_{10} + (0.9^2-0.8^2)P_9 + \dots + (0.2^2-0.1^2)P_2 + (0.1)^2P_1]$$

- (36)

From equation (36) it may be seen that the cylinder's scattering function is composed of the weighted sum of the differences between pairs of Bessel functions of the first order, which represent the contribution of each shell to the SIP. Each shell's contribution to the total pattern is weighted according to its radial position and relative electron density. This may be represented mathematically as follows:

$$\Delta_N^F(X) = \frac{P_N(X) [(N/10X) - (N-1/10) J_1(N-1/10X)]}{X^2(NF)}$$

- (37)

where  $\Delta_N^F(X)$  is the contribution of the Nth shell to the scattering amplitude

$P_N$  = relative electron density of the shell

$N$  = the shell number (1 for inner shell, 10 for the outer)

$NF$  = the "normalising factor" which is a function of the electron density distribution as a whole.

The two weighting parameters (electron density and shell position or number) introduce the necessary variation into the  $\Delta_N$  sub-function in order for the diffraction pattern to occur at all, otherwise the paired Bessel functions, of the types shown in equation (37); would simply cancel each other out. Although only two basic parameters are present (apart from X), variation in  $\Delta_N$ , is controlled by three factors.

First, it is the shell's position that controls the relative rates of variation of the pair of Bessel functions that combine to produce  $\Delta_N$ , and the rates of variation of these two functions are in the ratio  $N:(N-1)$ , the function involving the factor  $(N-1)$  varying the slowest rate of the two.

Second, it is again the position of the shell that is responsible for the relative proportion or ratio of the two Bessel functions included in  $\Delta_N$ , but third, it is the relative electron density that "weights" the contribution of each individual shell to the total scattering equation.

The normalising factor (NF) that is used to force the SIP to take a maximum value of unity (at the origin), may be seen to represent the total number of electrons that form the relevant EDP.

The following diagram serves to illustrate the complex manner in which the pairs of Bessel functions that compose the various  $\Delta_N$  sub-functions behave.

Figure 24 shows 3 pairs of related Bessel functions that might typically make up the  $\Delta_N$  sub-functions of the scattering equation. The resultant composite (or difference) function of the pairs of Bessel functions are shown as the dashed lines on their respective diagrams.

The form of this composite function, may be seen by inspection to depend on the relative rates of variation of the component Bessel functions. Figure 24a shows  $J_1(X)$  and  $J_1(0.9X)$ . The rate of variation (R) of the two functions is given by  $(X/0.9X) \sim 1.1$ . The composite curve is seen to oscillate periodically about the (X) axis, the position of its zeros being determined by the places where the two Bessel functions intersect each other.

Figure 24 shows the pair of Bessel functions  $J_1(0.5X)$  and  $J_1(0.4X)$  together with their derived composite function. The R value of the two functions is  $\sim 1.3$ , which means that the two Bessel functions will be even more out of phase, compared to those in Figure 24a this is reflected by the fact that the position of the zeros of the composite function have changed, as have the values of the relative maxima and minima, compared to the composite function shown in Figure 24a.

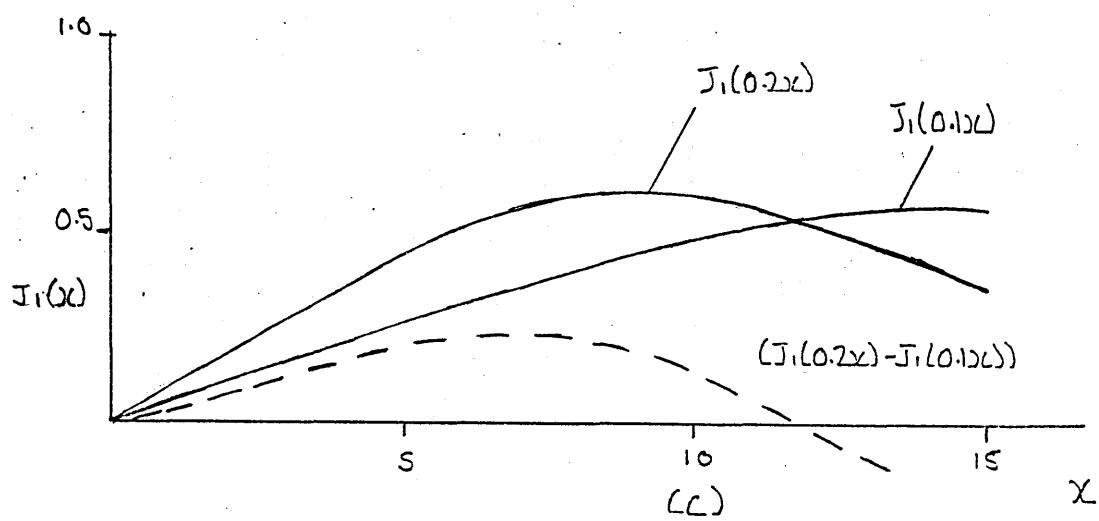
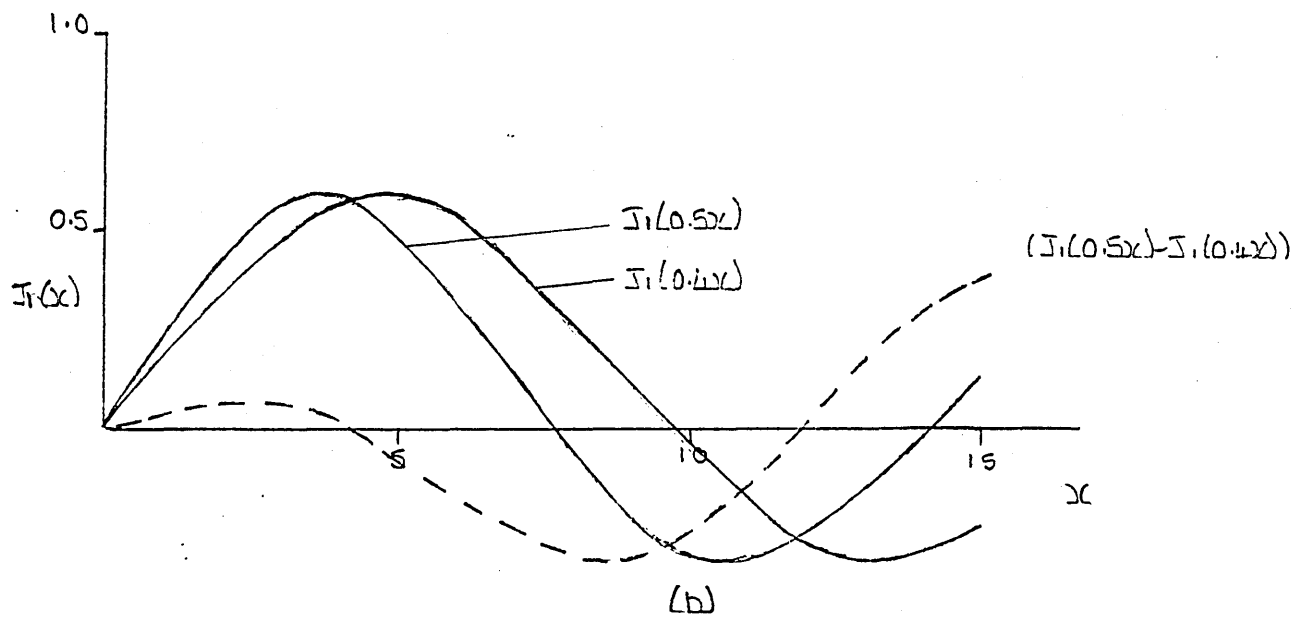
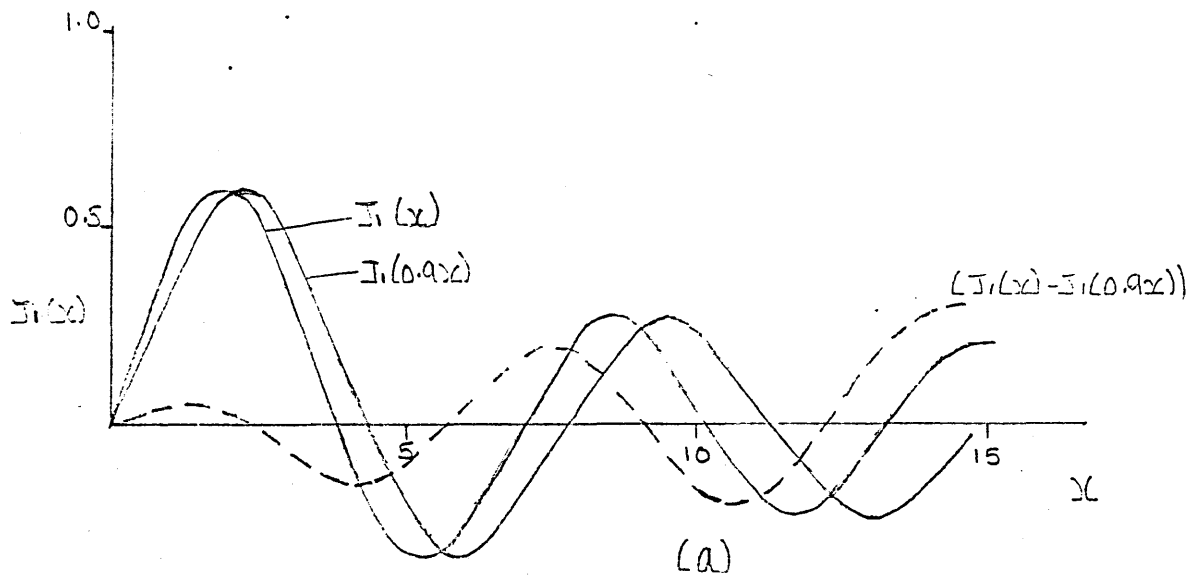


Figure 24

Figure 24c shows the pair of functions  $J_1(0.2X)$  and  $J_1(0.1X)$  the former function varying at twice the rate of the latter ( $R=2.0$ ). The composite function has changed considerably (over the ranges shown), compared to cases (a) and (b).

With reference to Figure 224 a,b,c and equation (37) it may be seen that the three pairs of Bessel functions chosen are those that appear in the  $\Delta_N$  sub-functions corresponding to the outer and inner-most shells (Figure 24a, c) and the fifth shell (Figure 24b) of the model cylinder.

The effect of changing the shell's number or equivalently its position, on the composite function on moving from the outer to the inner shells is to magnify or "exaggerate" the "basic" composite function shown in Figure 24a. Composite curves (Figure 24a and c) are in the main similar in form or shape, except in the position of their corresponding zero values and magnitudes.

This is to be expected, since the rates of variation of the two pairs of Bessel functions are almost the same, (1.1 and 1.25).

A more pronounced change in the composite function shown in Figure 24c is expected since the rate of variation of the paired Bessel functions is almost twice the rates in the other two cases.

The range of values of  $X$  chosen for Figure 24 a,b,c corresponds approximately to the range of values used to plot the SIP. Over this range, the composite functions that serve to make up the "core" of the  $\Delta_S$  sub-functions grow progressively more simple as the shell number decreases, but the absolute values or magnitudes of the functions increase. Hence the contribution of each shell to the diffraction pattern should increase as the shell number decreases, if the  $\Delta_N$  function were to be governed purely by composite function alone. This is not the case, due to the second and third controlling factors previously mentioned.

With the second controlling factor in the  $\Delta_N$  sub-function, account is taken of the fact that the actual composite function is made up of the contributions of "weighted" pairs of Bessel functions, which serves to reduce the absolute values of the composite function in relation to its shell number or position.

It is at the level of the third controlling factor where the complete SIP is assembled from the sub-functions,  $\Delta_N$ , due to each individual shell. Each sub-function's contribution to the SIP is weighted according to the electron density value occurring in the particular shell to which it relates.

On the basis of the above discussion, an attempt will now be made to analyse the behaviour of the SIPs due to the various types of structured cylinder outlined earlier.

The "rectangular" series of EDPs due to the solid cylinder/thin shell set of structured cylinders will now be considered, recalling equation (36)

$$F(X) = 2[P_{10}(X)(J_1(X) - 0.9J_1(0.9X)) + P_9(X)(0.9J_1(0.9X) - 0.8J_1(0.8X)) \\ + \dots + P_1(X) 0.1J_1(0.1X)]$$

---

X<sup>2</sup>NF

- (36)

A solid cylinder is defined by the particular case of a structured cylinder with constant electron density throughout ie  $P_{10} = P_9 = \dots = P_1 = 1.0$  which means that all of the ten shells making up the amplitude function  $F(X)$  are equally weighted in their contributions. The normalising factor (NF), both here and throughout, serves merely to adjust the scale of the resultant SIP to a suitable value. The intensity is derived from the square of  $F(X)$ , and this process will serve to highlight certain features of the  $F(X)$  or its derived function  $[F(X)]^2$ .

As the transition from a solid cylinder to a thin shell occurs, the effect upon the scattering function is that the contributions of the certain shells are absent, because the electron density ( $P_e$ ) in these particular regions are zero.

Referring to diagram (2) it will be seen that the effects of reducing the shell's thickness on the various SIPs shown, are in accord with the theory just developed. The transition from a solid cylinder to an 80% thick shell produces only a relatively small difference between the respective SIPs. This corresponds mathematically to the slowest varying composite functions, that carry the least weightings (lowest shell numbers), being omitted from the scattering equation.

The biggest relative changes between SIPs occur when the shell's thickness lies in the 80% to the 40% range, thus indicating that it is the cylinder's mid-radius shells, in the numerical range 3 to 7, or their corresponding  $\Delta_N$  sub-functions that have a major impact upon the structure of the SIPs. This may be explained by reference to Figure 24. Although the composite functions that compose the various  $\Delta_N$  functions tend to increase in absolute value as the shell number decreases, it might be supposed that the  $\Delta_N$  functions due to the low numbered shells (1,2) make the biggest contribution to the SIP. This is not so, due to the fact that the highest value composite functions due to the lowest numbered shells also carry the lowest positional weightings. One parameter's effect opposes the other. Even though the higher number shells carry the largest positional weightings, the relatively small contribution of the relevant composite functions tends to oppose this, effectively lessening the contribution due to the higher numbered shells. It is with the middle order shells that the composite function, or the Bessel functions that form the basis of it are sufficiently well separated that the effect of the positional or shell weighting is overcome, therefore making the middle orders have the biggest impact upon the SIP.

From the 40% to the 20% thick case, and then to the infinitely thin shell, the relative changes between the corresponding SIPs will be less marked due to the fact that a limiting scattering function is being approached.

The variation in SIPs, as noted earlier, is most evident in the first order peak heights and positions, and also in the changes in shape (not magnitude) of the central or main peak.

It is worthy of note at this point that the normalising factor is self-adjusting to the number of shells that are included in the scattering function, due to the fact that electron density factors are present within the (NF) itself.

Diagram (1) shows the SIPs due to the various sawtooth approximations, and illustrates the result of a scattering function that contains the contributions of all ten shells of the cylinder, weighted according to a series of decreasing electron density values (1.0, 0.9, 0.8,....., 0.1) because the three EDPs used are very similar, particularly in the five and ten level cases, no significant changes in the SIPs are to be expected. Comparing the 2 level EDP to the five and ten level cases, it might be expected that a significant difference should occur here.

The differences between the 3 EDPs presented are of relatively small changes in the electron density weighting of the shell's composite functions and these small changes in weighting are not of a sufficient size to alter the shape of the SIPs in a major way.

Again diagram (1), showing the effects of reducing the electron density of the inner five shells, relative to the remainder, illustrates the effects of electron density weighting on the scattering function due to a full set of ten shells. Only as the weightings of the inner five shells approach the value 0.2, does any significant variation in the SIP occur.

The "standard" sawtooth EDP and its mirror image distribution, diagram (4) pose a more interesting test of the theory just outlined. The shape of the reverse distribution may be accounted for in the following way.

The shells that normally contribute the most to the SIP, are the middle to the outer shells, as in the cases of the solid cylinder etc, and the standard sawtooth, where more or less "normal" electron density weightings of the  $\Delta_N$  functions are present. However, in the case of the reverse sawtooth, the weightings used in the scattering function are reversed. This results in the contributions of the middle to outer shells being reduced at the expense of the inner shells with less varying  $\Delta_N$ , which are greatly enhanced, compared to the standard sawtooth. The contributions of the fastest varying functions are diminished as the contributions due to the slowest varying are enhanced.

The net result of this is that the SIP due to the reverse sawtooth has only a single main peak of half width  $5.2kR$ , which is by far the largest central peak width noted of any of the models used.

The importance of the terms due to the mid-radius shells to the scattering profile will now be examined with the aid of the moving shell series of EDPs as presented in diagram (5) and Figure 24 in which a pair of shells are selected, one of which is fixed as the 10th and outer shell and the other being allowed to move in relation to fixed shell. The effect on the scattering equation may be seen as follows:

Re-calling equation (35)

$$F(X) = 2[P_{10}(X)(J_1(X) - 0.9J_1(0.9X)) + P_9(X)(0.9J_1(0.9X) - 0.8J_1(0.8X)) + \dots + P_1(X)(0.1)J_1(0.1X)]$$

---


$$(X)^2 [(1-0.9^2)P_{10} + (0.9^2-0.8^2)P_9 + \dots + 0.1^2P_1] \quad - (35)$$

Since the outer or 10th shell remains fixed in position the term in equation (35) relating to this viz  $[P_{10}(J_1(X)) - 0.9J_1(0.9X)]$  will always be present. The effect of the moving shell on the remaining terms in equation (35) will be to select the terms that relate to the current position of the moveable shell for inclusion in the "reduced" scattering equation, and exclude the rest.

The normalisation factor being treated in similar manner. Equation (36) reduces to:

$$F(X) = 2 \left[ P_{10}(X)(J_1(X) - 0.9J_1(0.9X)) + P_N(X) \left( \frac{N}{10}J_1(NX) - \left( \frac{N-1}{10} \right) \cdot J_1\left(\frac{N-1}{10}X\right) \right) \right]$$


---


$$X^2 \left[ (1-0.9^2)P_{10} + \left( \left( \frac{N}{10} \right)^2 - \left( \frac{N-1}{10} \right)^2 \right) P_N \right]$$

- (37)

where  $N =$  shell number

Since the electron density values for these two shells are taken to be 1.0,  $P_{10} = P_N$  throughout the "moving-shell" series of cylinders. For the two shells in contact the moving shell is number  $N=9$ . Inserting this value on  $N$ , together with the appropriate  $P_e$  values, has the effect of cancelling out the two terms in equation (3) involving the function  $J_1(0.9X)$ , thereby reducing the equation to the variables  $J_1(X)$  and  $J_1(0.8X)$ . Diagram (4a) shows that four subsidiary peaks are observed in the case of the two shells in contact, (1100000000).

Moving on to diagram (4b) the (1010000000) case, equation (38) has become a function of two clear-cut  $\Delta_N$  sub-functions, as opposed to the previous case where the two sub-functions merged into one. The effect of the interaction of two composite functions on the SIP diagram (4b) is the reduction in the number of subsidiary peaks from four in the close contact case, to two with reduced amplitude in the present case.

Diagram (4c) illustrates the (1001000000) case, where the first order peak has been reduced in intensity even further compared to the latter case, and the second subsidiary peak has disappeared. However a fifth subsidiary peak has been introduced

Diagram (4d) has three subsidiary peaks at positions one, four and five, and represents the case where the two shells are separated by three equivalent of three "empty" shells.

At shell separations of between three and five, diagram (4 d,e,f), only three subsidiary peaks are observed of varying orders. The interesting point is that these subsidiary peaks become more closely spaced ie from (1,4,5) to (1,3,4) to (1,2,3) for the three cases.

These latter three cases correspond to the terms in equation (36) that are due to the mid-range shell positions of the structured cylinder. This means that the corresponding composite function involving the two relevant Bessel functions is maximising its contribution in this region.

As the separation increases to the maximum possible (1000000001) the number of subsidiary peaks increases to five, and finally back to four at maximum separation.

The scattering function for the cases approaching maximum separation, is composed of the  $\Delta_N$  sub-function for the outer or tenth shell, combined with, and one of the sub-functions relating to the inner shells. At almost maximum separation the relevant  $\Delta_N$  function is varying at a slow rate (c.f that of the  $\Delta_{10}$  shell), so that here the SIP ought to be composed of the pattern due to the thin shell (of 10% thickness) with slight modification due to the more slowly varying, and low positionally weighted inner shell. Diagram (4d,h,j) apparently confirms this.

As will be noted from the diagrams (2,3,5), the intensities of the subsidiary peaks tend to decrease with peak position number, but with the "moving-shell" series diagram (5), this is not always the case. This is presumably due to the fact that interactions between the sub-functions making up the latter case are not concealed by the contribution of additional shells that are present in cases such as the solid cylinder etc.

CHAPTER 4

MODEL PARAMETERS - THE LATTICE FUNCTION

## 4.1 INTRODUCTION

The concept of the lattice interference function as used by Oster and Riley<sup>(13,15)</sup> and Burge,<sup>(17,18,19)</sup> forms the basis of the model's interference function, the behaviour of which is examined as the number of points in a centred, hexagonal lattice is varied.

As is shown, an infinite lattice need not be considered, since a sufficiently close approximation to the interference effects produced by an infinite lattice is obtained from an array with only a limited number of points.

Starting with a centred hexagonal array consisting of seven points, the resulting behaviour of the interference function is examined as the lattice is expanded by adding extra lattice points. This is accomplished by the process of adding complete concentric "rings" of points to the basic array of seven points.

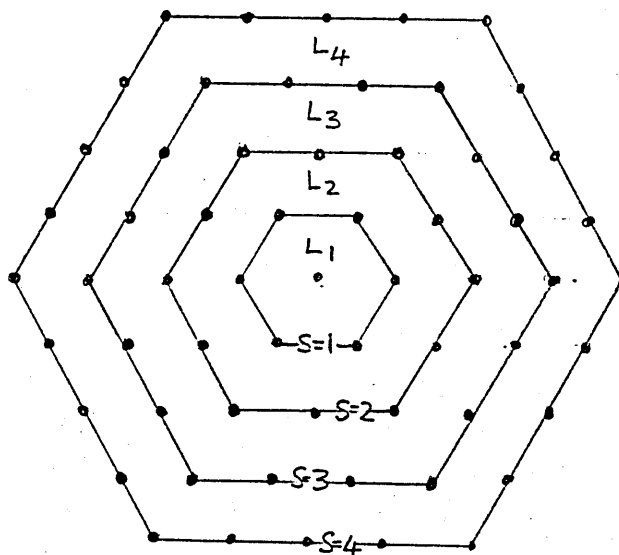


Figure 25

A series of 4 centred blocks of lattice are shown in Figure 25. The block  $L$ , consisting of the central point and ring  $S_1$ ,  $L_2$  consisting of  $(L_1 + S_1)$ ,  $L_3$  consisting of  $(L_2 + S_3)$  etc.

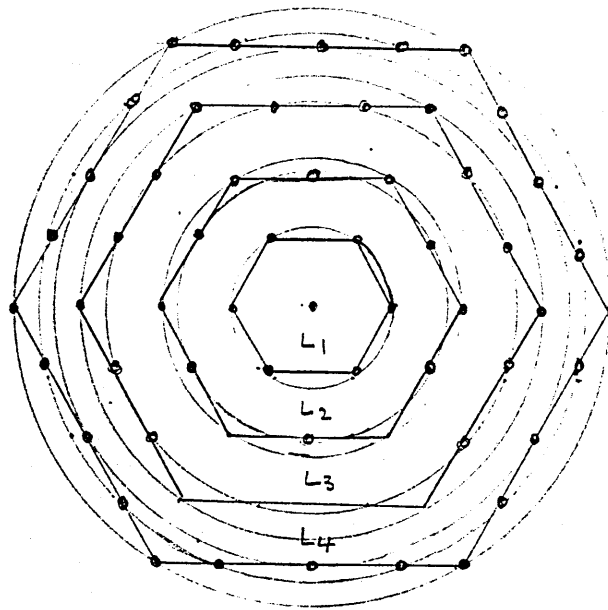


Figure 26

As can be seen from Figure 26, the lattice points for the series of centred lattices  $L_1 - L_4$  fall on a series of concentric circles. The number of circles associated with each hexagonal ring increases as the ring number increases and is given by the relation:

$$\begin{aligned}
 C &= (S + 2)/2 && S \text{ even} \\
 &= (S + 1)/2 && S \text{ odd}
 \end{aligned}
 \quad - (1)$$

For example, if  $S = 2$  then  $(2+2)/2 = 2$  circles are required to describe the second ring, and for  $S = 3$  then  $(3+1)/2 = 2$  circles are required. Inspection of Figure 26 shows that for any odd numbered ring  $S$ , then the  $S_{th}$  and the  $(S + 1)_{th}$  rings are described by the same number of circles.

The radii ( $R_S$ ) of the various circles are related to the ring number ( $S$ ), by the following relation:

$$R_S(K) = [S(S-K) + K^2]^{\frac{1}{2}}R \quad - (2)$$

where  $K = 0, 1, \dots, S$

$R_S(K)$  = radius of a particular circle related to the  $S$ th ring

$R$  = radius of  $S_1$ , the basic array.

As an example, consider the 4th ring of lattice points. The radii of the various circles relating to the 4th ring are obtained from equation (2) by allowing  $K$  to take the values  $0, 1, \dots, S$ , so that  $S = 4$ , the values of  $R_S(K)$  obtained are  $4R, \sqrt{13}R, \sqrt{12}R, \sqrt{13}R, 4R$ . Hence it is seen that only three circles of radius  $4R, \sqrt{13}R, \sqrt{12}R$  are needed to describe the radial symmetry of the fourth ring. Figure 27 illustrates the case for the fourth ring.

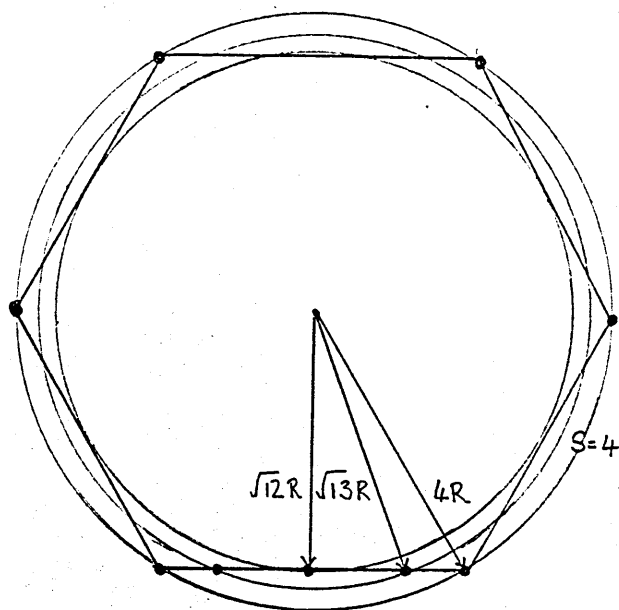


Figure 27

The multiplicities of the values of  $R_S(K)$  occurring for each particular ring are determined by the number of times ( $T$ ) a particular circle cuts a side of the related hexagonal ring. Referring to Figure 29 it can be seen that  $T$  can only take two values, namely  $T=1$  or  $T=2$ .

Figure 27 illustrated a series of concentric lattices, consisting of from one to four complete rings of points. The number of points contained within each of the lattices  $L_1$  to  $L_4$  is given by the following relation:

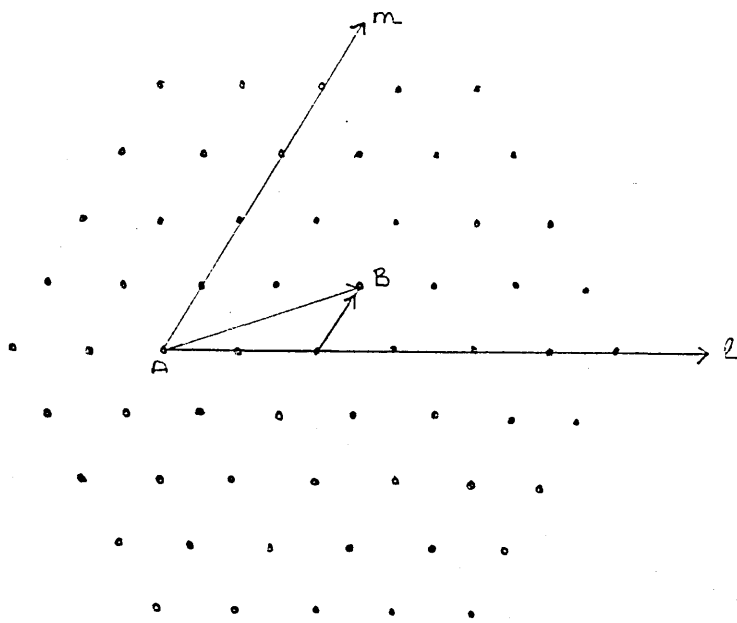
$$N = 3s^2 + 3s + 1 \quad - (3)$$

For example, if the array consists of three concentric rings, then the number of lattice points  $N = (3 \times 3^2 + 3 \times 3 + 1) = 37$  points. Each ring included in a particular array contains  $N = 6S$  lattice points. For instance if the lattice  $L_3$  is expanded to  $L_4$ , then an extra  $N = (6 \times 4) = 24$  lattice points are added, giving a total of 61 lattice points in all. The use of a series of centred lattices in the form described above, enables an orderly transition from the basic lattice configuration ( $L_1$ ) consisting of seven points, through to the lattices  $L_2, L_3, L_4$  with increasing numbers of lattice points, to be made. This enables a detailed examination of the behaviour of the lattice function as the number of points included in the array increases.

#### 4.2 THE LATTICE CO-ORDINATE SYSTEM

At this point, it is convenient to introduce a co-ordinate system that is to be used to describe the relation between the lattice points in a centred hexagonal array. Use will be made of the system in order to describe the phase relationships existing between waves scattered by such centred arrays of model cylinders. Such a system was described by Burge<sup>(17)</sup> and is adopted here.

If a convenient lattice point be taken as the origin of the co-ordinate system, any other lattice point may be referenced by a pair of integers (l,m), which serve to define a lattice vector. This is illustrated as follows:



$$D_{A,B} = (l^2 + lm + m^2)^{1/2}$$

$$l, m \geq 0$$

Figure 28

The length or magnitude  $D_{A,B}$  of the vector AB between the pair of points A, B is given by the following relation:

$$D_{A,B} = (l^2 + lm + m^2)^{1/2} \quad - (4)$$

$$l, m \geq 0$$

for the particular points in question  $l = 2, m = 1$

$$\text{from (44) } D_{A,B} = (2^2 + 2 \cdot 1 + 1^2)^{1/2} = \sqrt{7}$$

For an array containing N lattice points, there are  $N^2$  lattice vectors, not all of different magnitude. For example, an array containing seven lattice points has  $(7^2) = 49$  lattice vectors of various lengths, whilst an array of 4 complete rings (61 lattice points) has 3721 lattice vectors relating the lattice points.

Applying the condition  $l, m = 0$  to equation (4) implies the presence of lattice vectors of zero length. The number of zero length vectors present for any given array is equal to the number of points (N) included in the array.

The number  $V_{1,m}$  of lattice vectors of length  $u$  in any given hexagonal array is determined by the following relation, due to Burge<sup>(17)</sup>

$$V_{1,m} = 12 \sum_{u=0}^{\min(s-m, 2s-l-m)} [2s-l-m+1-u] + 12 \sum_{u=1}^{m-1} [2s-l-m+1] + 12 \sum_{u=\max(m,1)}^s [2s-l-m+1] \quad - (5)$$

The second term in equation (5) is valid for those vectors where  $m-1=0$ . If  $m=0$  or  $1=m$ , the vectors are counted twice, and equation (5) gives  $2 \times V_{1,m}$ .

The multiplicity factor 12 which is due to the symmetry of the hexagonal lattice is not valid for the zero length or identity vectors (0,0), thus equation (5) is only applicable for  $1, m \geq 0$ .

Whilst equation (5) determines the number of vectors of a particular length  $V_{1,m}$ , the total number of  $V_{1,m}$  vectors of different lengths is given by

$$\sum V_{1,m} = (L + 1)^2 \quad - (6)$$

where  $L$  = number of complete rings in the lattice.

The significance of equations (4) and (5) which serve to determine the lengths and numbers respectively of the lattice vectors, is as follows.

Whilst it is the motif or cylinder that is responsible for the scattering of the incident X-radiation, it is the purpose of the lattice function to account for the way that the scattered waves interfere to produce the diffraction pattern, by the introduction of phase differences between the scattered waves.

The number of inter-point vectors defined by the array, including the zero length vectors, determine the number of phase relationships possible between the scattered waves, whilst the length of each vector between a pair of lattice points, determines the difference in phase between the scattered waves.

The number of phase relationships possible for a given lattice, corresponds to the number of lattice vectors present. For example, the hexagonal lattice consisting of four complete rings, has 3721 possible phase relationships between scattered waves, and from equation (6), it can be seen that of these 3721 phase relationships, there are only 25 different magnitudes.

#### 4.3 THE LATTICE INTERFERENCE FUNCTIONS

The mathematical form of the interference function may be defined as follows:

$$I = 1/n^2 \sum_{l=1}^n \sum_{m=1}^n J_0 (kU_{l,m}) \quad - (7)$$

where  $I$  = Normalised magnitude of the interference function

$K = 4 \sin\theta/\lambda$

$\theta$  = Bragg angle

$U_{l,m}$  = separation of the  $l$ th and  $m$ th lattice points

$n$  = number of lattice points

The original form of equation (7) due to Debye (1915)<sup>(14)</sup> is modified here by the inclusion of the factor  $(1/n^2)$ , in order to obtain the interference per lattice point, the significance of this will be apparent when the whole model is discussed.

The variable ( $U$ ) in equation (7) corresponds to the lattice vector defined earlier, the link between the lattice vector and phase being established when the variables  $K$  and  $U$  are considered together.

The radial nature of the lattice used is reflected by the inclusion of the zero order Bessel function  $J_0$  in equation (7).

The interference functions due to the lattices  $L_1$  to  $L_4$  are shown below:

$$I_1 = 1/7^2 [7 + 24J_0(X) + 6J_0(2X) + 12J_0(\sqrt{3}X)] \quad - (8)$$

$$\begin{aligned}
I_2 = & 1/19^2 [ 19 + 84 J_0(X) + 54J_0(2X) + 24J_0(3X) + 6J_0(4X) \\
& + 60J_0(\sqrt{3}X) + 72J_0(\sqrt{7}X) + 24J_0(\sqrt{13}X) \\
& + 18J_0(2\sqrt{3}X)] \quad - (9)
\end{aligned}$$

$$\begin{aligned}
I_3 = & 1/37^2 [37 + 180J_0(X) + 138J_0(2X) + 96J_0(3X) + 54J_0(4X) \\
& + 24J_0(5X) + 6J_0(6X) \\
& + 144J_0(\sqrt{3}X) + 216J_0(\sqrt{7}X) + 144J_0(\sqrt{13}X) + 72J_0(\sqrt{21}X) \\
& + 24J_0(\sqrt{13}X) \\
& + 78J_0(2\sqrt{3}X) + 96J_0(\sqrt{19}X) + 36J_0(2\sqrt{7}X) + 24J_0(3\sqrt{3}X)] \\
& - (10)
\end{aligned}$$

$$\begin{aligned}
I_4 = & 1/61^2 [61 + 312J_0(X) + 258J_0(2X) + 204J_0(3X) + 150J_0(4X) \\
& + 96J_0(5X) + 54J_0(6X) + 24J_0(7X) + 6J_0(8X) \\
& + 264J_0(\sqrt{3}X) + 432J_0(\sqrt{7}X) + 336J_0(\sqrt{13}X) \\
& + 240J_0(\sqrt{21}X) + 144J_0(\sqrt{13}X) + 72J_0(\sqrt{43}X) + 24J_0(\sqrt{57}X) \\
& + 174J_0(2\sqrt{3}X) + 264J_0(\sqrt{19}X) + 180J_0(2\sqrt{7}X) \\
& + 96J_0(\sqrt{39}X) + 36J_0(2\sqrt{13}X) + 96J_0(3\sqrt{3}X) + 120J_0(\sqrt{37}X) \\
& + 48J_0(7X) + 30J_0(4\sqrt{3}X)] \\
& - (11)
\end{aligned}$$

where  $X = kU$

The number of terms present within the brackets is given by  $(L+1)^2$ , hence for  $L = 4$ , there are twenty five terms present inside the brackets.

Diagram (6) shows the form of the four lattice functions  $L_1$  to  $L_4$ . Also shown in the diagrams are the positions of the reflections that would be expected from an infinite hexagonal array. (see Appendix B for the calculation of the reflections for an infinite lattice).

#### 4.3.1 The $I_1$ interference function

In order to gain a deeper insight into the structure of the interference function, it is necessary to consider in detail the component parts of the function.

As a particular case, consider the  $I_1$  interference function describing the interference produced by a centro-symmetric array of seven points.

Re-calling equation (8)

$$I_1 = 1/7^2 [7 + 24J_0(X) + 12J_0(\sqrt{3}X) + 6J_0(2X)] \quad - (8)$$

where  $X = (kU_{1,m})$

As can be seen, the function  $I_1$  is composed of combinations of the function  $J_0$ , weighted according to the numbers of the various lattice vectors of length  $(U_{1,m})$  present in the array. By writing the quantity  $(kU_{1,m})$  as  $(X)$ , it is evident that the  $I_1$  function is composed of a series of weighted combinations of the same function that are varying at different rates. Recall that the scattering function of a structured cylinder is built up in much the same manner as the above, except that the function concerned is  $J_1(X)$  instead of  $J_0(X)$ . For example, the component Bessel functions in equation (8) vary at rates of  $X$ ,  $\sqrt{3}X$  and  $2X$ .

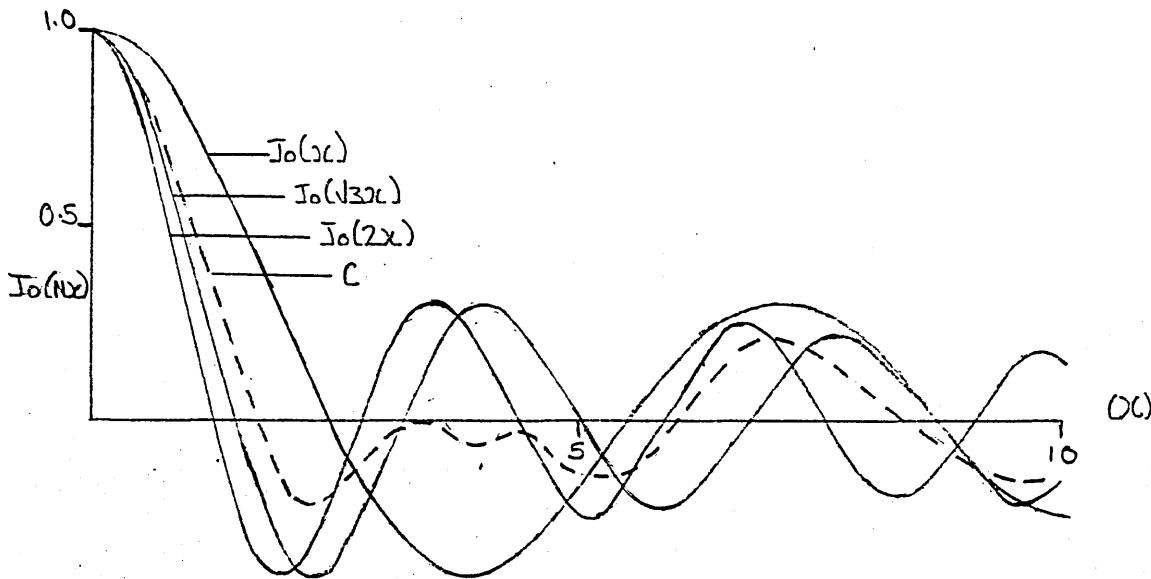


Figure 29

Figure 29 shows the three Bessel functions  $J_0(X)$ ,  $J_0(\sqrt{3}X)$ , and  $J_0(2X)$ , whose rates of variation are in the ratio  $(1:\sqrt{3}:2)$ . As can be seen from equation (8), the functions composing the interference function are not paired, as in the case of the scattering function (see earlier). The composite function  $C$ , derived from the average value of  $J_0(X)$ ,  $J_0(\sqrt{3}X)$  and  $J_0(2X)$  has a central peak of maximum value 1.0 at the origin. As  $X$  increases the function  $C$  takes positive and negative values of diminishing absolute value. The form of the curve  $C$  is due to the fact that the component functions are varying at different rates.

The interference function  $I_1$  is however composed of weighted values of the functions shown in Figure 30, which account for the multiplicities of the phase differences between the waves scattered from pairs of lattice points, plus the zero phase difference waves scattered from the individual lattice points.

Figure 30 shows the components parts of the interference function defined by equation (8).

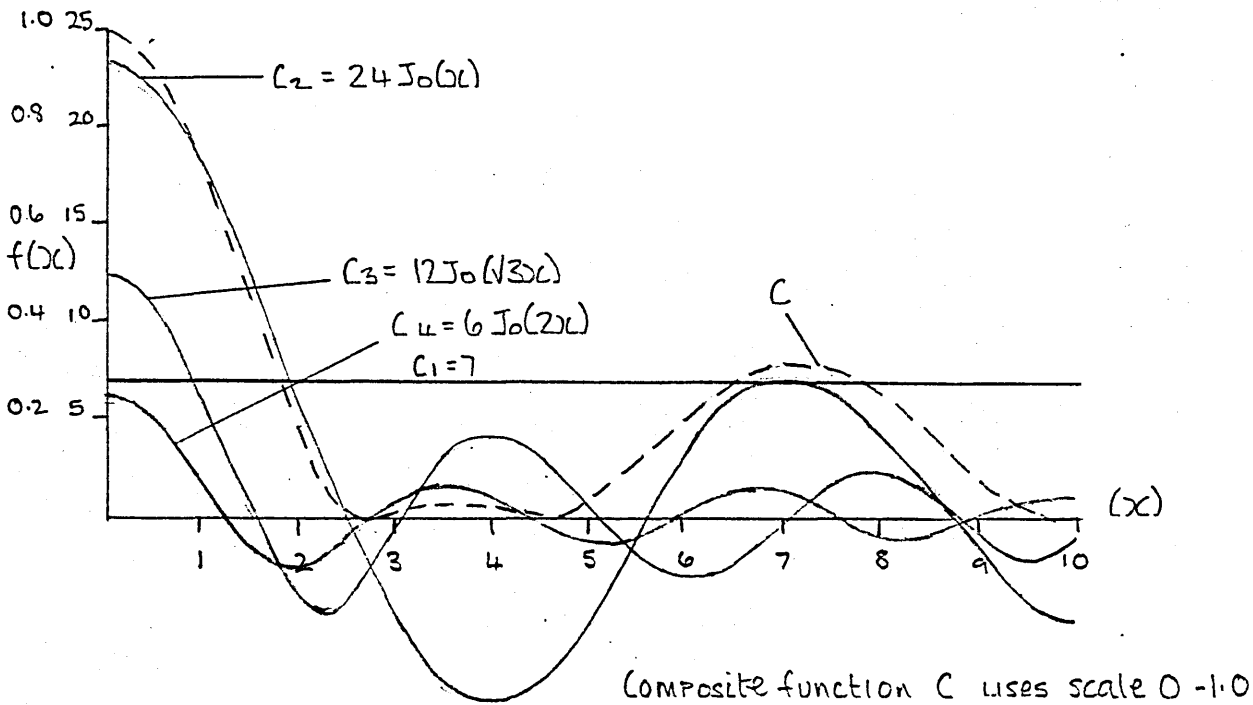


Figure 30

The composite function  $C$  shown in Figure 30 represents the weighted sum of the four functions defined in equation (8). The maximum value of which is 49 at the origin. It will be noted that in contrast to Figure 29 where the three functions are unweighted, the effects of weighting, plus the offset (due to waves scattered from each lattice point), force the composite function to take only positive values. The interference function  $I_1 = C/7^2$ , is in effect, the average contribution of each lattice point to the scattering function.

Several interesting points emerge from inspection of Figure 30 above. Close to the origin, the composite function is dominated by the slowest varying component function viz  $24J_0(X)$ . The region from  $2.4X$  to  $5.6X$  where the function is negative is offset by the two faster varying functions  $12J_0(\sqrt{3}X)$  and  $6J_0(2X)$ , and the constant term, represented by the straight line. In the region near the origin, where the components  $C_3 = 12J_0(\sqrt{3}X)$  and  $C_4 = 6J_0(2X)$ , the width of the central peak is in the main determined by the function  $C_3$  and  $C_4$  which are the fastest varying components in the interference function. Due to the fact that  $C_3$  and  $C_4$  are varying collectively at approximately twice the rate of the  $C_2$  function, the absolute magnitudes of these two functions fall away more rapidly than the  $C_2$  function. Hence the behaviour of the interference function away from the origin becomes more and more dominated by the slowest varying functions  $C_1 (=7)$  and  $C_2$ . The fact that the interference function never takes negative values may be visualised as follows. If the sum of two slowest varying functions  $C_1$  and  $C_2$  is considered, only in one region, from  $\sim 3.0$  to  $\sim 4.5$  does the function take negative values. If the sum of the functions  $C_3$  and  $C_4$  is considered, then it can be seen by inspection that  $(C_1 + C_2) > (C_3 + C_4)$  hence the total function  $I_1 = (C_1 + C_2 + C_3 + C_4)/49$  can never take negative values.

### 4.3.2 The $I_2$ interference function

The interference function  $I_2$ , due to 19 points in a centred hexagonal array is given by equation (9) viz:

$$I_2 = 1/19^2 [19 + 84J_0(X) + 54J_0(2X) + 24J_0(3X) + 6J_0(4X) \\ + 60J_0(\sqrt{3}X) + 72J_0(\sqrt{7}X) + 24J_0(\sqrt{13}X) \\ + 18J_0(2\sqrt{3}X)] \quad - (9)$$

The function  $I_2$  is composed of 9 functions  $C_1, \dots, C_9$ , taken in order of appearance in equation (9) i.e  $C_1 = 19$ ,  $C_2 = 84J_0(X)$  etc. As with the  $I_1$  function, the largest weighted component  $C_2$  is the function involving the slowest varying Bessel function  $J_0(X)$ . The sum,  $(C_1 + C_2)$  of  $I_2$  is much larger than the equivalent partial sum of the  $I_1$  interference function, due obviously to the additional numbers of lattice points included in the array and also the fact that these extra lattice points introduce extra phase variability of "length X". This is however compensated for by the additional numbers of the type  $C_3, C_4$  as per the  $I_1$  interference function, together with additional "phasing" terms viz,  $J_0(\sqrt{7}X)$ ,  $J_0(\sqrt{13}X)$  etc.

The addition of the "extra" terms in  $I_2$ , as compared to the  $I_1$  interference function does not alter in any major way the overall shape of the  $I_2$  function, v's the  $I_1$  function, as can be seen in diagram (6). This is due to the fact that although there are additional terms included in the interference function, these extra terms are varying so rapidly c.f the basic term viz,  $J_0(X)$ , that the effects produced by them are short lived. The main influence of these additional terms being to affect the graph in the region of the central peak of the interference function, and to resolve certain other peaks.

### 4.3.3 The $I_3$ Interference Function

The  $I_3$  interference function due to 37 lattice points, is composed of 16 terms  $C_1, \dots, C_{16}$ , defined in the order of appearance in equation (10) viz:-

$$\begin{aligned}
I_3 = 1/37^2 [ & 37 + 180J_0(X) + 138J_0(2X) + 96J_0(3X) + 54J_0(4X) \\
& + 24J_0(5X) + 6J_0(6X) \\
& + 144J_0(\sqrt{3}X) + 216J_0(\sqrt{7}X) + 144J_0(\sqrt{13}X) + 72J_0(\sqrt{21}X) \\
& + 24J_0(\sqrt{31}X) + 78J_0(2\sqrt{3}X) + 96J_0(\sqrt{19}X) + 36J_0(2\sqrt{7}X) \\
& + 24J_0(3\sqrt{3}X) ] \quad - (10)
\end{aligned}$$

The fastest varying term in equation (10) is  $C_7 = 6J_0(6X)$ , which is varying at 6 times the rate of the  $C_2$  components, so that by the time that  $X$  attains the value , the  $C_7$  components of the interference function is almost insignificant compared to the  $C_2$  function.

#### 4.3.4 The $I_4$ Interference function

The  $I_4$  interference function, viz

$$\begin{aligned}
I_4 = 1/61^2 [ & 61 + 312J_0(X) + 258J_0(2X) + 204J_0(3X) + 150J_0(4X) + 96J_0(5X) \\
& + 54J_0(6X) + 24J_0(7X) + 6J_0(8X) + 264J_0(\sqrt{3}X) + 432J_0(\sqrt{7}X) \\
& + 336J_0(\sqrt{13}X) + 240J_0(\sqrt{21}X) + 144J_0(\sqrt{31}X) + 72J_0(\sqrt{43}X) \\
& + 24J_0(\sqrt{57}X) + 174J_0(2\sqrt{3}X) + 264J_0(\sqrt{19}X) + 180J_0(2\sqrt{7}X) \\
& + 96J_0(\sqrt{39}X) + 36J_0(2\sqrt{13}X) + 96J_0(3\sqrt{3}X) + 120J_0(\sqrt{37}X) \\
& + 48J_0(7X) + 30J_0(4\sqrt{3}X) ] \quad - (11)
\end{aligned}$$

contains 25 terms consisting of the weighted values of the zero order Bessel Function, all varying at different rates, with the exception of terms  $C_8 + C_{24}$ , both of which contain the term  $J_0(7X)$ , ie correspond to lattice vectors of the same length, and are due to the lattice vectors (7,0) and (5,3) respectively. This is accounted for by the fact that as the size of the lattice increases, the greater the probability that within a given lattice there will be two vectors  $(l_1m_1)$ ,  $(l_2m_2)$  whose lengths are equal. For this to be so, the following relation between the components holds:

$$l_1^2 + l_1m_1 + m_1^2 = l_2^2 + l_2m_2 + m_2^2 \quad - (12)$$

As already noted, there are 2 lattice vectors of length 7 present in the  $L_4$  lattice, and onwards  $L_5$ .....etc. No more multiplicities of lengths are encountered until  $L_8$ , which contains 317 lattice points, where the vectors of length 13 and 14 occur twice.

As an example of the duplication of vectors it may be seen that for vectors of the type  $(7n,0)$ ,  $(n = 1,2,3\dots)$  the following relation holds:

$$\begin{aligned} \text{If } \langle(1,m)\rangle &= \sqrt{1^2 + 1m + m^2} \\ \text{then } \langle(7n,0)\rangle &= \langle(5n,3n)\rangle \quad - (13) \end{aligned}$$

So that, provided the lattice contains enough points then equation (13) holds. A similar relation may be seen to be valid.

For vectors of the type  $(13n,0)$ ,  $(8n,7n)$  etc. the fastest varying terms present in the  $I_4$  interference function is  $C_9 = 6J_0(8X)$ .

#### 4.4 ANALYSIS OF THE INTERFERENCE FUNCTIONS

By inspection of Figure 30 (the composite functions), it is evident that after a certain value of  $X$  is attained, the faster varying composite functions make considerably less contribution to the interference function than do the slower varying functions. This is easily seen for example in the cases of the  $C_2 (= 312J_0(X))$  and the  $C_9 (= 6J_0(8X))$  component functions since  $C_2/C_9 = 312/6 = 52$ , at  $X=0$ .

The main contribution to the interference function of the faster varying component functions present in the interference functions  $I_1 - I_4$  therefore seems to be in the vicinity of the central peak of the interference function, where the various weights of the said functions are utilised to the best effect. The contributions of these functions falling off to zero very rapidly, eg in the case of the  $C_9$  component function which has the value  $|C_9| = 0.4$  at  $X=10$  compared to the  $C_2$  term which has the value  $|C_2| \sim 77$  which is to the slowest varying components present.

If the above argument is accepted, it follows that the form of the interference function is mainly determined by the slowest varying component functions that are present, with the faster varying components making their biggest contribution to the form of the central peak, and making practically no contribution to the form of the interference function as  $X$  takes on higher values.

With the appropriate choice of functions included in any interference function, it may be possible to reduce a complicated interference function which would otherwise include a large number of terms, to a relatively simpler one with fewer, slower varying terms.

The functions used for this work will however include the full number of terms present in the interference function, and not the reduced form with fewer terms.

Before discussing the significance of the four interference functions, as shown in diagram (6), it is useful to recall the definition of the interference function so that useful comparisons may be made between the four functions. The functions plotted in diagram (6) represent the "averaged" interference due each lattice point within the particular array, and is obtained from the "true" interference function by simply scaling the values in inverse proportion to the number of points within each array. This enables the contribution of each individual lattice point to its appropriate interference function to be examined, and how this contribution varies as more points are added to the lattice.

The  $I_1$  interference function due to seven points shown in diagram (6a) has a central main peak of magnitude unity, and has four well defined peaks of significant magnitude, in the range 0-20 X or kS. The central peak is of half width ~2.40 kS.

The  $I_2$  interference function due to a 19 component lattice, diagram (6b) has a central main peak of half width ~1.5 kS and seven significant subsidiary peaks.

The  $I_3$  interference functions (diagram 6c) has a central main peak of half width ~1.2 kS and as with the  $I_1$  and  $I_2$  functions has seven subsidiary peaks. However, with the  $I_4$  function, (diagram 6d) there are eight well defined subsidiary peaks, the central peak being of half width ~1.0 kS.

As the number of points included within the lattice increases the central or main peak of the function decreases in half width from a value of  $\sim 2.5$  for the  $L_1$  lattice containing 7 points to a half width of  $\sim 1.0$  for the  $L_4$  lattice containing 61 lattice points. This trend is to be anticipated since the case of the interference function due to an infinite lattice should result in a series of delta functions at specified intervals that are determined by the planes of points present within the lattice and which are characteristic of the hexagonal lattice.

As with the central peak, the first subsidiary peak gets narrower as the number of points included in the lattice increases, from a width of  $\sim 4.2$  kS in the  $I_1$  case to  $\sim 2.6$  kS for the  $I_4$  case. Along with this decrease in peak width, there is also a decrease in the magnitude of the peaks as the lattice expands, from  $I$  (kS)  $\sim 0.33$  for  $L_1$  to  $I$  (kS)  $\sim 0.11$  for  $L_4$ . The second subsidiary peak present in the  $I_1$  function of width  $\sim 6.2$  kS, is very quickly resolved into two peaks in the  $I_2$  and subsequent interference functions, the total width of the pair also decreasing to a value of 3.2 kS progressing through the functions  $I_2 \dots I_4$ . In similar fashion, the other subsidiary peaks present in the four functions both decrease in width and amplitude, and in some cases are resolved into a pair of peaks. As individual peaks are resolved, the resulting pair of peaks tend to maintain a constant ratio between the magnitudes of the two peaks.

The decrease in peak amplitude may be explained by the fact that inherent in the interference function is the scaling factor. It is this factor that is responsible for this fall off in amplitude of the subsidiary peaks.

Indicated on the diagram (6a,b,c,d) are the positions of the peaks that result from the interference function due to an infinite hexagonal lattice. With relatively few numbers of points in the lattice, as in the  $L_1$  case, peak merging occurs, for example, in the (11) and (20), the (21) and (30) and the (22) and the (31) cases as the numbers of lattice points are increased, as in the  $L_2$  to  $L_4$  series of lattices, resolution of the merged

peaks into their component occurs. With a lattice consisting of 19 components, all of the merged peaks, except the (22), (31) case have resolved in sufficient detail to enable their component peaks to be identified.

With the  $L_4$  lattice, the (22), (31) set has just resolved sufficiently to identify the separate components.

Inspection of the diagram (6a,b,c,d) shows that the positions of these subsidiary peaks, changes little (at least to the resolution in  $kS$  used) as the numbers of lattice points increases. With finer resolution in  $kS$  it may be possible to estimate the numbers of component points in the particular lattice given the interference function, by say noting the position of one of the prominent peaks such as the (10) reflection which at least over the range of lattices used is strong compared to the other reflections observed.

Once sufficient numbers of lattice points are included, the general form of the interference function remains fairly uniform (allowance being made for the change in magnitude of respective values due to the scaling function). For example, there appears to be less relative change over the  $I_2$  to  $I_4$  interference functions, than comparing the  $I_1$  to  $I_2$  interference functions. If the lattices used are compared over the range say of 0-20  $kS$ , then it may be seen that the  $I_3$  and  $I_4$  lattices show a more or less identical pattern, again due allowance being made for the scaling factor. It may be inferred that the  $I_3$  lattice therefore represents a reasonable minimum approximation to the case of the infinite two dimensional hexagonal lattice.

Apart from the "standard" Bragg reflections that are characteristic of the hexagonal lattice, diagram (6) shows the presence of a number of non-Bragg peaks of significant magnitude, whose appearance may be explained by analogy with the diffraction pattern resulting from a one dimensional array of slits with varying numbers. When the numbers are low, the diffraction pattern consists of a series of broad peaks, as the number of slits ( $n$ ) increases, the main peaks occupy the same position but are narrower still with the attendant smaller peaks. Until in the case of the infinite array, only a series of delta functions is observed, with no subsidiary peaks at all.

The non-Bragg peaks present in diagram (6) are therefore due to the limited numbers of lattice points in the arrays  $L_1 - L_4$ . Recalling that the interference function is built up from a set of component functions varying at different rates (see Figures 31,32), it may be easily seen for example that in the vicinity of the origin, the presence of the non-Bragg peaks may be attributed to the faster varying component functions present within the interference function.

As the number of lattice points increases, so more rapidly varying terms are included in the interference function and serve to reduce the amplitude of these non-Bragg peaks in relation to the standard peak's, the amplitude of these non-Bragg peaks, eventually reducing to zero when  $L_x$  is attained.

The main problem, as far as the lattice function is concerned is the most efficient manner by which the lattice may be expanded.

A method used by Burge (18,19) to take account of lattices which are not highly symmetrical was to use the multiple interference function approach.

In line with the above approach, a suitable manner by which to expand a hexagonal lattice is shown below:

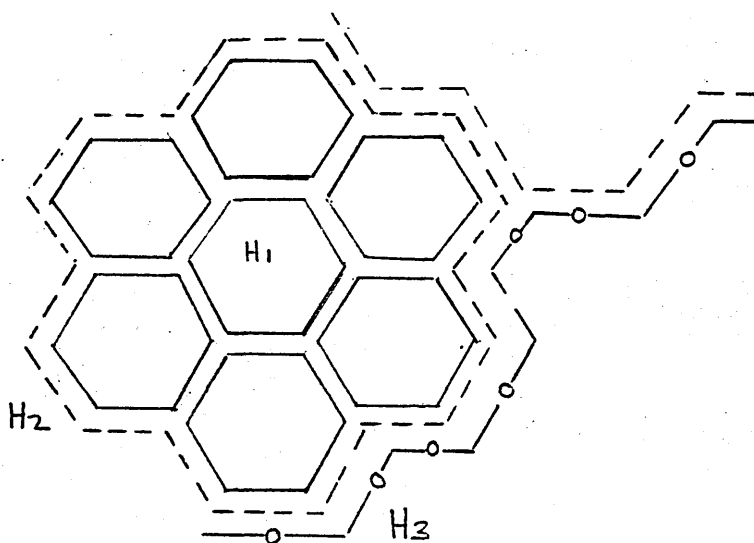


Figure 31

where  $H_1$  consists of a centred array of seven lattice points,  $H_2$  consists of a centred array of 7  $H_1$  units, and  $H_3$  consisting of a centred array of 7  $H_2$  units, and so on.

At each level  $H_1, H_2, H_3, \dots$  etc, there is a sevenfold increase in the number of lattice points when compared to the level below. For example,  $H_1$  contains 7 points,  $H_2$  contains  $7^2$  points, and  $H_3$  contains  $7^3$  points.

The interference function  $I(H)$  due to the lattice  $H_N$  may conceptually be written as

$$I(H) = HI_1 \cdot HI_2 \cdot HI_3 \dots HI_N \quad - (14)$$

where  $HI_1, HI_3, \dots$  etc are the interference functions due to  $H_1, H_2, \dots$  etc.

The interference function due to the  $H_1$  lattice is the same basic function used previously (see equation (8)..)

$$HI_1 = 1/7^2 [7 + 12J_0(X) + 24J_0(\sqrt{3}X) + 6J_0(2X)] \quad - (15)$$

At the second level of a diagram the lattice  $H_2$  may be represented by a similar function to that used for the  $L_1$  case.

$$HI_2 = 1/7^2 [7 + 12J_0(\alpha X) + 24J_0(\alpha\sqrt{3}X) + 6J_0(\alpha 2X)] \quad - (16)$$

The factor  $X$  included in equation (16) takes account of the scaling factor between the two levels, when the two functions are combined.

In similar manner, the  $H_3$  lattice interference function may be written

$$HI_3 = 1/7^2 [7 + 12J_0(\beta X) + 24J_0(\beta\sqrt{3}X) + 6J_0(\beta 2X)] \quad - (17)$$

and so on.

The interference function due to a lattice of  $7^n$  components may be compiled by taking  $n$  interference functions of the types defined by equations (15), (16), (17) as above, and forming their product function, i.e

$$HI_n = 1/7^2 [7 + 12J_0(X) + 24J_0(\sqrt{3}X) + 6J_0(2X)] \cdot 1/7^2 [7 + 12J_0(\alpha X) + 24J_0(\alpha\sqrt{3}X) + 6J_0(\alpha 2X)] \cdot 1/7^2 [7 + 12J_0(\beta X) + 24J_0(\beta\sqrt{3}X) + 6J_0(\beta 2X)] \dots - (18)$$

The mathematical advantage of modelling the interference function.. in this manner is that each of the "sub" interference functions is composed of the same basic unit -

$$\text{viz: } 1/7^2 [7 + 12J_0(\emptyset X) + 24 J_0(\emptyset\sqrt{3}X) + 6J_0(\emptyset 2X)]$$

where  $\emptyset$  = scaling factor appropriate to each sub-function.

Once the behaviour pattern of the sub-function, as defined above, is established, the behaviour of the overall lattice function should follow readily.

Diagram (7) shows the interference functions due to the  $H_1$ ,  $H_2$ ,  $H_3$  and  $H_4$  lattices, containing 7, 49, 343 and 2401 lattice points, respectively.

The  $H_2$  lattice consisting of 49 lattice points should produce an interference function whose form follows closely that due to the  $L_3$  and  $L_4$  lattices, with due allowance being made for the scaling factors etc. This does not appear to be the case since the  $H_2$  lattice produces an interference function consisting of a series of more or less evenly spaced peaks.

The departure of the behaviour of the H series of lattices as compared to the L series is even more marked when the  $H_3$  and  $H_4$  lattices are considered. With the comparatively large numbers of points involved in the H series as opposed to the L series, it should be expected the interference function due to the  $\infty$  lattice should be approached rapidly ie in the  $H_2$  case. This is not found to be so.

This method, involving multiple interference functions, as indicated earlier, has found criticism by such authors as Vainshtein<sup>36</sup> and Tyson and Woods<sup>37</sup>. Comparing the L and H lattices, it is evident that the interference functions due to the latter lattices, do not generate sufficient lattice vectors, or equivalently phase relations between the scattered waves. This accounts for the fact that no consistent behaviour is observed in the interference functions due to the H series of lattices. Accordingly, this approach will not be considered further.

CHAPTER 5

MODEL PARAMETERS - THE SWELLING FACTOR

## 5.1 INTRODUCTION

In order to allow for varying inter-cylinder separation within any particular array of model cylinders, the concept of the "swelling" factor has been adopted.

Inter-cylinder separation may be specified in two ways. Firstly in terms of the separation between the boundaries of the cylinders, and secondly between the centres of the cylinders. The latter method has been adopted here.

The swelling factor ( $\gamma$ ) was first introduced by Oster and Riley<sup>(13,15)</sup> in order to account for the hydration or lateral swelling of a lattice of macro-molecules or fibrous material. Their definition as presented below is also employed here.

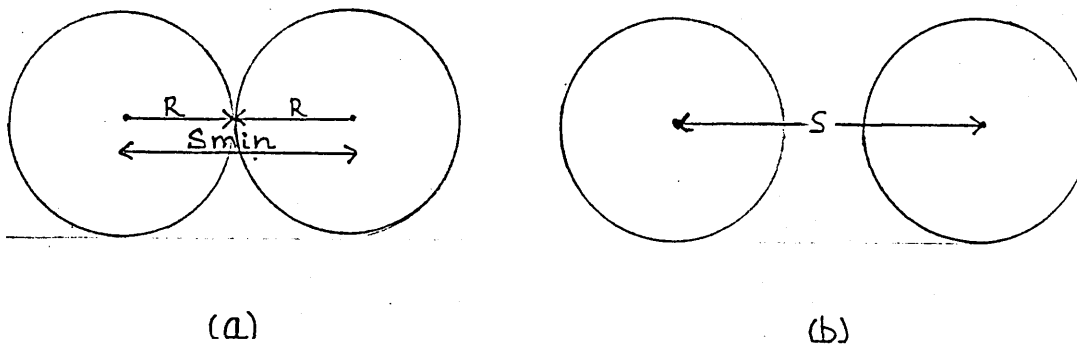


Figure 32

The separation  $S$  between a pair of nearest neighbours is given by

$$S = 2\gamma R \quad - (1)$$

where  $\gamma$  = swelling factor

$R$  = cylinder's radius.

Inspection of Figure 32 shows that the minimum possible separation  $S_{\min} = 2R$  for which  $\gamma_{\min} = 1.0$ , hence fixing a lower limit for the range of values of  $\gamma$ . A  $\gamma$  value  $< 1$  might be taken to imply either of two things, a) that the array is so compacted

that cylinder deformation is occurring, or b) that the cylinders are so "nebulous" that inter-cylinder penetration takes place. Neither case is allowed within the definition of the model used here. It is the function of the swelling parameter then, to allow for variations in the packing of the cylinders.

## 5.2 THE SWELLING FACTOR AND ITS RELATION TO THE DIFFRACTION EQUATION

In order to illustrate the relation of  $\chi$  to the diffraction equation, the diffraction model for an array of seven solid cylinders is considered. The diffraction equation due to the above array may be written in the following form:

$$I = F^2(kR) \cdot 1/7^2 [7 + 24J_0(kS) + 12J_0(\sqrt{3}kS) + 6J_0(2kS)] - (2)$$

where I = scattering intensity due to the array

$F^2(kR)$  = scattering function of the cylinder

$k$  = scattering vector

Equation (2) contains the variables R and S, defining the radius and separation of the cylinders, respectively. Recalling the definition of the swelling factor (equation 1), enables equation (2) to be written in either of the following two forms:

$$I = F^2(kR) \cdot 1/7^2 [7 + 24J_0(2\chi kR) + 12J_0(2\sqrt{3}\chi kR) + 6J_0(4\chi kR)] - (3)$$

or

$$I = F^2(kS/2\chi) \cdot 1/7^2 [7 + 24J_0(kS) + 12J_0(\sqrt{3}kS) + 6J_0(2kS)] - (4)$$

Equation (4) is the most convenient form of the diffraction equation, due to the fact that since the variable S, which represents the distance between lattice points, is used for the independent variable, the interference function will always give the "standard" Bragg reflections in the same places (on the graph), irrespective of the value of  $\chi$ . This enables easy comparisons to be made between arrays of cylinders, as  $\chi$  takes different values.

The swelling factor may be thought of as operating on the cylinder's scattering function by effectively shrinking the cylinders radius and retaining constant S instead of expanding the lattice, (ie increasing S) for constant cylinder radius.

The effect of the swelling factor on the components of the diffraction equation is more clearly seen with the aid of the following diagram.

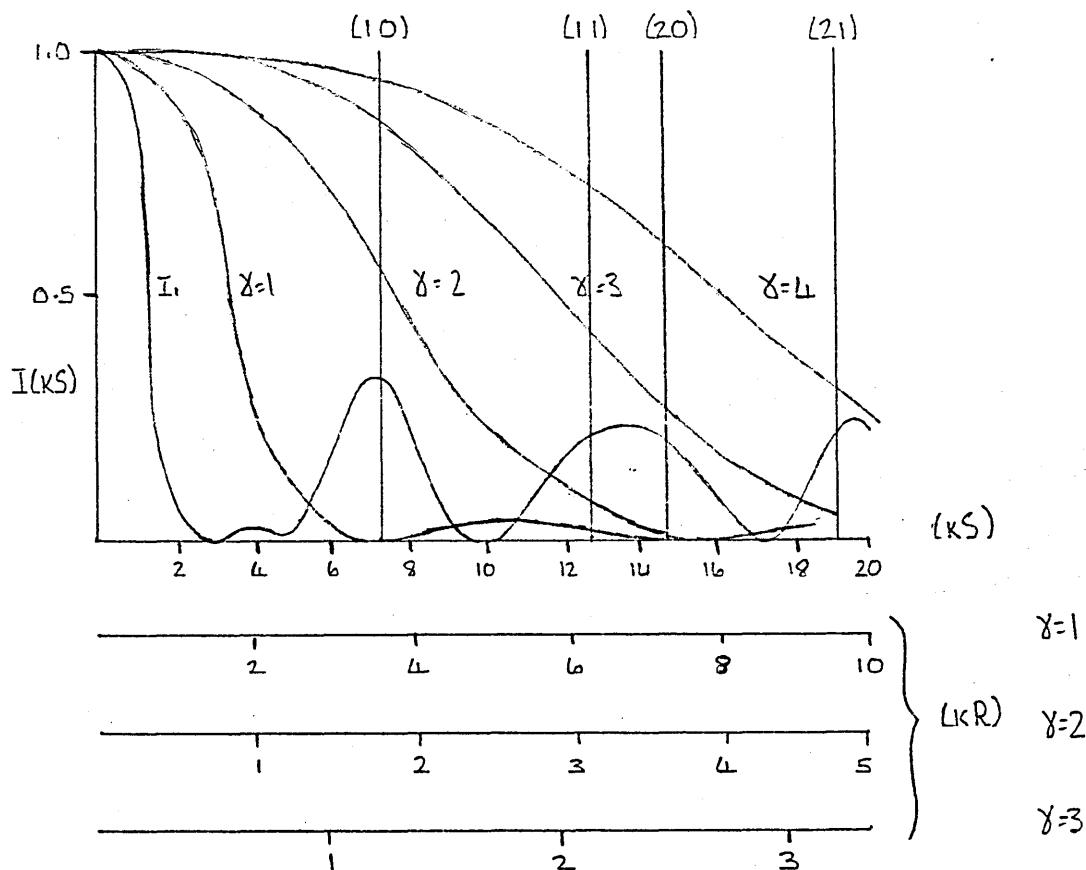


Figure 33

Figure 33 shows the graphical representation of the two main components of the interference function ie the scattering profile of the cylinder and the lattice interference function. The interference function is represented by  $I_1$ , and uses the horizontal  $(kS)$  scale, whilst the scattered intensity profiles due to the solid cylinder, labelled  $\gamma = 1, \gamma = 2$ , etc. use the appropriately labelled  $kR$  scales. As is shown, in the diagram, the value of  $\gamma$  determines the range of  $kR$  values of the SIP that combine with the interference function to form the diffraction pattern. At the higher values of  $\gamma \geq 2$ , it is evident that it is only the central peak of the SIP that contributes to the diffraction pattern, over the range 0 - 20 in units of  $kS$ .

Also made clear from Figure 33 is the reason for scaling the cylinder's radius rather than the lattice. With the lattice parameter being fixed, the standard Bragg peaks due to a complete hexagonal lattice, will always appear in the same  $kS$  positions. If the diffraction pattern were plotted as a function of  $(kR)$ , rather than  $(kS)$ , then due to the fact that the lattice parameter is "scaled-up", the Bragg peaks will change positions as the value of  $\chi$  is changed. Thus, this method of presenting the results, enables the diffraction patterns produced by the various arrays of cylinders to be easily compared.

### 5.3 THE EFFECTS OF VARIATION IN $\chi$ ON THE DIFFRACTION PATTERN

Diagram (8) shows the diffraction patterns due to seven solid cylinders in a hexagonal array with various values of  $\chi$ , ranging from 1.0 - 5.0, the former value representing the case where the cylinders are in contact, whilst the latter represents the case where the cylinders' centres are separated by ten times the cylinder's radius.

The following points are noted, from diagram (8). The number of well defined peaks present is dependent on the value of  $\chi$ . The case  $\chi = 1$  has only a single central peak of half width  $\sim 2.40 kS$ . At a value of  $\chi = 2$ , two subsidiary peaks are evident, the first one being a non-Bragg peak, centred about a  $kS$  value  $\sim 3.8$ , and of magnitude  $\sim 0.03$ . The second of these peaks corresponds to the (10) Bragg reflection, centred about  $kS \sim 7.0$  and of magnitude  $\sim 0.14$ . For  $\chi = 3$ , there are 3 subsidiary peaks present, the second and third of these peaks corresponding to the (10) and a merged (11) and (20) peak, of magnitudes 0.23 and 0.06 respectively.

For  $\chi = 4$ , there are 4 subsidiary peaks, the second, third and fourth of these peaks corresponding to the reflections (10), ((11), (20)) and (21) reflections of magnitudes 0.27, 0.11 and 0.04 respectively.

At  $\delta = 5$ , the values of these Bragg peaks are 0.28, 0.12 and 0.07 respectively. Over the range of  $\delta$  used in the diagram, the non-Bragg first subsidiary peak that is present increases in magnitude from 0.03 at  $\delta = 1.0$ , to 0.04 at  $\delta = 5.0$ , and also shifts in position from  $kS = 3.8$  to  $kS = 3.9$  for the respective values of  $\delta$ .

As a general feature of diagram (8) all of the subsidiary peaks observed have a) increased in number, b) increased in magnitude, c) have broadened and d) have changed their position to higher values of  $kS$ .

#### 5.4 ANALYSIS OF THE CHANGES IN THE DIFFRACTION PATTERN DUE TO VARIATIONS IN $\delta$

All of these features may be explained by recourse to Figure 33. Taking the  $\delta = 1$  and  $I_1$  cases as shown, the value of  $\delta = 1$  curve is sensibly zero after a  $kS$  value of  $\sim 7.2$ , so that the product of these two functions for values of  $kS > 7.2$  may be taken to be zero. The product function is dominated by the faster varying term  $I_1$ . From Figure 33, it may be estimated that the central peak of the product function (ie the diffraction pattern) should be  $\sim 2.2$   $kS$  in half width. The values of the product function for  $kS$  values between 2.0 and 7.2 are negligible.

As the value of  $\delta$  increases, the interference function ( $I_1$ ) combines with a smaller range of the various SIP ( $\delta$ ) curves that are shifted to higher values. It is to be expected then, that more variation be introduced into the product function. For example a (10) peak might be expected at  $\delta = 2$  but no others since the SIP ( $\delta = 1$ ) tails off in the region of the (11) interference peaks.

At values of  $\delta = 3, 4, 5$  etc, the "full range" of the Bragg peaks that are encompassed by the  $I_1$  function should be seen.

Items b), c), d) mentioned above (section 5.3), are due to the fact that the value of  $\delta$  chosen changes the magnitudes and slopes of the ranges of the SIP ( $\delta$ ) that combine with the  $I_1$  function, in the vicinities of the relevant "Bragg-regions".

The non-Bragg peak is seen more clearly at higher values of  $\delta$ , since the value of  $I_1$  in this region is multiplied by almost unity, and as explained earlier (see page 98), this peak is due to the limited numbers of lattice points, ie cylinders in the array.

For very large separations between the cylinders, assuming the diffraction equation is still valid, the  $I_1$  function would effectively combine with an SIP ( $\delta$ ) which is almost unity over the whole range of  $(kS)$  values of  $I_1$ , so that the diffraction pattern should tend to a limiting set of values.

If the function  $I_1$  is replaced by  $I_2, I_3, I_4$  etc, then recourse to the above discussion supports the idea that for a given type of structured cylinder, the form of the diffraction pattern should change little over the various values of  $\delta$ , and the various  $I_n$  functions used. Some additional resolution of the diffraction peaks occurring as more cylinders are added to the array.

It is evident from the above discussion that whichever particular model cylinder is chosen to include in the diffraction equation with the various lattice functions, only a very limited range of the particular SIP is ever used. The maximum range of values of  $kR$  that is used in forming the product function, or diffraction pattern, over a given range in  $kS$  is determined by the case of the cylinders in contact according to the relation  $kR = (kS/2\delta)$ , with  $\delta = 1$ . So that for example, if the range defined for  $kS$  is 0 to 20, with the cylinders in contact, the range of  $kR$  is 0 to 10. At  $\delta = 2$ , the range of  $kR$  is 0 to 5, and so on.

With the solid cylinder, Figure 33 shows that it is only the central peak in the SIP that takes any part at all in determining the diffraction pattern. As well as the width or extent of the central peak, it is obvious that the shape of the central peak must also affect the final form of the diffraction pattern.

Variations in electron density profile (EDP) also affect the diffraction pattern due to the fact that changes in the half width of the central peak and the introduction of subsidiary peaks occur.

If, as already mentioned, the diffraction model is valid for very large values of  $\chi$ , then no matter what structured cylinder is chosen to include in the model, it will only be the shape and extent of the central peak that ultimately decides the form of the diffraction pattern for a given lattice.

CHAPTER 6

MODEL DIFFRACTION PATTERNS

## 6.1 INTRODUCTION

The set of cylinders with EDPs in the range (1111111111) to (1000000000), with  $\Delta\rho_e = -1$  are used in various arrays in an attempt to analyse certain general features that are present in the model's diffraction pattern. The above set of cylinders will be considered in the basic  $L_1$  array of seven components, with various values of  $\gamma$ . Certain of these cylinders will then be used to illustrate the trends occurring in the diffraction pattern as the number of components in the array is increased.

The next set to be considered is the series representing a two level electron density distribution, ie a cylinder with an inner portion of varying width and electron density, in the  $L_3$  array of 37 components.

Finally a series of cylinders that might be taken to represent a reasonable approximation to the micellar electron density distribution will be examined in the  $L_3$  lattice configuration.

Recalling the diffraction equation described earlier (see section 5.2 )

$$I = F^2(kS/2\gamma) \frac{1}{7^2} [(7+24J_0(kS) + 12J_0(\sqrt{3}kS) + 6J_0(2kS))] \quad - (1)$$

for seven cylinders in a centred hexagonal array of seven components

where  $F^2(kS/2\gamma)$  is given by the function

$$F^2(kS/2\gamma) = \frac{\left[ 2 \left[ \rho_{10}(kS/2\gamma) J_1(kS/2\gamma) + (\rho_9 - \rho_{10})(0.9)(kS/2\gamma) J_1(0.9(kS/2\gamma)) \right. \right. \\ \left. \left. + \dots + (\rho_1 - \rho_2)(0.1)(kS/2\gamma) J_1(0.1(kS/2\gamma)) \right] \right]^2}{\left[ (kS/2\gamma)^2 (\rho_{10} + (\rho_9 - \rho_{10})0.9^2 + \dots + (\rho_1 - \rho_2)(0.1^2)) \right]^2} \quad - (2)$$

Note that instead of using  $kR$  as the independent variable in (1) the radius parameter has now been scaled by the  $\gamma$  factor ( see section 5.2 ).

The (1111111111) cylinder has already been discussed in the  $L_1$  configuration (see section 5.3), but the main points will be reiterated in order to maintain continuity in the following discussion.

The diffraction patterns due to a solid cylinder (EDP = (1111111111)) in the  $L_1$  array are shown in diagram (8) and as previously noted, the number of peaks present depend on the value of  $\delta$ . The case of the cylinders in contact,  $\delta = 1$  displays only a single main peak of half width  $\sim 2.40$  kS. For  $\delta = 3$  there are three subsidiary peaks present, the second and third peaks corresponding to the (10) and a merged ((11),(20)) peak, of magnitudes 0.23 and 0.06 respectively. The first subsidiary peak being a non-Bragg peak of intensity  $\sim 0.03$ .

The effects on the diffraction pattern of reducing the electron density of the innermost two shells of the cylinder to zero are shown in diagram (9). For  $\delta = 1$ , only the single main peak of half width  $\sim 2.49$  kS is observed, and to the level of resolution used, no difference is detected between this case and the (1111111111) case, in terms of peak width.

For  $\delta = 2$ , two subsidiary peaks are observed, the first of magnitude  $\sim 0.03$ , positioned at kS  $\sim 3.8$ , and the second of magnitude  $\sim 0.14$  positioned at kS  $\sim 7.0$ . The width of the central peak again is  $\sim 2.40$  kS in half width.

At  $\delta = 3$ , there are three subsidiary peaks present of magnitudes 0.04, 0.23 and 0.06 at kS values of 3.8, 7.0 and 12.40 respectively. The half width of the central peak has increased to  $\sim 2.60$  kS.

As the width of the zero electron density region of the cylinder increases to 40% of the radius ie EDP = (111110000), diagram (10) the case of the cylinders in contact  $\delta = 1$ , shows no detectable difference in central peak width from the cases described earlier (half width  $\sim 2.40$  kS), and no other peaks being observed.

At  $\gamma = 2.0$  the half width of the central peak is 2.40 and two subsidiary peaks are observed at  $kS = 3.8$  and  $6.8$  of magnitudes 0.03 and 0.12 respectively.

As  $\gamma$  increases to 3.0, the central peak's half width has not changed, but the magnitudes of the first two subsidiary peaks have increased to 0.04 and 0.22 respectively. The positions of these peaks have not changed from the previous case. A third subsidiary peak is also present of magnitude 0.05 and positioned at  $kS \sim 12.40$ .

Diagram (11) shows the set of diffraction patterns due to an array where the cylinders zero electron density region is 60% ie EDP = (1111000000). The  $\gamma = 1$  or contact case, shows that the half width of the central peak is still constant at 2.40  $kS$ , but there is a single subsidiary peak present centred at  $kS = 7.8$ , corresponding approximately to the (10) Bragg peak.

At  $\gamma = 2$ , again no change in the central peak is noticeable, but there are three subsidiary peaks present, the first positioned at  $kS \sim 3.8$  and of magnitude 0.03. The second peak at  $kS \sim 6.8$  is of magnitude 0.10 and corresponding to the (10) Bragg reflection, whilst the third peak at  $kS \sim 19.0$  is of magnitude 0.03 and corresponds to the (21) Bragg reflection.

At  $\gamma = 3$ , 3 subsidiary peaks are observed, the first non-Bragg at  $kS \sim 3.8$  and of magnitude 0.04, the second and third Bragg peaks positioned at  $kS = 7.0$  and  $12.4$  and of intensities 0.20 and 0.03 respectively. Note the "change" in position of the third subsidiary peak from the (21) position to the merged (11), (20) position.

The diffraction patterns due to the cylinder with the inner 80% of zero electron density is shown in diagram (12).

As with all the cases previously discussed the central peak's half width remains constant at  $\sim 2.4$   $kS$  throughout this series. At  $\gamma = 1$ , one subsidiary peak is present in the (10) position, centred at  $kS \sim 7.6$ , and of intensity 0.04. No other peaks are observed.

At  $\chi = 1.5$ , two subsidiary peaks are present in the non-Bragg position at  $kS \sim 3.8$  of magnitude 0.02, and in the ((11), (20)) position of magnitude 0.03 and position  $\sim 13.0$ .

Four subsidiary peaks are observed at  $\chi = 2.0$ , three of which correspond approximately to the Bragg reflections (10), (20) and (21) at positions of  $kS = 6.6, 14.6$  and  $18.8$  and of intensities 0.08, 0.02 and 0.03 respectively. The first subsidiary peak (non-Bragg) is of intensity 0.03 at  $kS = 3.8$ .

At  $\chi = 2.5$ , three subsidiary peaks are present, two of which correspond approximately to the (10) and (21) reflections. The intensities of these two peaks being 0.13 and 0.03 at  $kS = 6.8$  and  $19.4$  respectively. But at a  $\chi = 3.0$ , only one Bragg peak is observed (10), at  $kS = 7.0$  and of intensity 0.18, apart from the non-Bragg peak at  $kS \sim 3.8$ , no other subsidiary peaks are observed.

The diffraction patterns due to the thin shell, where the inner 90% of the cylinder has zero electron density, EDP = (1000000000) are shown in diagram (13). Throughout this series of diffraction patterns, the central peak's half width, as with the other models discussed earlier, remains constant at a value of  $\sim 2.4 kS$ .

The contact case  $\chi = 1.0$  exhibits only a single subsidiary peak centred at  $kS = 7.6$  and of intensity 0.05. A single subsidiary peak is also present at  $\chi = 1.5$ , but this time corresponds to the ((11), (20)) peak, and is centred at 12.8 and is of intensity 0.03. With the  $\chi = 2.0$  case, the peaks (10), (20) and (21) are present at  $kS = 6.6, 14.4$  and  $18.8$  and of intensities 0.06, 0.03 and 0.03 respectively.

With the  $\chi = 2.5$  case the (20) peak has disappeared, leaving the (10) and (21) peaks of intensities 0.12 and 0.04 respectively. Again in the  $\chi = 3.0$  case, the (10) and (21) peaks are present of intensities 0.17 and 0.02 respectively.

As will be noted from the above presentation of the results for the (1111111111) to (1000000000) series of cylinders in the  $L_1$  array, the extremes of the range viz (1111111111) and (1000000000) form the limiting cases for the diffraction patterns of the whole series of cylinders, the rest of the series exhibiting behaviour intermediate between these two cases. For the  $L_2$  lattice consisting of 19 components only the (1111111111) and the (1000000000) cylinders will therefore be representative of the behaviour limits of the whole series in this configuration.

The diffraction patterns due to the solid cylinder and the thin shell in the  $L_2$  configuration are shown in diagrams (14) and (15).

From diagram (14) which shows the diffraction patterns due to the  $L_2$  array of solid cylinders, the first point of note is that the half width of the central peak is  $\sim 1.60$  kS, as opposed to the  $L_1$  array of solid cylinders. This peak width remains at the same value throughout the range of  $\chi$  values used. The case  $\chi = 1$  has in common with the  $L_1$  ( $\chi = 1$ ) case only a single central peak, but at  $\chi = 1.5$  only 1 subsidiary peak is observed in the (10) position of intensity 0.04 at kS = 7.0. The non-Bragg peak in the vicinity of kS 3.8 is absent unlike the  $L_1$  ( $\chi = 1.5$ ) case.

At  $\chi = 2.0$ , two subsidiary peaks are present the first at kS  $\sim 2.2$ , and of magnitude  $\sim 0.02$ , and the second at kS  $\sim 7.2$  and of intensity 0.08 and corresponding to the (10) peak.

At  $\chi = 2.5$ , again only 2 subsidiary peaks are present in the same position as the  $\chi = 2$  case, but of intensities 0.02 and 0.12 respectively. Again at  $\chi = 3.0$ , only two subsidiary peaks are observed, as in the previous 2 cases of magnitude respectively.

Comparing the cases of the solid cylinder in the configurations  $L_1$  and  $L_2$  it is evident that the corresponding (10) peak intensities in the  $L_2$  are reduced pro-rata from the  $L_1$  case by a factor of  $\sim 2$ . The half width of the main peak has also been reduced from a value of  $\sim 2.2$  in the  $L_1$  case to kS  $\sim 1.6$  in the  $L_2$  case.

The position of the first subsidiary peak present in the  $L_2$  case has "moved" to a  $kS$  value of  $\sim 2.2$  and has again been reduced in intensity by a factor of  $\sim 2$ .

Diagram (15) shows the diffraction patterns due to the (1000000000) cylinder in the  $L_2$  configuration. In common with the solid cylinder/ $L_2$  series, the half width of the central peak has decreased to a value of  $\sim 1.6$  for this series, and again a corresponding reduction in intensities in the subsidiary peaks observed compared to the corresponding  $L_1$  cases. A peculiarity arises at  $\delta = 1.5$ , where no subsidiary peaks are observed, as compared to the  $L_1$  configuration.

At  $\delta = 2.0$  only one subsidiary peak is observed at  $kS \sim 7.0$  of intensity  $\sim 0.03$ , and is approximately half the value observed in the  $L_1$  case. For  $\delta = 2.5$ , as in the  $L_1$  case 3 subsidiary peaks are observed, the second and third of which correspond to the (10) and (21) Bragg peaks, positioned at  $kS = 7.2$  and  $19.2$ , of intensities  $0.07$  and  $0.02$  respectively, the first subsidiary peak is  $kS = 2.2$  and of intensity  $0.02$ .

At  $\delta = 3.0$ , only 2 subsidiary peaks are observed at  $kS = 2.2$  and  $7.2$  and of intensities  $0.02$  and  $0.10$  respectively, no (21) peak is observed as in the  $L_1$  case.

Diagrams (16) and (17) show the diffraction patterns due to the cylinders (1111111111) and (1000000000) in the  $L_3$  configuration, ie a centred hexagonal array of 37 points, and as shown earlier, the behaviour of the diffraction pattern for an  $L_3$  array of 37 cylinders represents a reasonable approximation to the diffraction pattern of an infinite array.

As can be seen from diagrams (16) and (17), the central peak has now decreased in half width to  $\sim 1.20$   $kS$  and a non-Bragg peak appears at  $kS \sim 1.60$ , and of intensity  $0.02$ . As the value of  $\delta$  increases from 1 to 3 the (10) peak increases in intensity from zero at  $\delta = 1$  to a value of  $0.10$  at  $\delta = 3$ . No additional peaks are observed until  $\delta = 2.5$  when the (11) peak is present and of magnitude  $0.01$ . At  $\delta = 3$  the (10) peak is of intensity  $0.10$  and the ((11),(20)) merged peak has now separated into two distinct

if low, intensity peaks of values 0.02 and 0.01 respectively.

The  $(\underline{1000000000})/L_3$  series are shown in diagram (17), For the  $\chi = 1$  case, there is only a single central peak of half width 1.2 kS. Only the (11) reflection of intensity 0.01, and a non-Bragg peak centred on  $kS = 1.6$ , and of magnitude 0.02 are present at  $\chi = 1.5$ . At  $\chi = 2$  the (10)m, (20) and (21) peaks are observed, of intensities 0.02, 0.01, and 0.01 respectively, in addition to the non-Bragg peak at  $kS = 1.6$ , the (20) peak being absent, the (10), and (21) peaks are of intensities 0.05 and 0.02 respectively, and again only the (10) and (21) peaks are present in the  $\chi = 3.0$  case, and are of magnitudes 0.07 and 0.01 respectively.

It will be noted from diagrams (8) and (17) which show the diffraction patterns due to the solid cylinder and thin shell in the various arrays  $L_1$ ,  $L_2$  and  $L_3$  that the arrays involving the solid cylinder produce a more consistent set of diffraction patterns than the thin shell series. As  $\chi$  increases from the contact case of 1.0, the number of peaks observed also increases in the case of the arrays containing the solid cylinder. This is not found to be the case for the thin shell, for example in the  $L_2/(\underline{1000000000})$  series as  $\chi$  increases from 1 to 1.5, the (10) peak disappears, but at  $\chi = 2.0$  is observed again, no (11), (20) reflections are noted, but the (21) peak appears for  $\chi > 1.50$ . In the  $L_3/(\underline{1000000000})$  series, no (10) reflection is observed for  $\chi < 2.0$ . The (11) reflection is present at  $\chi = 1.5, 2.0$  and 3.0 whilst the (21) peak is present at  $\chi = 2, 2.5$  and 3.0.

The above results will now be discussed using the theory developed earlier, and with the aid of the following diagram -

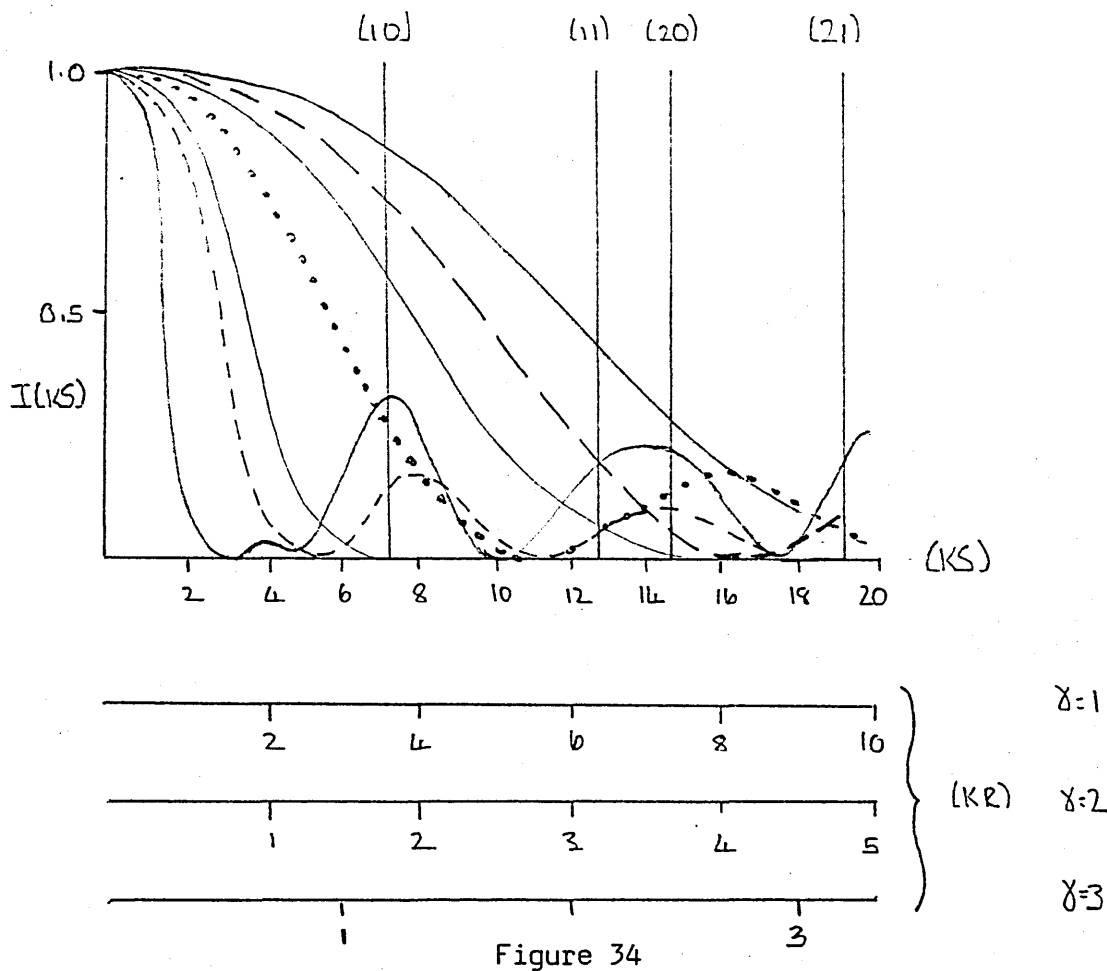


Figure 34

As already discussed, the diffraction pattern is formed from the product of the scattering function of the cylinder, and the lattice function. Figure 34 shows the three lattice functions  $L_1, L_2$  and  $L_3$  and also the ranges of the scattering profiles due to the solid cylinder and the 10% thick shell that combine with the lattice functions (see section 3.3). It is also useful at this point to recall that the diffraction patterns as presented represent the averaged contribution of each point in the array.

Considering the solid cylinder in the  $L_1$  array, it is the faster varying function  $I_1$  that dominates the true diffraction pattern, so that considering the  $I_1$  function and the solid cylinders scattering profile at  $\delta=1$ , the product of these two functions should give a central diffraction peak of half width  $\sim 2.4 kS$  at most and since the scattering profile is zero at equivalent values of  $kS > 6.8$ , no other peaks are to be expected.

As the value of  $\gamma$  increases through 1.5 to 2.0 the central peak at the solid cylinder's scattering profile is effectively broadened and encompasses a wider range of the  $I_1$  function. As a consequence the diffraction function might be expected to produce two peaks at  $kS$  values of approximately 4.0 and 7.2. This latter corresponding to the (10) Bragg reflection.

At  $\gamma = 3.0$ , the solid cylinder and the  $L_1$  lattice should produce 3 Bragg peaks ie 10, (11) and (20) the latter two peaks being merged. Also if figure 34 is examined the magnitudes of the (11) and (20) peaks should be considerably reduced in intensity (cf. the (10) peak).

It can be seen therefore, that recourse to Figure 34 and the previously developed theory, a satisfactory explanation of the diffraction pattern due to an  $L_1$  array of solid cylinders is obtained.

As shown in Figure 34 the difference between the  $I_1$  and  $I_2$  interference functions is one of intensity [again, recall that it is the lattice interference function that provides the "averaged" interference per lattice point].

At  $\gamma = 1$ , it is to be expected that there will only be a central peak due to the solid cylinder/ $L_2$  combination of half width  $\sim 1.2 kS$ .

As  $\gamma$  increases from 1.0 through to 2.0 or in the  $L_1$  case a (10) peak is to be expected. The non-Bragg peak that is observed in the ( $L_1/\gamma = 1.5$ ) case is not present, because due to the scaling factor built into the interference function, the amplitude of this peak is effectively zero, and it is this scaling factor that has reduced the amplitude of the (10) peak by almost 50% compared to the ( $L_1$ ) case.

Throughout the ( $L_2/\gamma = 1$  to 3) cases the major differences between the diffraction patterns due to the solid cylinder in the  $L_1$  and  $L_2$  series of lattices, is one of reduction in intensity of the subsidiary peaks, some of which are not present due to this factor.

The same is true as the number of solid cylinders in the array increases from 19 in the  $L_2$  lattice to 37 in the case of the  $L_3$  lattice, the general trend being a reduction in intensity in the amplitude of the peaks found in the previous two cases.

The case of the thin shell (EDP = 1000000000), in combination with the  $L_1$  to  $L_3$  series of lattice, diagrams (13), (15), (17), is seen to produce a series of diffraction patterns, that are not as predictable as the case of the solid cylinder and the same set of lattices. This is seen to be due to the fact that the scattering profile of the thin shell exhibits a series of subsidiary peaks that are not present in the case of the solid cylinder. Some of the "peculiarities" observed in the diffraction patterns due to the thin shell, are caused by the movement of these subsidiary peaks relative to the interference functions.

For the  $L_1$  array of thin shells, the following points are noted. At  $\gamma = 1$ , there is only a single main peak of half width  $\sim 1.2$  kS and from Figure 34 by combining the relevant  $I_1$  and thin shell scattering profiles for  $\gamma = 1$ , no other peaks should be observed.

From the Figure 34, it may be estimated that in the  $\gamma = 1.5$  case, there is a sufficient shift in the first zero of the thin shell's scattering profile to bring it into the vicinity of the (10) peak due to the interference function, their product being effectively zero. This is observed (see diagram (13)). The separated (11) and (20) peaks are caused by the fact that the second zero of the thin shell's scattering profile falls in between these particular (11) and (20) positions, effectively causing the combined (11),(20) peak of the  $I_1$  function to resolve into two separate peaks.

Progressing to  $\chi = 3.0$ , recourse to Figure 34 shows that, since the scattering profile falls off to zero in the vicinity of the (20) peak, there will be no (20) peak present in the diffraction pattern, see diagram (13).

In the same manner as for the solid cylinder, the effect of increasing the number of lattice points in general causes a reduction in peak amplitude, as the progression from  $L_1$  to  $L_2$  to  $L_3$  occurs.

Since the above two models ie the solid cylinder and the thin shell, in the various arrays  $L_1$  to  $L_3$  produce diffraction patterns that may be regarded as the limiting cases of a series of model arrays where cylinders of various thicknesses are considered. It follows therefore that the predictions made using the knowledge gained by investigating these two limiting cases, may with reasonable validity be applied to any intermediate cases.

The general principles upon which predictions are made as to the features that ought to be found in a particular diffraction pattern, are as follows. Again reference is made to Figure 34. The three main components that combine to produce the diffraction pattern are the scattered intensity profile, the swelling factor and the interference function. The form of the interference function is quickly established, and the  $L_1$  array of seven points shows all the features that are present in the  $L_2$  and  $L_3$  arrays of 19 and 37 components respectively. However at the higher numbers of lattice points resolution of certain of the peaks occur.

It follows therefore, that since the lattice function is to a first approximation constant (apart from diminished magnitudes) the chief sources of variation in the diffraction pattern are the scattering function due to the particular type of cylinder, and the swelling factor  $\chi$ . For a given type of cylinder, it is the swelling factor that produces the variations in the diffraction pattern.

As clearly demonstrated, a cylinder which possesses an SIP with several subsidiary peaks will introduce the most variation into the diffraction equation. For the cases already considered the maximum number of subsidiary peaks that are useful in determining the shape of the diffraction pattern is governed by the case of the  $\infty$  thin shell, ie by  $J_0(kR)$  and it is the range of  $kS$  used for the interference function that actually selects the number of subsidiary peaks of the scattering profile that play a part in the diffraction pattern.

It may be said then that no matter what structured cylinder is taken, that even the limited amount of cases discussed, the general features of the diffraction patterns variation with cylinder type and numbers is now established. Even the case of the reverse sawtooth (see diagram 4), with only the single peak of half width  $\sim 5.0 kR$ , should produce a diffraction pattern when considered in the  $L_1, L_2, L_3$  array that starts at an equivalent solid cylinder case where  $\chi = 2.0$ .

The diffraction patterns due to an  $L_3$  array of infinitely thin shells are shown in diagram (18). For the case  $\chi = 1$ , the (10) and (20) peaks are present, and of magnitudes 0.02 and 0.01 respectively. At  $\chi = 1.5$ , the (10) and the (20) peaks are absent, but the (11) and (20) peaks are present, being both of magnitude 0.01. At  $\chi = 2.0$ , the (10), (11), (20) and (21) peaks are all present, and of magnitudes 0.02, 0.01, 0.01 and 0.01 respectively.

At  $\chi = 2.5$ , only the (10) and (21) peaks are present, and are of magnitudes 0.04 and 0.02 respectively, and at  $\chi = 3.0$ , again only the (10) and (21) peaks are observed, and are of magnitudes 0.06 and 0.01 respectively.

Throughout the whole of this series, there is a non-Bragg peak present, centred at  $kS \sim 1.6$ , and of almost constant magnitude ( $\sim 0.02$ ).

Contrasting this case with that of the 10% thick shell, it will be noted that the basic trends exhibited by the thin shell or (1000000000) case, are followed by the infinitely thin shell case, for example, the sequence of appearance and disappearance of the (10) peak.

The magnitude of the (10) peak is always found to be marginally greater in the (1000000000) case than in the case of the infinitely thin shell, but in the main, the reverse appears to be true when the (11), (20), (21) peaks are considered. In general, the diffraction peaks due to the infinitely thin shell are narrower than their counterparts in the 10% thick case, although for both cases, the central peak's width is of the same magnitude throughout.

Since the SIP due to the infinitely thin shell exhibits narrower scattering peaks, than the SIP due to the (1000000000) shell, then the combination of a given lattice function and the above two SIPs should produce narrower diffraction peaks in the former case.

Also, since the scattering peaks due to the infinitely thin shell are greater in magnitude than those due to the (1000000000) shell, it might be expected that in general, the diffraction peaks due to the former case should be greater than those due to the later case. This does not appear to be true, and may be explained by the fact that for the two series of diffraction patterns considered, only a limited value of  $\chi$  is used, and that the particular increments in  $\chi$  always select particular regions where the SIP due to the (1000000000) shell has the greater magnitude of the two cases considered.

The effect on the diffraction pattern is that the (10) peak is strongest in the (1000000000) shell case c.f. to the equivalent peak in the case of the infinitely thin shell.

As a final series of examples to confirm the hypothesis advanced in this work, the following series of cylinders, whose EDP are in the range (1111NNNNNN) where  $N = 8$  to  $2$  with  $\Delta p_e N = -2$ .

The series of electron density profiles representing the above series are shown in diagrams 19-22, as are the corresponding diffraction patterns.

On the basis of the theory previously outlined, since the EDP of the cylinder is intermediate between that of a solid cylinder (1111111111) and a thin shell (1000000000) then the diffraction patterns obtained from the  $L_3$  array at various values of  $\delta$  should also be intermediate between the diffraction patterns due to the solid cylinder and the thin shell.

The (1111888888) case, since the electron density profile differs very little from the EDP of the solid cylinder, should exhibit a diffraction pattern similar to that of the solid cylinder. Examination of diagrams (16) and (19) confirm this. There is a slight reduction in intensity of the peaks that are observed with this case, compared to the solid cylinder case. This at first might seem contrary to the facts since as the density of the inner part of the cylinder is reduced relative to the outer part, diagram (19) (the EDP's) show that, enhancement of the SIP should occur, therefore the intensities of the observed peaks should increase. This apparent anomaly is explained by the fact that accompanying an increase in peak intensities, as the cylinder changes by degrees into a shell, there is also a shift in peak position, and a change in the width of the central peak. Recourse to Figure 34 shows this to be valid.

As the relative electron density of the inner portion of the cylinder falls to 0.2 over the 6 inner shells of the cylinder, so the diffraction profiles exhibited by this series, tend to those of the thin shell. This is confirmed by inspection of diagram (22), and noting that the appearance and disappearance of certain of the peaks present in the diffraction pattern, follow similar trends to those observed in the case of the diffraction patterns due to the thin shell.

The whole of the work presented in this thesis may be described as the determination of the behaviour of combinations of the zero and first order Bessel functions, the scattering function due to the motif or cylinder being expressed in terms of combinations of  $J_1(X)$ , and the lattice interference function being expressed in terms of combinations of  $J_0(X)$ .

The behaviour of the SIPs due to the various structures, falls in the main between the cases of the SIPs due to the infinitely thin shell, and the solid cylinder. The main characteristics of these SIPs are a central peak, and a series of subsidiary peaks, which show a gradual fall off in intensity with distance from the origin. For a given range of  $KR$  in the SIP, the infinitely thin shell exhibits narrower, and more numerous scattering peaks than does the solid cylinder.

The "thick-thin" shell series exhibits intermediate behaviour to the cases described above, with the numbers of subsidiary scattering peaks in a given range decreasing as the progression from a thin shell to a solid cylinder occurs. There is also an attendant decrease in intensity of these subsidiary peaks. The SIP due to the "reverse saw-tooth" EDP exhibits only a single central scattering peak with the greatest width of any of the models considered.

The SIPs due to the "moving" shell series of cylinders exhibits different characteristics to those of the "thick-thin" shell series. At certain separations of the shells, certain of the subsidiary peaks that are typically present in the "thick-thin" series for example, are absent. Also in contrast to the "thick-thin" series of SIPs, the magnitudes of the scattering peaks, in some of the cases due to the "moving" shell series, do not exhibit the gradual fall off in intensity as the distance from the origin increases.

The interference function due to an infinite 2-D hexagonal lattice may be approximated with reasonable confidence by the interference function due to an array with relatively few points. The main differences between the interference functions  $I_1$  to  $I_4$  being in the resolution of certain of the "standard" Bragg peaks, for example in the case of the  $I_1$  interference function where the (11) and (20) peaks are merged, but resolved in the case of the  $I_2$  interference function. It has been shown elsewhere (17), that the positions of these "standard" peaks change very little as the numbers of lattice points is increased, thus giving support to the contention that only the interference functions due to a limited array need be used to approximate to that due to the infinite case.

Consideration of the interference functions  $I_1$  to  $I_4$  shows that the  $I_3$  interference function due to an array of 37 lattice points provides a reasonable "minimum" approximation to the case due to the infinite lattice.

Having established the behaviour of the separate components of the diffraction pattern ie the SIP due to the cylinder, and the lattice interference function, the behaviour of a wide range of structured cylinders in an infinite hexagonal array may be predicted with reasonable accuracy, by recourse to a diagram of similar nature to that shown in Figure 34.

The sometimes complex nature of the diffraction pattern due to a particular array of cylinders, being explained by the shift in the peaks in the scattering profile, relative to the interference function, due to variations in the swelling factor ( $\delta$ ), ie the separation between centres of the cylinders in the array.

For any given array of structured cylinders, it is seen that only a relatively small part of the SIP is "useful" in determining the form of the diffraction pattern. For any given interference function  $I$ , the range of  $(kR)$  in the SIP due to the cylinder used to produce the diffraction pattern, is given by  $(S/2\delta)$ . If a range of  $kS = 0$  to 20 is taken as a reasonable figure for low-angle X-ray diffraction work, then a range of  $kR = 0$  to 10 is the maximum of the SIP that is ever used to form the diffraction pattern.

It therefore follows that it is the central peak and perhaps one or two at the most, of the subsidiary peaks of the SIP, that are important. In particular it is the position and extent of the first subsidiary peak of the SIP, determined by the first two zeros as they change position as  $\delta$  changes, that serve to introduce the variation into the diffraction pattern at low values of  $\delta$ .

As  $\delta$  takes on higher values  $\gg 5$ , the form of the diffraction pattern, for a given  $I$ , is determined completely by the shape and extent of the central peak of the particular SIP being used.

The behaviour of the diffraction patterns due to the structured cylinders considered in this work, fall in between the two limiting cases defined by the solid cylinder and the thin shell. This is to be expected since for a given array the dominant influence on the diffraction pattern is the SIP of the cylinder, which as already noted is limited by the two extreme cases, described above.

The diffraction patterns due to arrays of solid cylinders and thin shells are easily distinguished, by amongst other things, the change in intensities of the various Bragg peaks as the swelling factor ( $\delta$ ) changes, and also by comparing the shape and extent of the central diffraction peak. Consider for example, the  $L_3$  array of solid cylinders with  $\delta = 1$ , there is only the central peak in evidence, whilst for the corresponding case of the thin shell (10% R thick), the (10) reflection is observed.

In the case of the solid cylinder, as  $\delta$  increases, there is an orderly progression in the appearance of the various Bragg peaks, starting at  $\delta = 1.5$ , where the (10) peak is seen. At  $\delta = 2.5$ , the (10) and (11) peaks are present, whilst at  $\delta = 3.0$ , the (10), (11) and (21) peaks are evident. This progression is maintained until the thickness of the shell approaches  $\sim 30\%R$ , below this value, the behaviour of the diffraction pattern follows the trends exhibited by the thin shell case.

The diffraction patterns due to the solid cylinder and the thin shell result from structures with EDPs that are quite distinct from one another. However, when such structures have EDPs that are little different, as for example, when the (1111111111) and the (1111111100), or (1111110000) and (1111000000) cases are compared, the differences between the respective pairs of diffraction patterns being small, but distinguishable as slight changes in the magnitude of the diffraction peaks, rather than by their presence or absence.

In such cases as the above, in order to distinguish between particular models it may be necessary to consider the respective diffraction patterns as a function of  $\chi$ , since comparison of the diffraction patterns at specific, well separated values ( $\chi = 1, 2, 3, \dots$  etc) may be misleading, as for example when comparing the thin shell (10%R) and the infinitely thin shell cases.

The diffraction theory and the models presented during the course of this work do not differ greatly from those presented in previous studies. Where this work differs, is that the specific components of the diffraction model have been examined in more detail than in previous works, in an attempt to gain a deeper insight into the way that each of these components affects the diffraction pattern. The use of a ten strip electron density profile being determined to be sufficient to illustrate the trends occurring in the diffraction pattern as the cylinder's structure is varied. Similarly, the behaviour of the interference function  $I_3$ , due to a centred hexagonal array of 37 points being determined to be sufficient to describe the behaviour of the interference function due to an infinite hexagonal lattice.

The diffraction pattern shows an interesting change in behaviour as the shell's thickness decreases to around 30%R. The use of an EDP with more strips, in any future work, might enable a more precise determination of the shell's thickness at which this change occurs. In conjunction with this, a range of diffraction patterns, due to suitable arrays of model cylinders with smaller increments in  $\chi$ , be examined.

Consideration of the above, might provide some useful information relating to arrays of shells of thicknesses around  $10\%R$ . Also, the consideration of models which allow for larger arrays of cylinders than in the case of the  $L_3$  array may also provide useful information in the way of diffraction peak definition and intensity.

The investigation of irregularities in the packing of the cylinders has not been considered in this work, but might be incorporated into some future study with some benefit.

Finally, in order to cater for any deformities that might exist in such micellar structures (or models of them), that have been examined during the course of this work, the consideration of a model incorporating a non-radially symmetric scattering unit might also provide a source of useful information.

DIAGRAMS

MODEL SCATTERING PROFILES AND DIFFRACTION PATTERNS

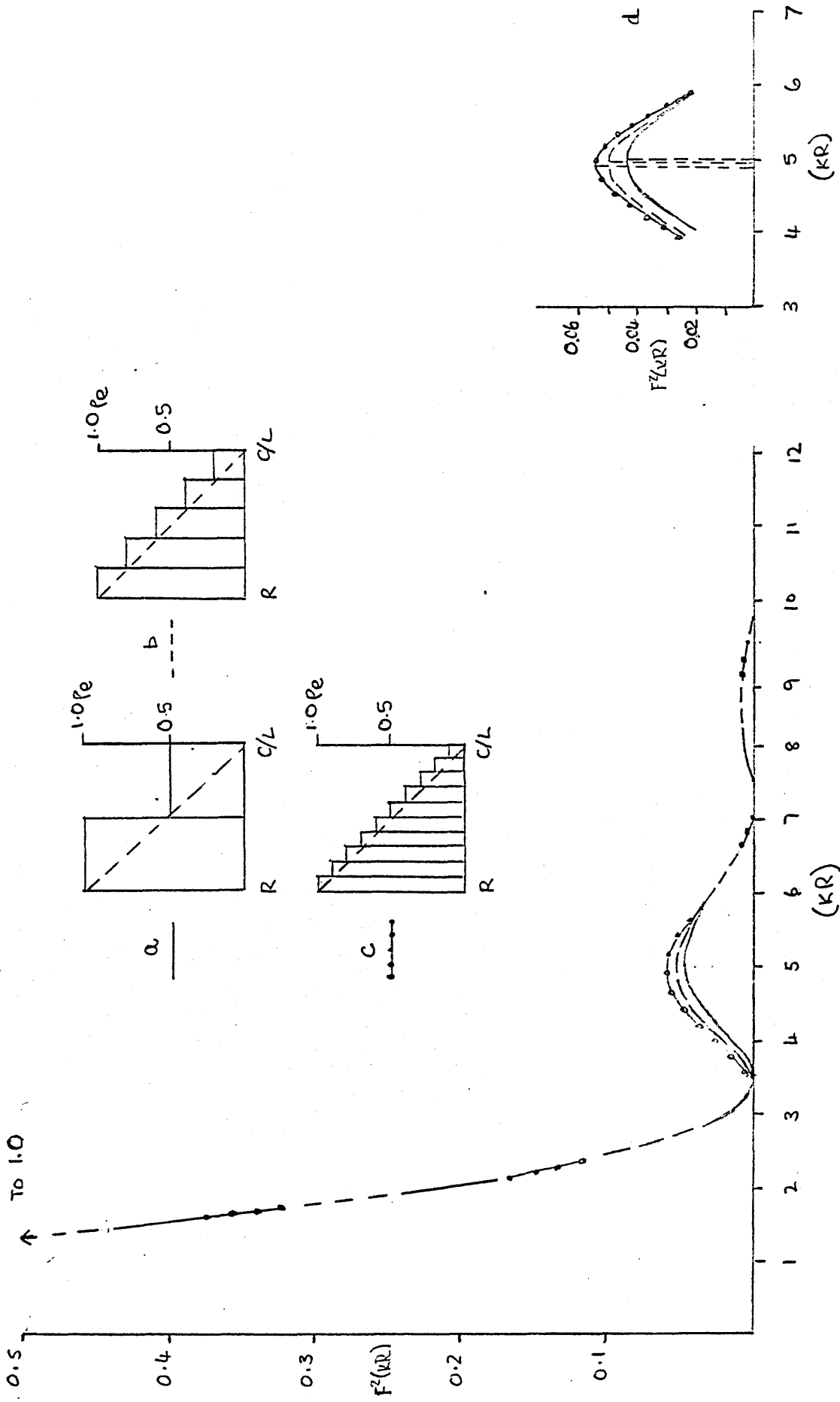


Diagram 1 Scattering Profiles due to a series of Cylinders with Smoothed Electron Density Profiles  
 Normalised Intensity of scattering ( $F^2(kR)$ ) for independent cylinders.

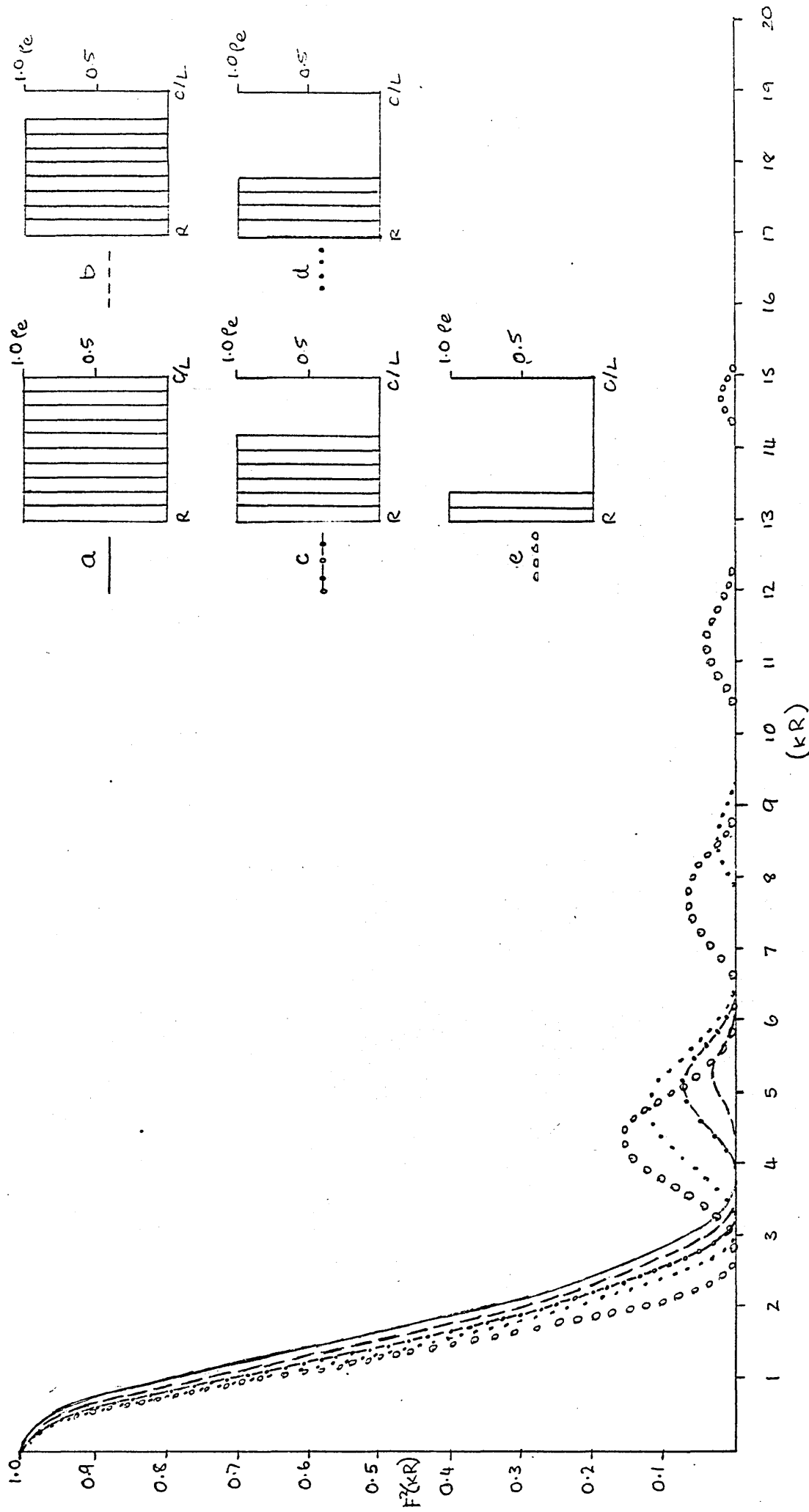


Diagram 2 Scattering Profiles due to a series of Cylindrical Shells of various thicknesses  
 Normalised intensity of scattering ( $F^2(kR)$ ) for independent cylindrical shells.

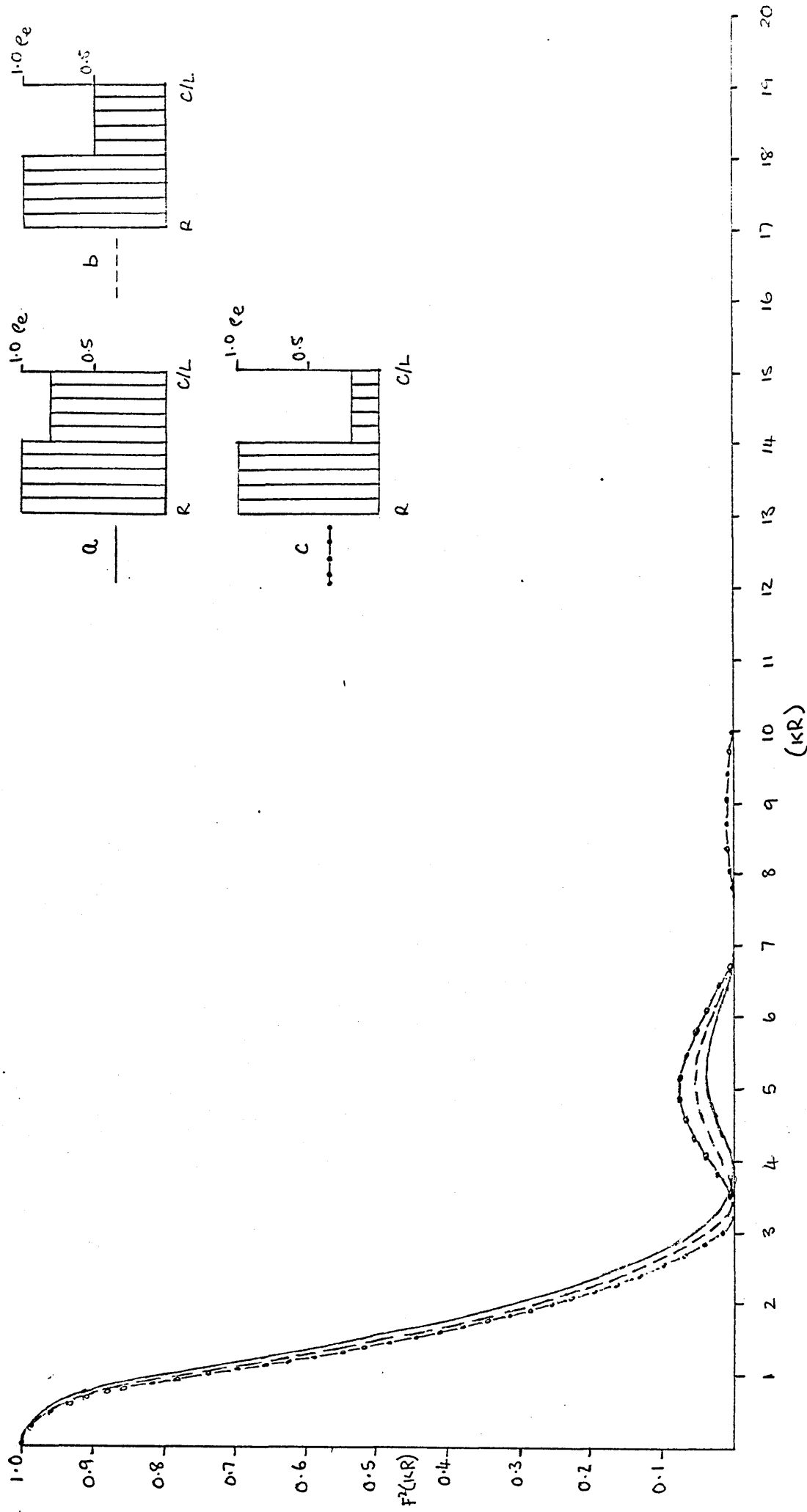


Diagram 3

Scattering Profiles due to a series of cylinders with two stage Electron Density Profiles

Normalised intensity of scattering ( $F^2(kR)$ ) for independent cylinders

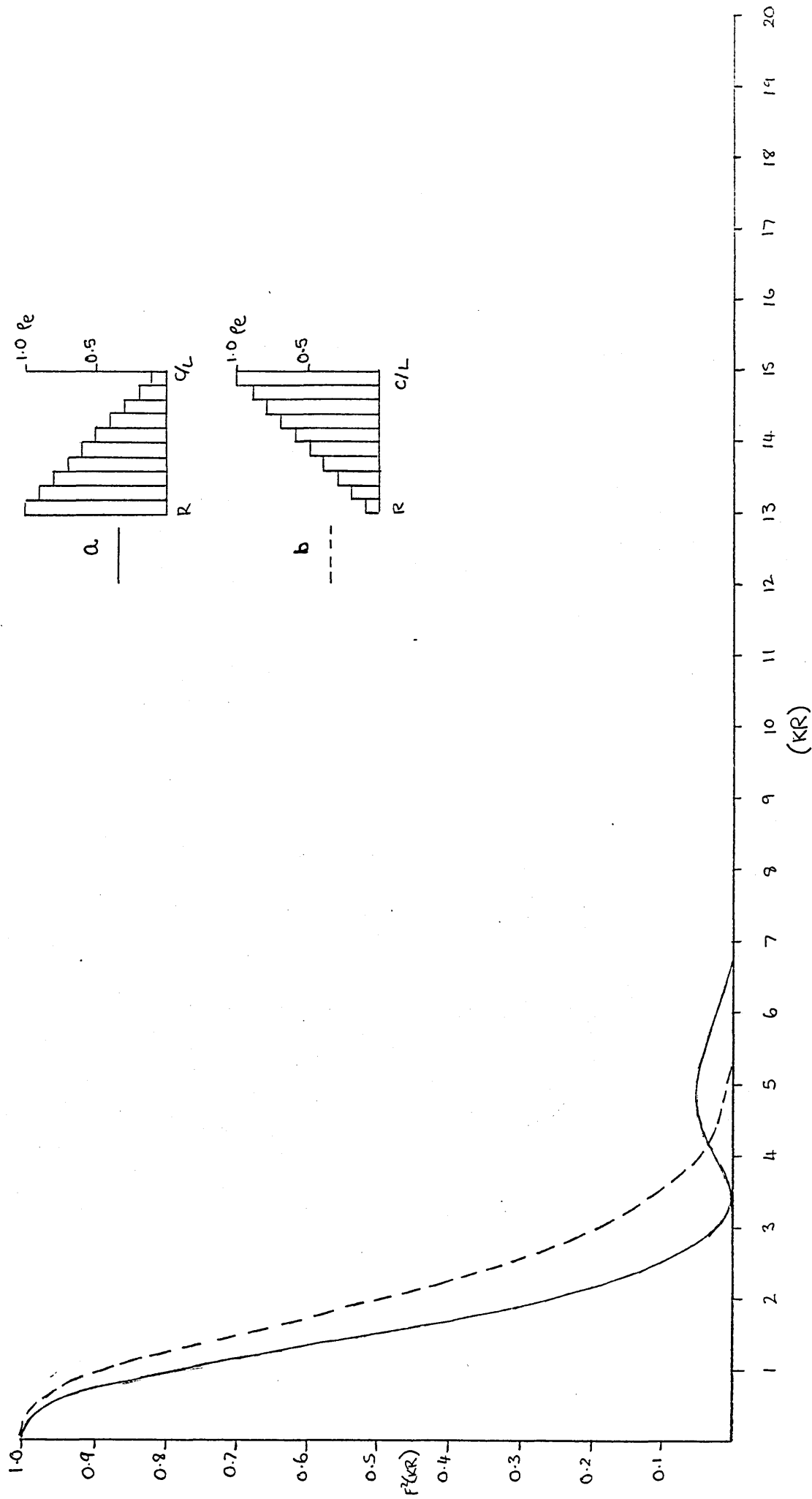


Diagram 4 Scattering Profiles due to a "Standard" Sawtooth and its mirror image. Electron Density Distribution. Normalized intensity of scattering ( $F^2(kR)$ ) for independent cylinders.

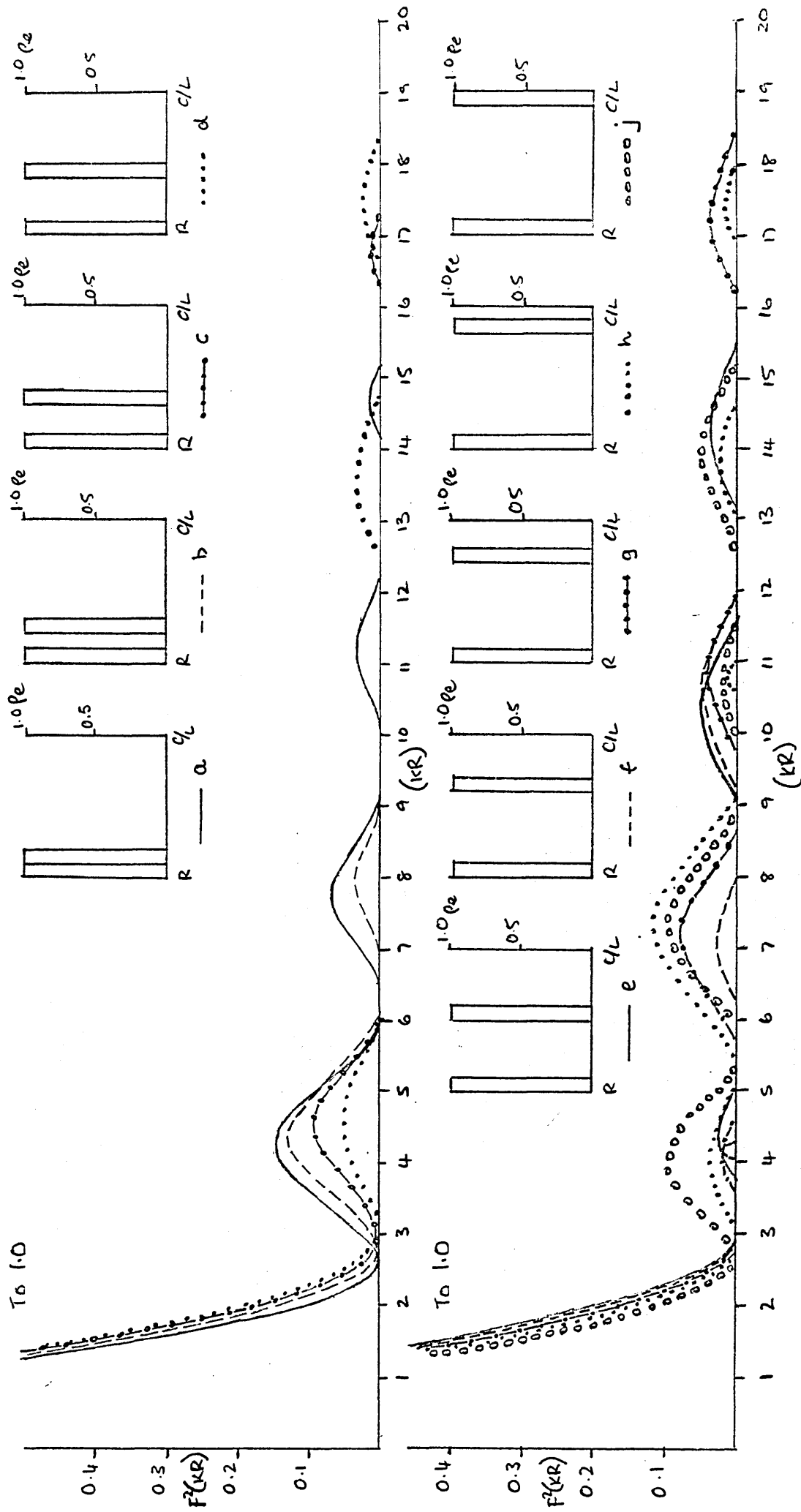


Diagram 5 Scattering Profiles due to the "Moving-Shell" series of Electron Density Profiles  
 Normalised intensity of scattering ( $F^2(kR)$ ) for independent cylindrical shells.

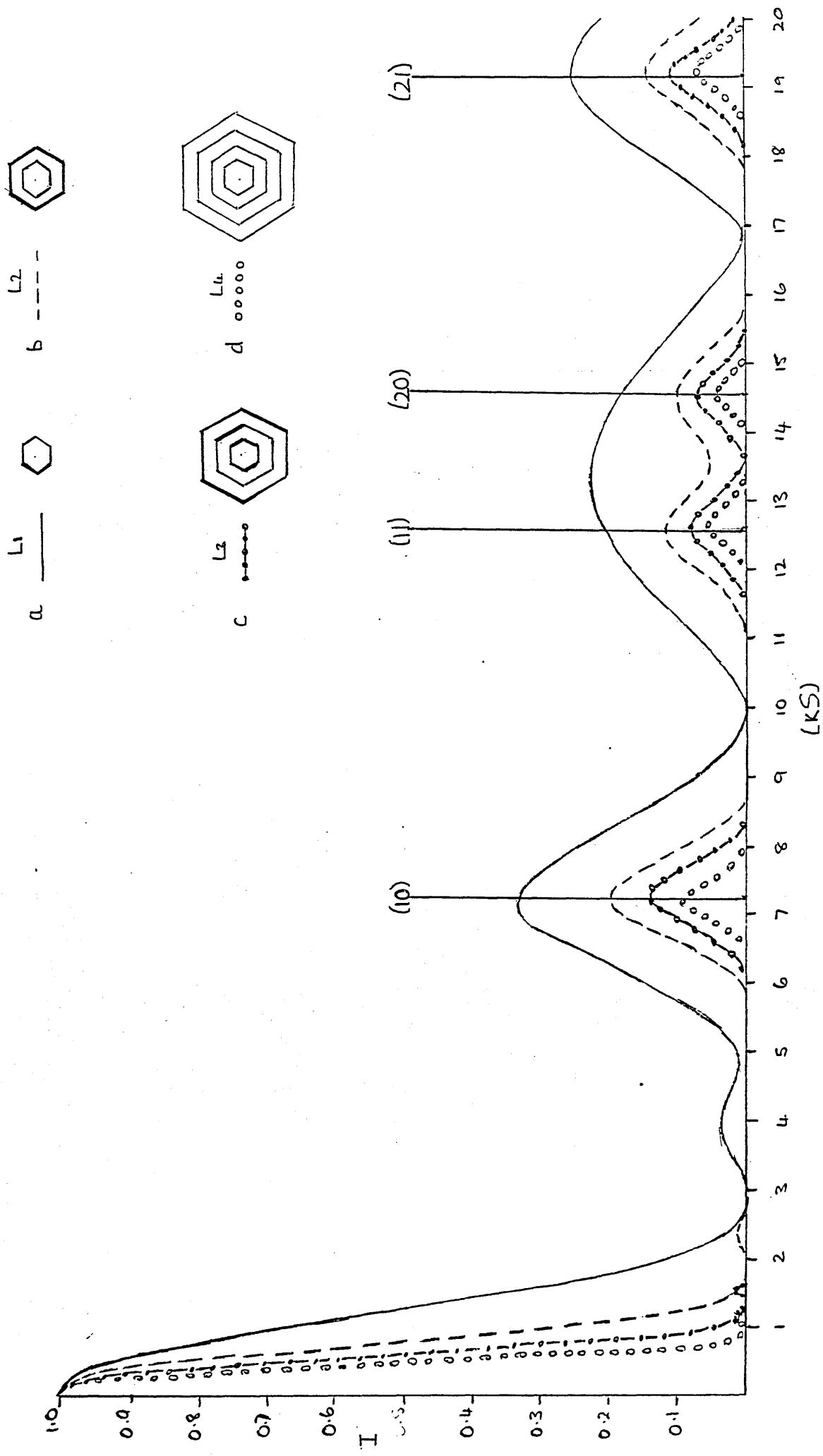


Diagram 6 The Interference Functions  $I_1 - I_4$   
 Variation in  $(I)$  with  $(kS)$ .

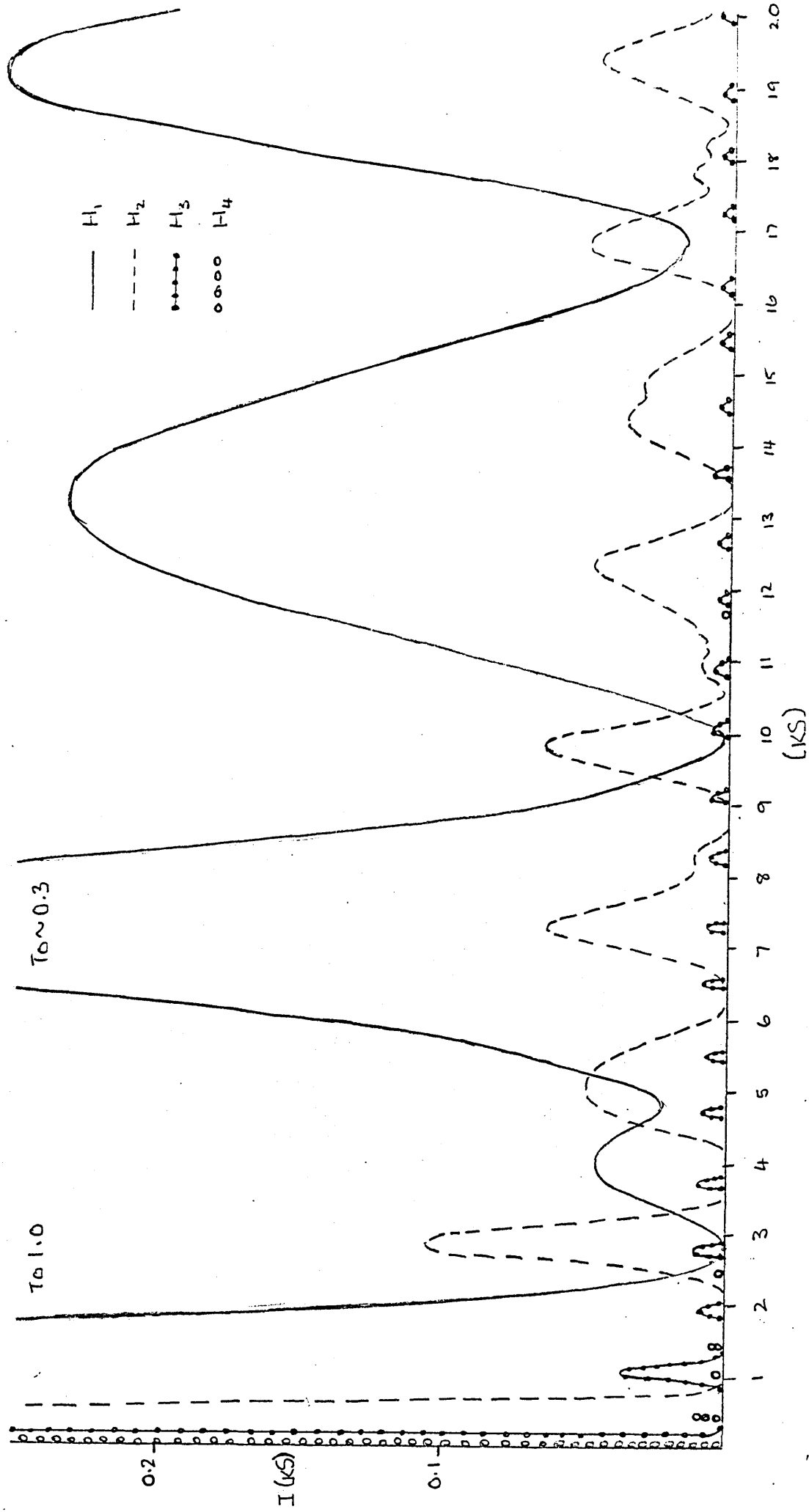


Diagram 7 The Interference Functions  $H_1-H_4$   
 Variation in (I) with (S)

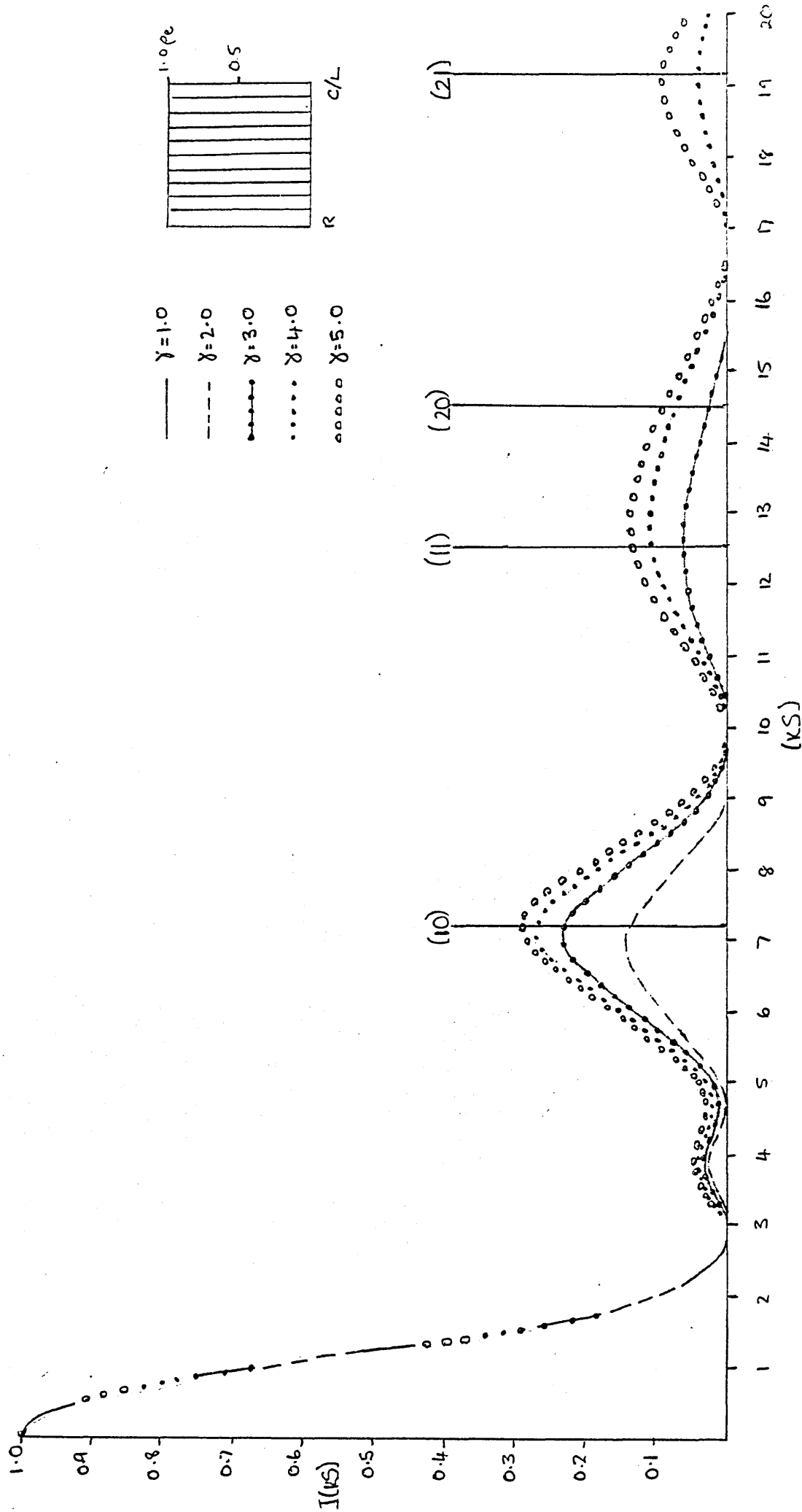


Diagram 8

The effects of variation in  $\gamma$  on the Diffraction Pattern due to a Hexagonal Array of Seven Solid Cylinders. Normalised intensity of scattering (I(x<sub>s</sub>)) per cylinder for independent aggregates.

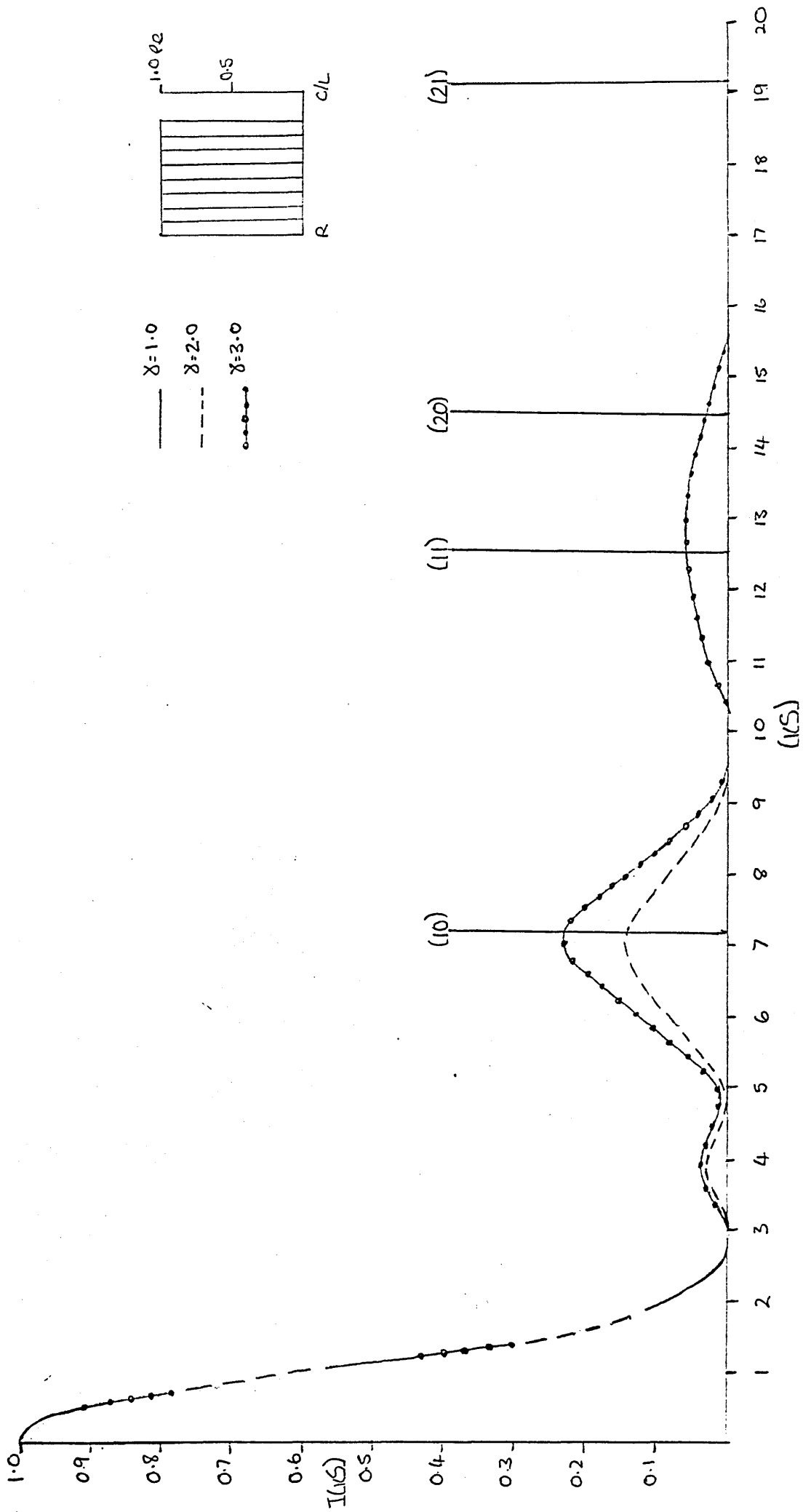


Diagram 9 The Diffraction Pattern due to a Hexagonal Array of Seven Shells (of 80% thickness) at various values of  $\delta$ . Normalised intensity of scattering  $I(r,s)$  per cylinder for independent aggregates.

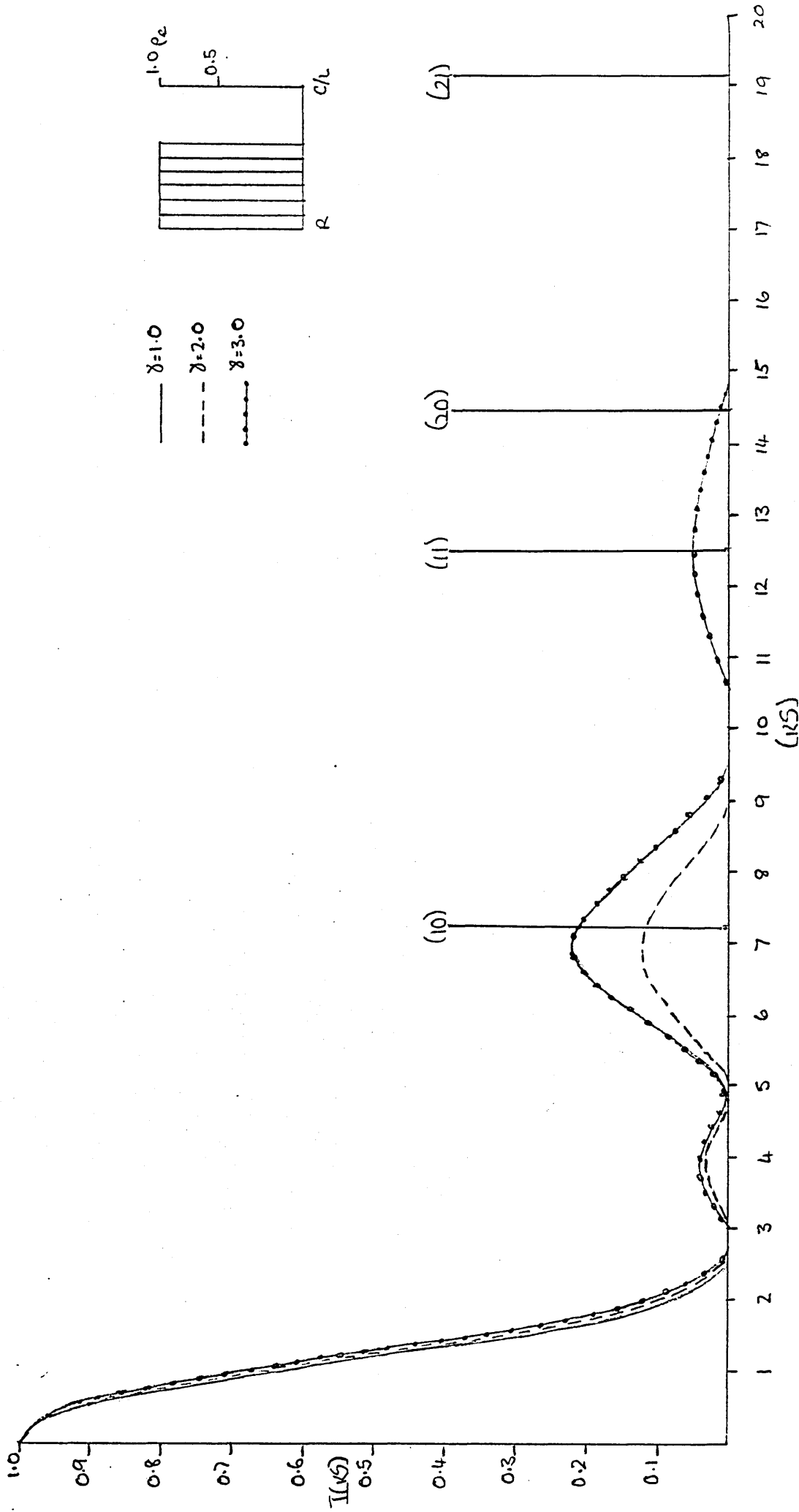


Diagram 10 The Diffraction Patterns due to a Hexagonal Array of Seven Disks (of 60% Fickness) at various values of  $\delta$ . Normalised Intensity of scattering ( $I(kS)$ ) per cylinder for independent aggregates.

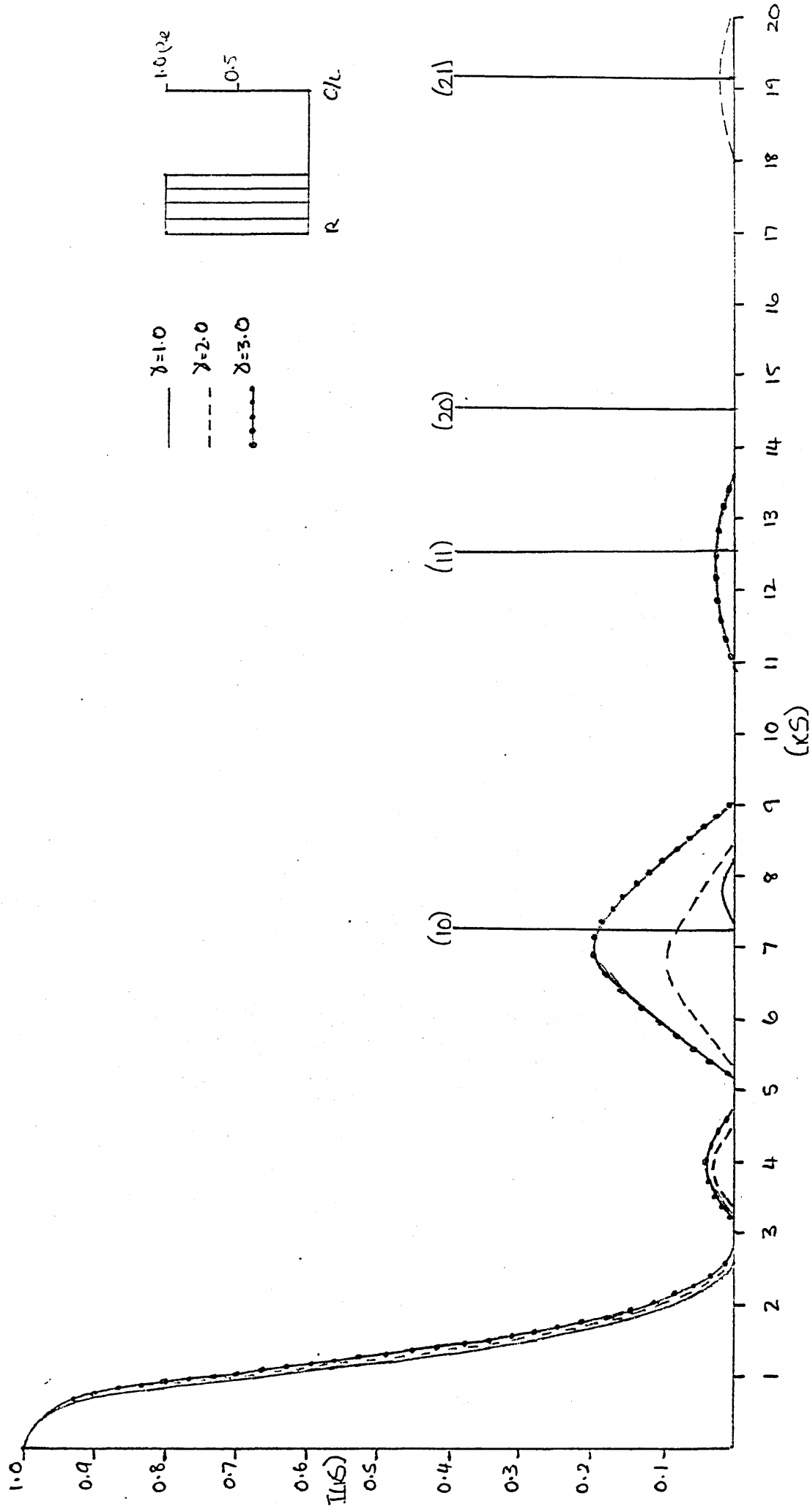


Diagram 11 The Diffraction Patterns due to a Hexagonal Array of Seven Shells (of 40% thickness) at various values of  $\delta$ . Normalised intensity of scattering ( $I(xS)$ ) per cylinder for independent aggregates.

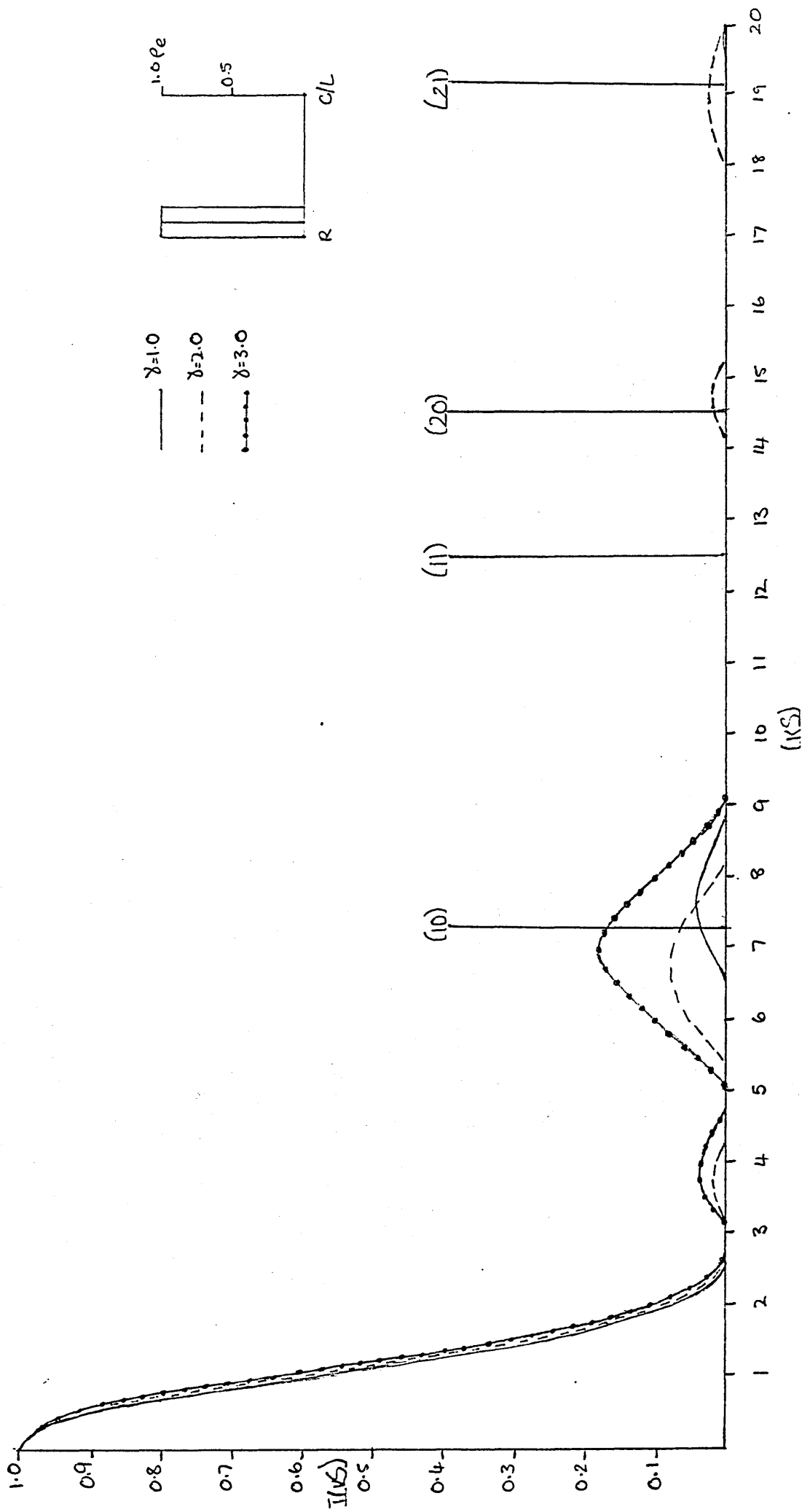


Diagram 12 The Diffraction Patterns due to a Hexagonal Array of Seven Shells (of 20% thickness) at various values of  $\delta$ . Normalised intensity of scattering ( $I(k_s)$ ) per cylinder for independent aggregates.

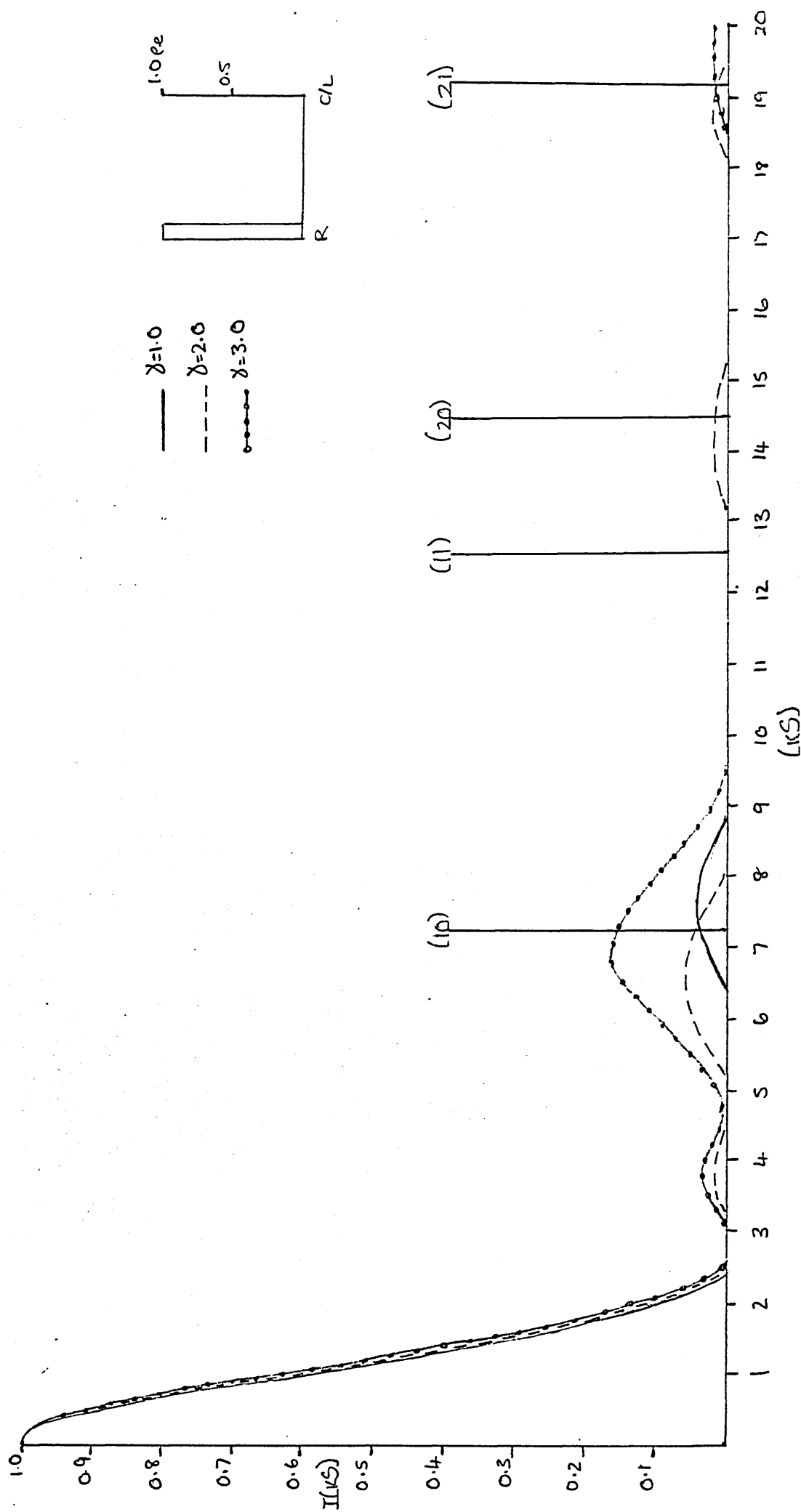


Diagram 13 The Diffraction Patterns due to a Hexagonal Array of Seven Shells (of 10% thickness) at various values of  $\delta$ . Normalised intensity of scattering ( $I(\kappa S)$ ) per cylinder for independent aggregates.

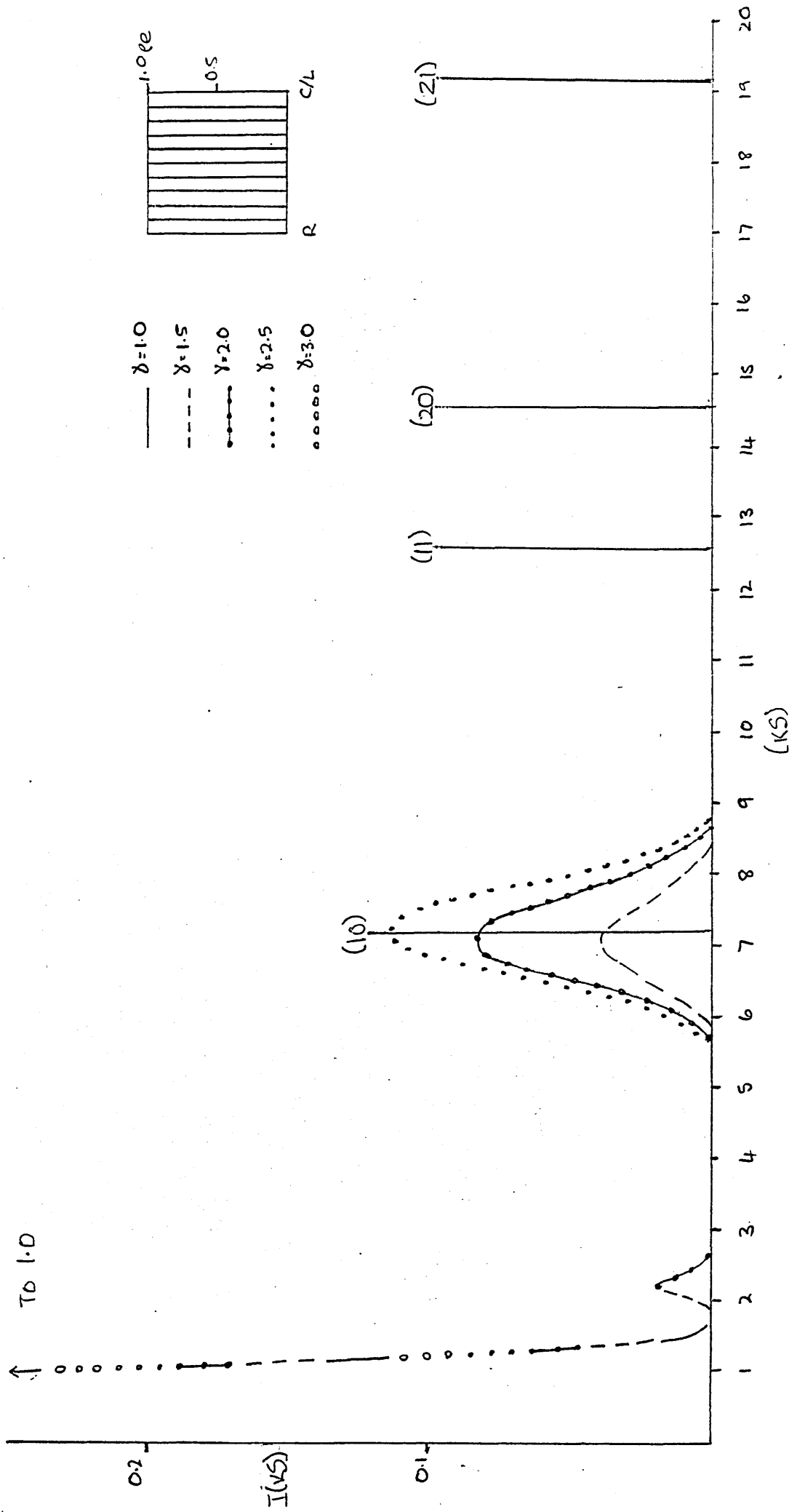


Diagram 14 The Diffraction Patterns due to a Hexagonal Array of Nineteen Solid Cylinders at various values of  $\delta$ . Normalised intensity of scattering ( $I(kS)$ ) per cylinder for independent aggregates.

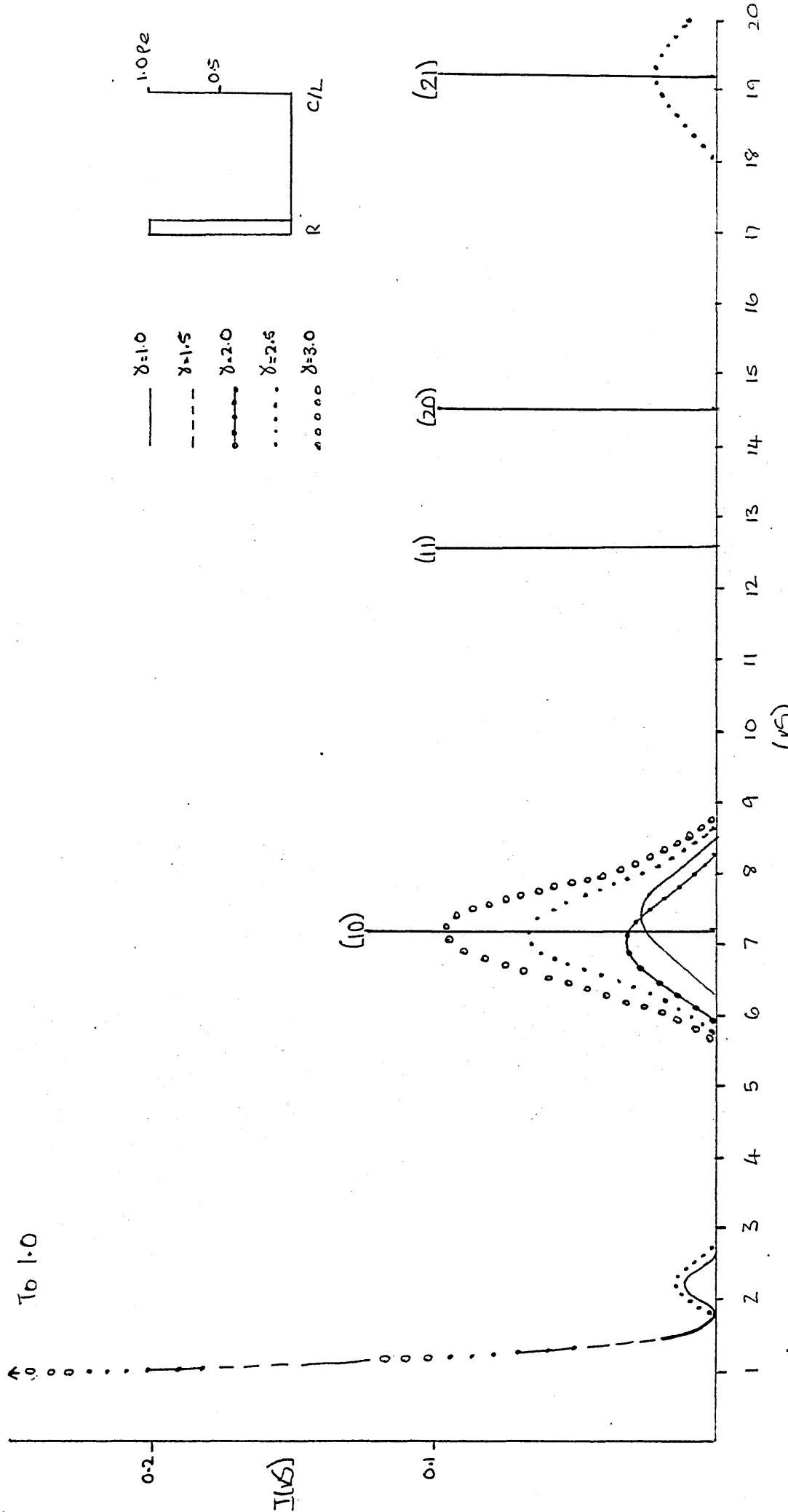


Diagram 15 The Diffraction Patterns due to a Hexagonal Array of Nineteen Shells (of 10% thickness) at various values of  $\delta$ . Normalised intensity of scattering ( $I(k_s)$ ) per cylinder (for independent aggregates).

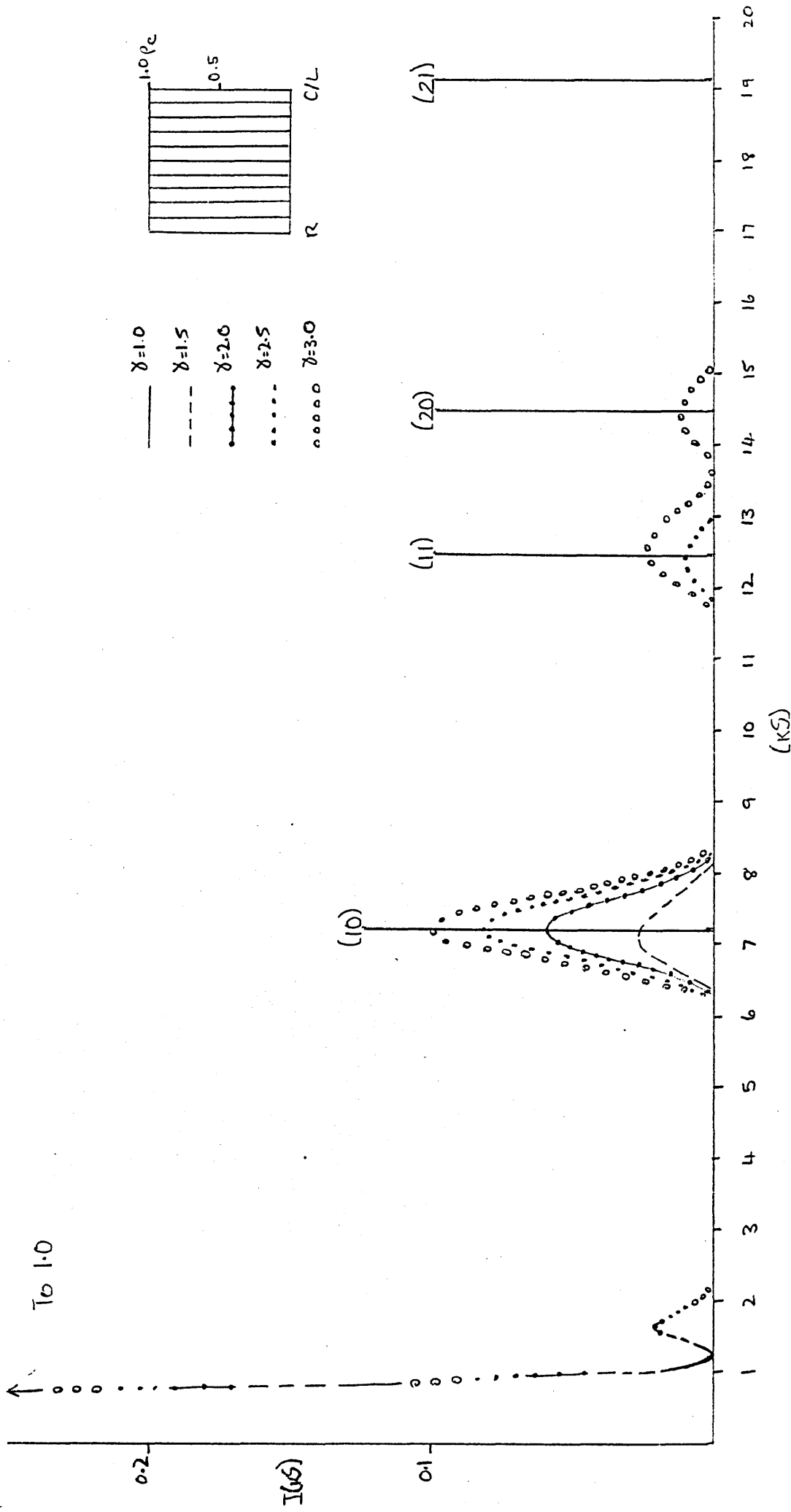


Diagram 16 The Diffraction Patterns due to a Hexagonal Array of Thirty-Seven Solid Cylinders at various values of  $\chi$ . Normalised intensity of scattering ( $I(kS)$ ) per cylinder for independent aggregates.

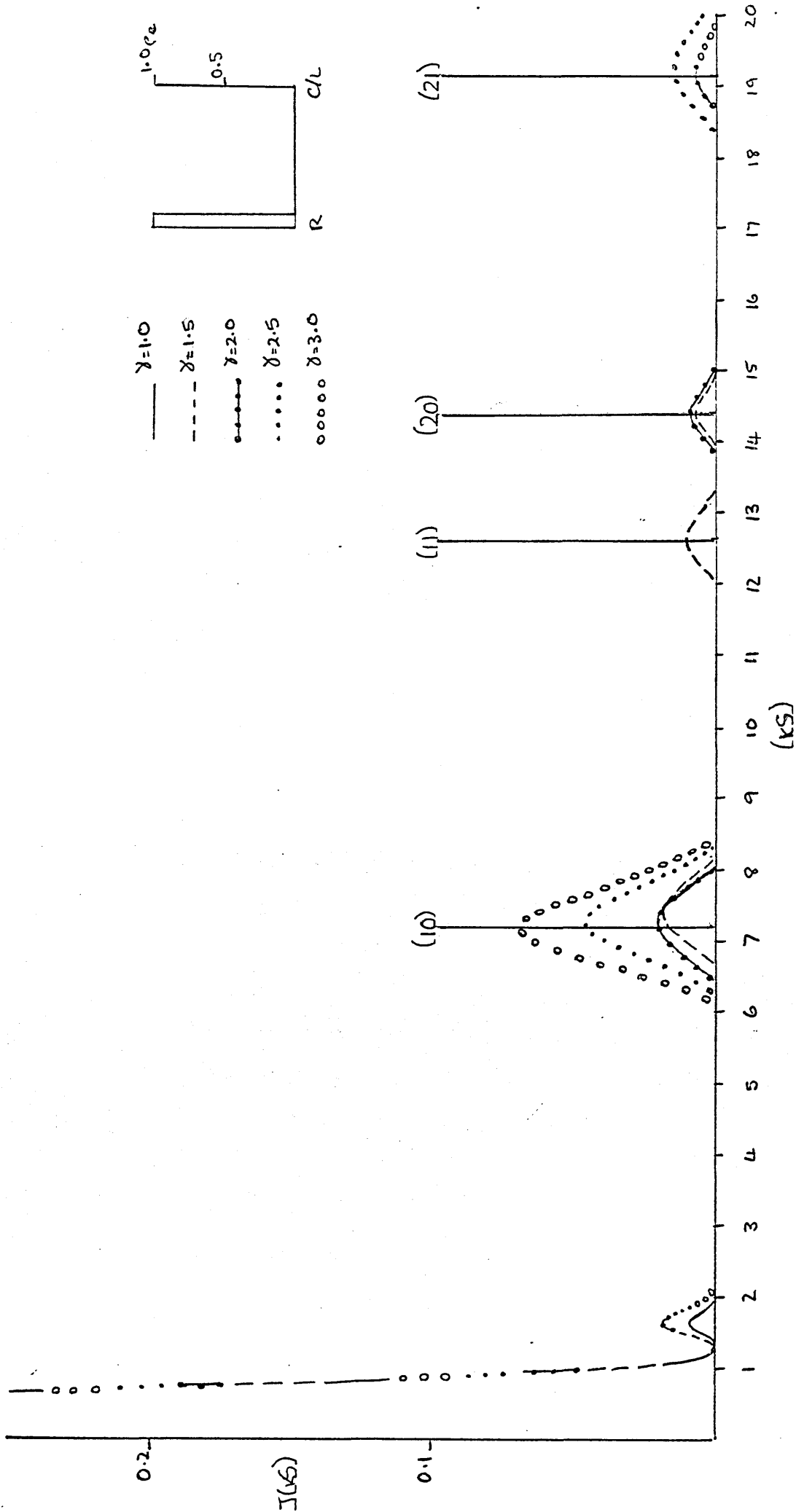


Diagram 17

The Diffraction Patterns due to a Hexagonal Array of Thirty-Seven Shells (of 10% thickness) at various values of  $\delta$ . Normalised Intensity of scattering ( $I(k_s)$ ) per cylinder for independent aggregates.

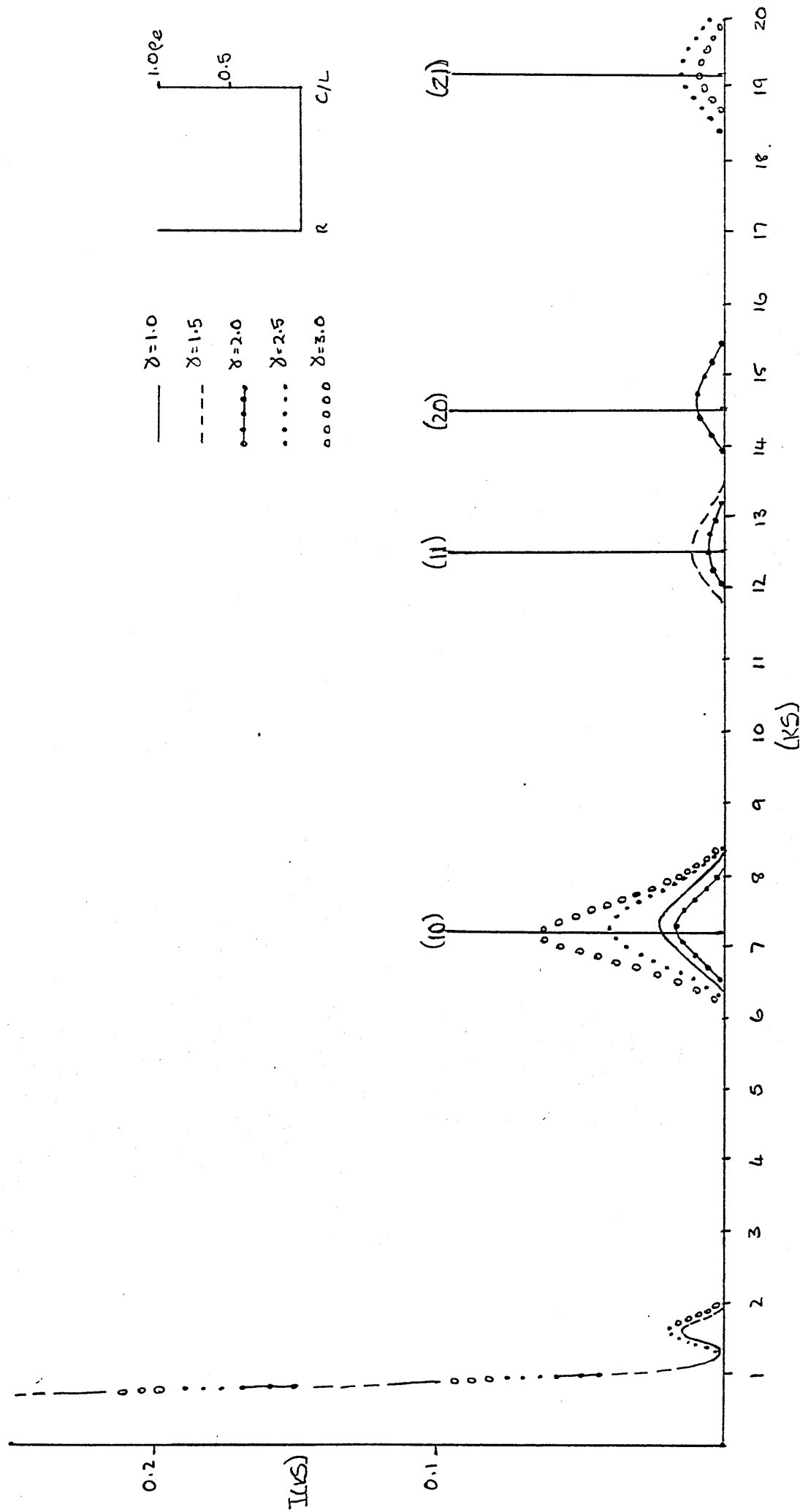


DIAGRAM 14

The Diffraction Patterns due to a Hexagonal Array of Thirty-Seven  $\infty$ -Thin Shells at various values of  $\delta$ . Normalised intensity of scattering ( $I(k_s)$ ) per cylinder for independent aggregates.

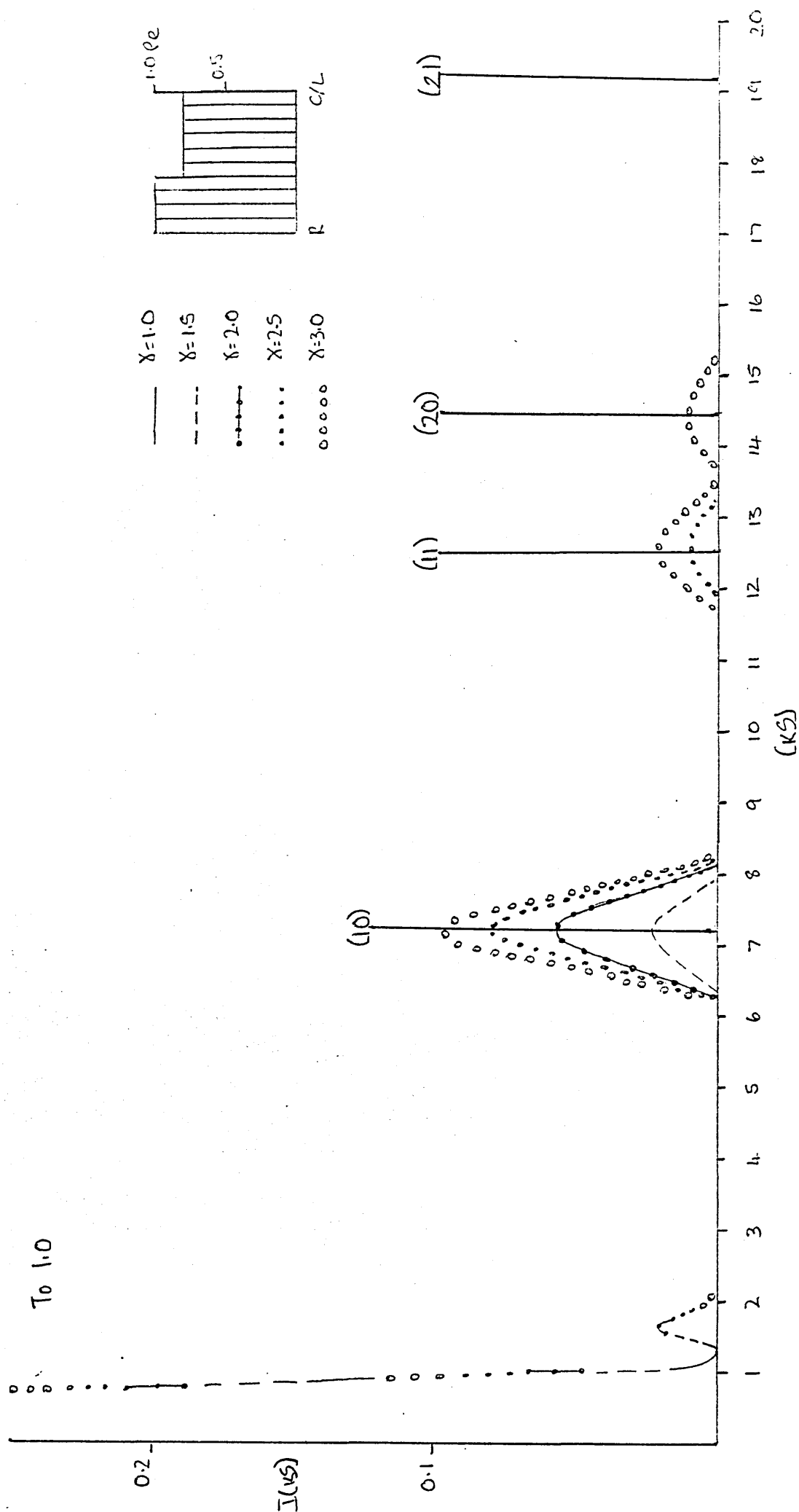


Diagram 19

The diffraction patterns due to a hexagonal array of thirty-seven structured cylinders at various values of  $\delta$ . Normalised intensity of scattering ( $I(k_s)$ ) per cylinder for independent aggregates.

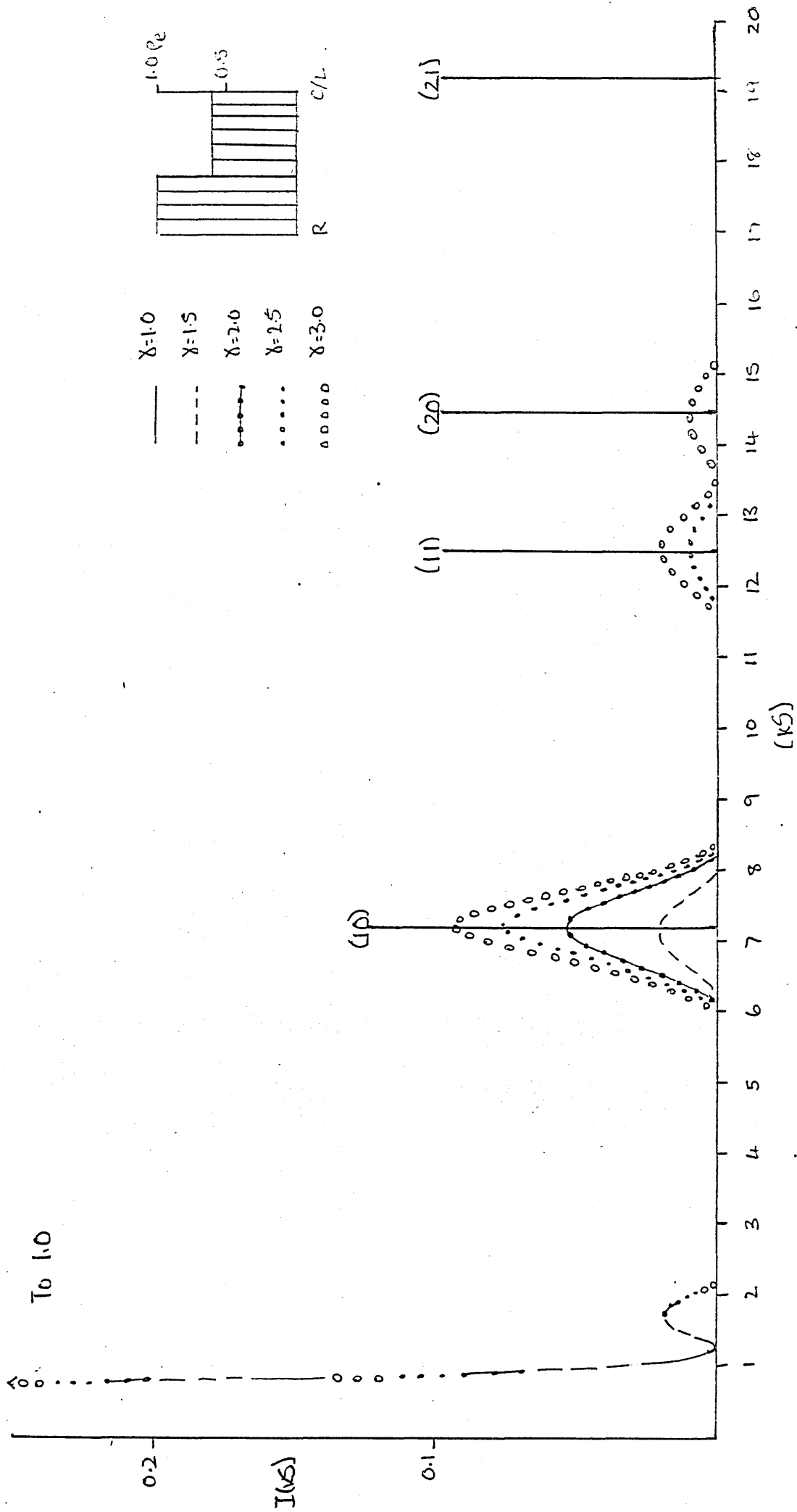


Diagram 20

The Diffraction Patterns due to a Hexagonal Array of Thirty-Seven Structured Cylinders at various values of  $\delta$ . Normalised intensity of scattering ( $I(k_s)$ ) per cylinder for independent aggregates.

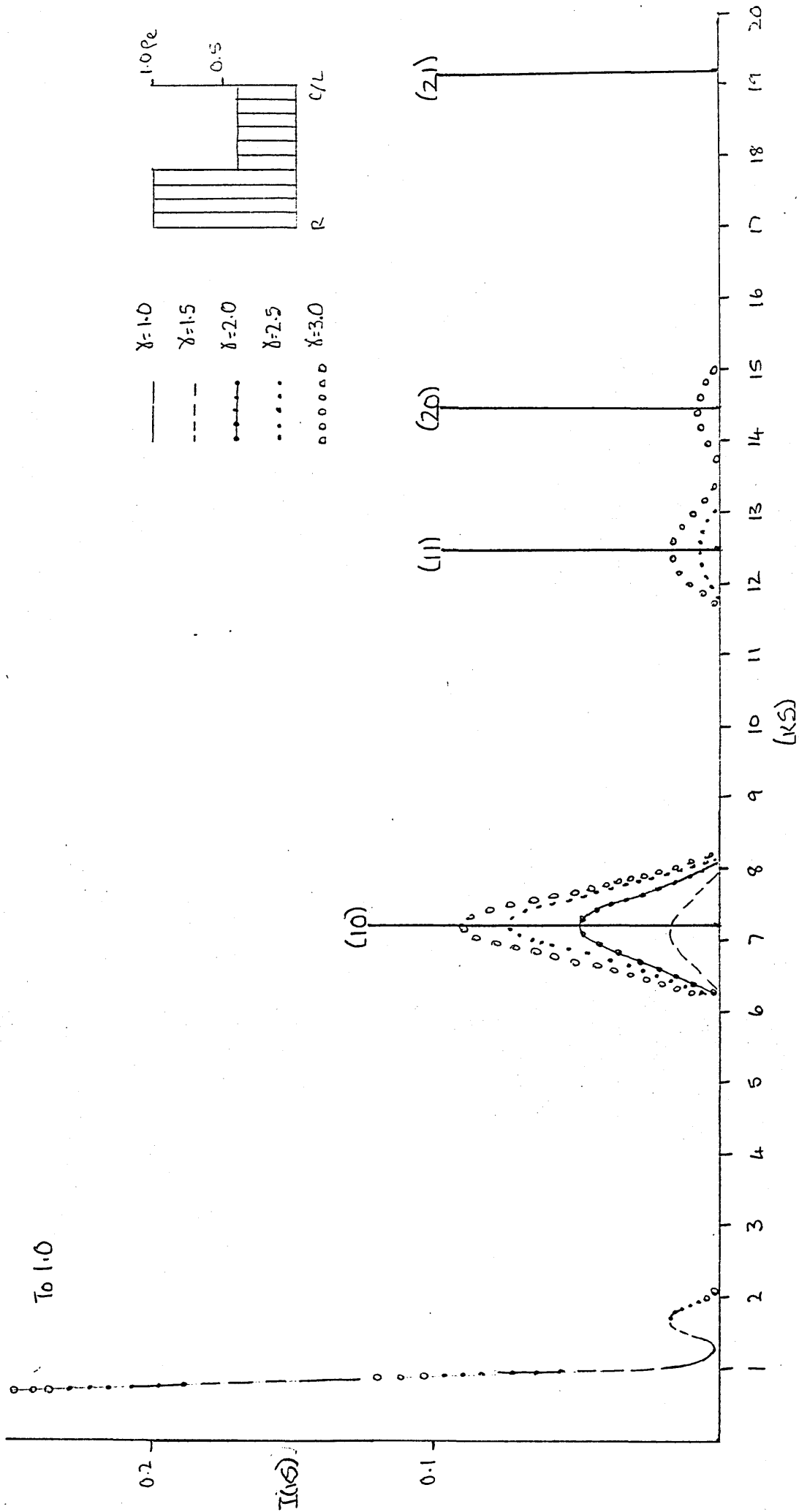


Diagram 21

The diffraction patterns due to a hexagonal array of thirty-seven structured cylinders at various values of  $\delta$ . Normalised intensity of scattering ( $I(k_s)$ ) per cylinder for independent averages.

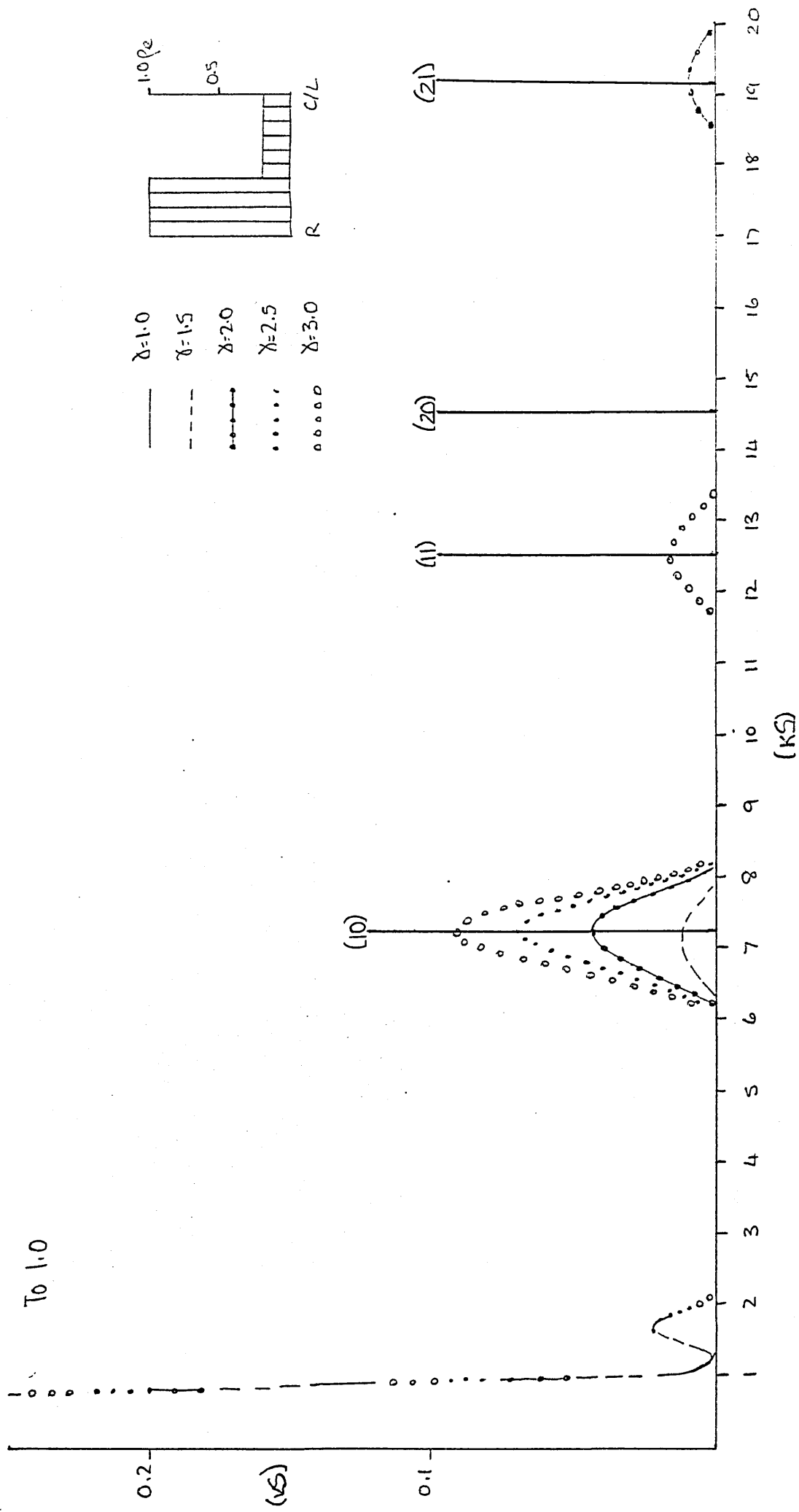


Diagram 22

The Diffraction Patterns due to a Hexagonal Array of Thirty-Sixty Structured Cylinders at various values of  $\delta$ . Normalized intensity of scattering  $(I/I_0)$  per cylinder for independent arrangements.

## APPENDIX A

The following computer program is used to calculate the scattering profiles and diffraction patterns referred to during the course of this work.

The Bessel functions  $J_0(X)$  and  $J_1(X)$  used in computing the lattice interference functions and scattering profiles of the various cylinders are calculated in accordance with the following integrals.<sup>(38)</sup>

$$J_0(X) = \frac{2}{\pi} \int_0^{\pi/2} \cos(X \sin \theta) d\theta \quad - (A1)$$

$$J_1(X) = \frac{2}{\pi} \int_0^{\pi/2} \sin(X \sin \theta) \sin \theta d\theta \quad - (A2)$$

and are computed to an overall accuracy of eight decimal places.

C  
C  
C

DEFINE VARIABLES

```
REAL*8 J0,J1,ED(10),KR,KS,MOTIF,LATTIC,DIFPAT,NUM,DEN
REAL*8 INTFER,V,ENDV,DELV,D,SCALE,LATPNT,SQR3,SQR7,SQR13
REAL*8 SQR19 SQR21,SQR31,SQR37,SQR39,SQR43,SQR57
INTEGER I,N,HEX,OPTION,PLOT
LOGICAL*1 MOT,GRAPH,LAT,STARS(100),NUMER
DATA STARS/100*'*/
```

C  
C  
C

CALCULATE SQROOTS FOR INTERFERENCE FUNCTION

```
SQR3=DSQRT(3.)
SQR7=DSQRT(7.)
SQR13=DSQRT(13.)
SQR19=DSQRT(19.)
SQR21=DSQRT(21.)
SQR31=DSQRT(31.)
SQR37=DSQRT(37.)
SQR39=DSQRT(39.)
SQR43=DSQRT(43.)
SQR57=DSQRT(57.)
```

```

C      SET UP OPTIONS
C
C
C
10     WRITE(5,10)
      FORMAT('1','ENTER T(RUE) OR F(ALSE) FOR OPTIONS REQD')
      WRITE(5,20)
20     FORMAT('0','MOTIF')
      READ(5,30)MOT
30     FORMAT(L1)
      WRITE(5,40)
40     FORMAT(' ','LATTICE')
      READ(5,50)LAT
50     FORMAT(L1)
      WRITE(5,60)
60     FORMAT(' ','NUMERICAL OUTPUT')
      READ(5,70)NUMER
70     FORMAT(L1)
      WRITE(5,80)
80     FORMAT(' ','GRAPHICAL OUTPUT')
      READ(5,90)GRAPH
90     FORMAT(L1)
      IF(.NOT. NUMER.AND..NOT.GRAPH)STOP
      IF(.NOT.GRAPH)GOTO 96
      WRITE(5,95)
95     FORMAT(' ','ENTER INTENSITY SCALE MAXVAL')
      READ(5,*)SCALE
96     IF(LAT.AND..NOT.MOT)GOTO 200
      WRITE(5,100)
100    FORMAT('0','ENTER ELECTRON DENSITIES(10 VALUES)')
      READ(5,*) (ED(N),N=10,1,-1)
      IF(LAT)GOTO 200
      WRITE(5,110)
110    FORMAT(' ','ENTER START, END,DELTA KR')
      READ(5,*)V,ENDV,DELV
      GOTO 240
200    WRITE(5,210)
210    FORMAT('0','ENTER INTERFERENCE FUNCTION NUMBER')
      READ(5,*)I
      LATPNT=3*I**2+3*I+1
      WRITE(5,220)
220    FORMAT(' ','ENTER START, END, DELTA KS')
      READ(5,*)V,ENDV,DELV
      WRITE(5,230)
230    FORMAT(' ','ENTER SWELLING FACTOR')
      READ(5,*)GAMMA

```

```

C      WRITE HEADINGS TO OUTPUT FILE
C
C
240    IF(.NOT.NUMER)GOTO 300
        WRITE(1,310) (ED(N),N=10,1,-1)
        WRITE(1,320)I,LATPNT,GAMMA
        WRITE(1,330)
        IF(.NOT.GRAPH)GOTO 400
300    WRITE(2,310) (ED(N),N=10,1,-1)
        WRITE(2,320)I,LATPNT,GAMMA
        WRITE(2,340) SCALE/2,SCALE
        GOTO 400
310    FORMAT(' ','MOTIF',10F6.2)
320    FORMAT('0','INTERFERENCE FUNCTION NO:',I4,10X,
1      'NO. POINTS:',F16.0,10X,'SWELLING FACTOR',F6.2)
330    FORMAT('0',' KR',10X,' KS',5X,' MOTIF',
1      5X,' LATTICE',5X,'DIFF PATTN')
340    FORMAT('0',' KR',10X,' KS',5X,'0',47X,
1      F5.3,44X,F5.3)

```

```
C      TEST WHICH OPTIONS HAVE BEEN SELECTED AND SWITCH
C      TO APPROPRIATE ROUTINE
C
400    V=V+DELV
        IF(V.GT.ENDV)STOP
        IF(.NOT.MOT)GOTO 470
        IF(MOT.AND.LAT)GOTO 420
410    KR=V
        GOTO 430
420    KR=V/(2*GAMMA)
```

```

C      CALCULATE SCATTERING FUNCTION FOR CYLINDER
C      AND WRITE VALUES TO OUTPUT FILE
C
430    NUM=ED(10)*J1(KR)
        DEN=ED(10)
        DO 440 N=9,1,-1
        NUM=NUM+((ED(N)-ED(N+1))*(0.1*N)*J1(0.1*N*KR))
        DEN=DEN+((ED(N)-ED(N+1))*((0.1*N)**2))
440    CONTINUE
        MOTIF=((2*NUM)/(KR*DEN))**2
        IF(MOT.AND.LAT)GOTO 470
        IF(NUMER)WRITE(1,450)KR,MOTIF
        IF(GRAPH)WRITE(2,460)KR,
        1      (STARS(M),M=1,PLOT(MOTIF,SCALE))
        GOTO 400
450    FORMAT(' ',F5.2,20X,F10.7)
460    FORMAT(' ',F5.2,20X,100A1)

```

```

C      CALCULATE LATTICE INTERFERENCE FUNCTION
C      AND WRITE VALUES TO OUTPUT FILE
C
470    KS=V
      IF(I .GT. 1)GOTO 472
      LATTIC=(7+24*J0(KS)+6*J0(2*KS)
1       +12*J0(SQR3*KS))/49
      GOTO 480
472    IF(I .GT. 2)GOTO 475
      LATTIC=(19+84*J0(KS)+54*J0(2*KS)+24*J0(3*KS)+6*J0(4*KS)
1       +60*J0(SQR3*KS)+72*J0(SQR7*KS)+24*J0(SQR13*KS)
1       +18*J0(2*SQR3*KS))/361
      GOTO 480
475    IF(I .GT. 3)GOTO 477
      LATTIC=(37+180*J0(KS)+138*J0(2*KS)+96*J0(3*KS)
1       +54*J0(4*KS)+24*J0(5*KS)+6*J0(6*KS)
1       +144*J0(SQR3*KS)+216*J0(SQR7*KS)+144*J0(SQR13*KS)
1       +72*J0(SQR21*KS)+24*J0(SQR31*KS)
1       +78*J0(2*SQR3*KS)+96*J0(SQR19*KS)+36*J0(2*SQR7*KS)
1       +24*J0(3*SQR3*KS))/1369
      GOTO 480
477    IF(I .GT. 4)STOP
      LATTIC=(61+312*J0(KS)+258*J0(2*KS)+204*J0(3*KS)+150*J0(4*KS)
1       +96*J0(5*KS)+54*J0(6*KS)+24*J0(7*KS)+6*J0(8*KS)
1       +264*J0(SQR3*KS)+432*J0(SQR7*KS)+336*J0(SQR13*KS)
1       +240*J0(SQR21*KS)+144*J0(SQR31*KS)+72*J0(SQR43*KS)
1       +24*J0(SQR57*KS)
1       +174*J0(2*SQR3*KS)+264*J0(SQR19*KS)+180*J0(2*SQR7*KS)
1       +96*J0(SQR39*KS)+36*J0(2*SQR13*KS)+96*J0(3*SQR3*KS)
1       +120*J0(SQR37*KS)+48*J0(7*KS)+30*J0(4*SQR3*KS))/3721
480    IF(MOT.AND.LAT)GOTO 510
      IF(NUMER)WRITE(1,490)KS,LATTIC
      IF(GRAPH)WRITE(2,500)KS,(STARS(M),M=1,PLOT(LATTIC,SCALE))
      GOTO 400
490    FORMAT(' ',15X,F5.2,20X,F10.7)
500    FORMAT(' ',15X,F5.2,5X,100A1)

```

```
C      CALCULATE DIFFRACTION PATTERN AND WRITE RESULTS
C      TO OUTPUT FILE
C
510    DIFFPAT=MOTIF*LATTIC
      IF(NUMER)WRITE(1,520)KR,KS,MOTIF,LATTIC,DIFFPAT
      IF(GRAPH)WRITE(2,530)KR,KS,(STARS(M),M=1,PLOT(DIFFPAT,SCALE))
520    FORMAT(' ',F5.2,10X,F5.2,5X,F10.7,5X,F10.7,5X,F10.7)
530    FORMAT(' ',F5.2,10X,F5.2,5X,100A1)
      GOTO 400
      END
```

C PLOT FUNCTION SUBROUTINE  
C  
C

```
INTEGER FUNCTION PLOT(A,SCALE)
REAL*8 A
PLOT=IDINT(100*A/SCALE)
IF(PLOT.GT.100)PLOT=100
RETURN
END
```

C JO FUNCTION SUBROUTINE  
C  
C

```
REAL*8 FUNCTION JO(A)
REAL*8 NDPTS,SUMODD,SUMEVN,DTHETA,PI
REAL*8 A
INTEGER M,STRIPS
PI=3.141592653589793
M=100
DTHETA=PI/(2*M)
NDPTS=1+DCOS(A)
SUMODD=DCOS(A*DSIN(DTHETA))
SUMEVN=0.0
DO 1000 STRIPS=2,(M-2),2
SUMODD=SUMODD+DCOS(A*DSIN(DTHETA*(STRIPS+1)))
SUMEVN=SUMEVN+DCOS(A*DSIN(DTHETA*STRIPS))
1000 CONTINUE
JO=(NDPTS+4*SUMODD+2*SUMEVN)/(3*M)
RETURN
END
```

C J1 FUNCTION SUBROUTINE  
C  
C

```
REAL*8 FUNCTION J1(A)
REAL*8 NDPTS,SUMODD,SUMEVN,DTHETA,PI
REAL*8 A
INTEGER STRIPS,M
PI=3.141592653589793
M=100
DTHETA=PI/(2*M)
NDPTS=DSIN(A)
SUMODD=DSIN(A*DSIN(DTHETA))*DSIN(DTHETA)
SUMEVN=0.0
DO 2000 STRIPS=2,(M-2),2
SUMODD=SUMODD+DSIN(A*DSIN(DTHETA*(STRIPS+1)))
1 *DSIN(DTHETA*(STRIPS+1))
SUMEVN=SUMEVN+DSIN(A*DSIN(DTHETA*STRIPS))
1 *DSIN(DTHETA*STRIPS)
2000 CONTINUE
J1=(NDPTS+4*SUMODD+2*SUMEVN)/(3*M)
RETURN
END
```

APPENDIX B

Conversion of diffraction line positions into equivalent interplanar spacings

For a 2-D hexagonal lattice recourse to standard crystallographic theory enables the inter-planar spacing (d) of a set of (hk) planes to be expressed in the form:

$$1/d^2 = \frac{4(h^2 + hk + l^2)}{3s^2} \quad - (B1)$$

where s is the distance between lattice points

The standard Bragg relation is defined as:

$$\lambda = 2d \sin \theta \quad - (B2)$$

The wave vector  $\underline{k}$  is defined by the relation

$$|\underline{k}| = \langle k \rangle = 4\pi \sin \theta / \lambda \quad - (B3)$$

so that using equation (B2) and equation (B3) gives

$$d = 2\pi / \langle k \rangle \quad - (B4)$$

and substituting equation (B4) into equation (B1) gives

$$4\pi^2 / \langle k \rangle^2 = \frac{3s^2}{4(h^2 + hk + k^2)} \quad - (B5)$$

re-arranging terms,

$$(\langle k \rangle s)^2 = \frac{16\pi^2(h^2 + hk + k^2)}{3} \quad - (B6)$$

$$\therefore \langle k \rangle s = \frac{4\pi\sqrt{h^2 + hk + k^2}}{\sqrt{3}} \quad - B7$$

Allowing h and k to take the various values 0,1,2,3.... etc. the equivalent  $\langle k \rangle s$  ( or (kS)) spacings of the particular sets of (hk) planes are obtained.

The equivalent (kS) spacings of the (10), (11), (20) and (21) planes obtained from equation (B7) are 7.26, 12.57, 14.51 and 19.20 respectively.

## REFERENCES

1. Sherwood D, Crystals, X-rays and Proteins. Longmans (1976)  
Ch.1 Elementary discussion of the states of matter.
2. Barker, J.A., Henderson, D. Scientific American Nov. 1981  
p 94-102 The fluid phases of matter
3. Hartshorne, N.H. Liquid Crystals and Plastic Crystals  
(compiled by Gray and Winsor)  
Ch 2. Optical Properties of Liquid Crystals
4. Hartshorne, N.H., Stuart, A. Crystals and the Polarising  
Microscope Arnold (1960)
5. Kelker, H., Hatz, R. Handbook of Liquid Crystals Verlag Chemie (1980)  
Ch. 2 Comprehensive table of mesogens
6. Kelker, H., Hatz, R. Handbook of Liquid Crystals  
Verlag Chemie (1980) Ch. 1
7. Hartshorne, N.H. Stuart, A. Crystals and the Polarising  
Microscope Arnold (1960) Ch. 9
8. Schaetzing, R., Lister, J.D. Advances in Liquid Crystals Vol.4  
(edited by Brown, G.H.) Academic Press (1979)  
p 147 - 202 Light scattering studies of Liquid Crystals
9. Danielsson, I. Lyotropic Liquid Crystals (compiled by  
Frieberg, S). Advances in Chemistry (1979)  
Ch. 2 Lyotropic Mesomorphism
10. Laughlin, R.G. Advances in Liquid Crystals Vol. 3 (edited by  
Brown, G.H.) Academic Press (1978)
11. Kelker, H. Hatz, R. Handbook of Liquid Crystals Verlag Chemie (1980)  
Ch. 11
12. Fontell, K. Liquid Crystals and Plastic Crystals (compiled by  
Gray and Winsor)  
Ch. 4 X-ray diffraction by Liquid Crystals - Amphiphilic Systems
13. Oster, G., Riley, D.P. Acta Cryst. (1952) 5, 1  
Scattering from Isotropic Colloidal and Macromolecular Systems
14. Azaroff L.V. Elements of X-ray Crystallography McGraw-Hill (1968)  
Ch 8 X-ray Scattering by Atoms
15. Oster, G., Riley, D.P. Acta Cryst. (1952) 5, 272  
Scattering from Cylindrically Symmetric Systems.

16. Azaroff, L.V. Elements of X-ray Crystallography  
McGraw-Hill (1968)  
Ch.7 Calculation of Lattice spacings
17. Burge, R.E. Acta Cryst. (1959) 12, 285  
X-ray Scattering by Bundles of Cylinders
18. Burge, R.E. J. Mol. Biol (1961)  
The Structure of bacterial Flagella
19. Burge, R.E. J. Mol. Biol (1963) 7, 213  
Equatorial X-ray Diffraction by Fibrous Proteins
20. Luzzati, V., Mustacchi, H., Skoulios, A., Husson, F.  
Acta Cryst (1960) 13, 660  
La Structure des colloïdes d'Association 1 Les Phases  
Liquide-Cristallines des Systèmes Amphiphile-Eau
21. Luzzati, V., Mustacchi, H., Husson, F. Acta Cryst (1960) 13, 668  
La Structure des Colloïdes d'Association II Description  
des Phases Liquide Cristallines de Plusieurs Systèmes  
Amphiphile-Eau.
22. Luzzati, V., Reiss-Husson, F. Journal of Colloid and  
Interface Science (1966) 21, 534  
Small-angle X-ray scattering study of the structure of  
soap and detergent micelles.
23. Luzzati, V., Tardieu, A. J. Mol Biol (1972) 64, 269  
A pattern recognition approach to the Phase Problem:  
Application to the X-ray diffraction study of biological  
membranes and model systems.
24. Blaurock, A.E, Worthington, C.R. J. Biophys (1966) 6, 305  
Treatment of Low-angle X-ray data from planar and concentric  
multi-layered structures.
25. Worthington, C.R. J. Biophys (1969) 9, 222 The  
interpretation of low-angle X-ray data from planar and  
concentric multi-layered structures.
26. Luzzati, V., Tardieu, A. J. Mol. Biol. (1979) 131, 435  
Structure of low-density Lipoprotein
27. Eikenberry, E.F., Brodsky, B. J. Mol. Biol. (1980) 144, 397  
X-ray diffraction of reconstituted Collagen Fibres

28. Nelander, J.C., Blaurock, A.E. J. Mol. Biol. (1978) 118, 497  
Disorder in nerve myelin: Phasing the higher order reflections  
by means of the Diffuse Scatter.
29. Meek, K.M., Elliott, G.F., Sayers, Z., Whitburn, S.B., Koch, M.H.J  
J. Mol. Biol (1981) 149, 477  
Interpretation of the meridional X-ray Diffraction Pattern  
from Collagen Fibrils in Corneal Stroma
30. Blaurock, A.E., J. Biophys (1973) 13, 281  
X-ray diffraction Pattern from a Bilayer with Protein outside.
31. Blaurock A.E, J. Biophys. (1973) 13, 290  
The Structure of a Lipid-Cytochrome c Membrane
32. Gulik-Krzywicki, T., Shecter, E., Luzzati, V., Faure, M.  
Nature (1969) 223, 1116.
33. Shipley, G.G., Leslie, R.B., Chapman, D., Nature (1969) 222, 561.
34. Lesslauer, W., Acta Cryst. (1974) B30, 1927  
X-ray Diffraction from Fatty-Acid Multi-layers.
35. Lesslauer, W., Act Cryst (1974) B30, 1932,  
X-ray diffraction from Fatty-Acid Multi-layers
36. Vainshtein, X-ray Diffraction from Chain Molecules Elsevier
- 37.1 Wilson, H.R. J. Mol. Biol (1963) 6, 474  
Molecular Arrangement in  $\alpha$ -keratin
- 37.2 Tyson, C.N. Woods, H.J., J. Mol. Biol (1964) 9, 266  
Molecular arrangement in  $\alpha$ -keratin
- 37.3 Wilson, H.R. J. Mol. Biol (1964) 9, 268  
Molecular Arrangement in  $\alpha$ -keratin.
38. Sneddon, I.N., Special functions of mathematical physics and  
chemistry Longmans (1979)  
Ch. 4 Bessel Functions

## ACKNOWLEDGEMENTS

To Dr. R.M. Wood of Sheffield City Polytechnic for his help and constructive criticism during the course of this project.

To the National Coal Board, in particular, Mr. N. Wood, Regional Chief Scientist (East Midlands) for permission to use the computer facilities in his laboratory. To Mrs. H. Greensmith for the painstaking work involved in typing this thesis. Finally to my wife and children for putting up with me during the course of this work.